# PERFORMANCE OF NANOSTRUCTURED TERNARY METAL SPINEL OXIDES AS EFFICIENT ELECTROCATALYSTS

**REHANA ISLAM**

A THESIS SUBMITTED TO THE FACULTY OF GRADUATE STUDIES IN PARTIAL FULFILLMENT OF THE REQUIREMENT FOR THE DEGREE OF MASTER OF SCIENCE

GRADUATE PROGRAM IN CHEMISTRY

YORK UNIVERSITY

TORONTO, ONTARIO

SEPTEMBER 2019

**Abstract**

In this work, various spinel oxides, namely $Ni_{1-x}Cu_xCo_2O_4$ ($0 \leq x \leq 0.75$), $Fe_y(Ni/Cu)_{x-y}Co_{3-x}O_4$ [($0.5 \leq x \leq 1$), ($0.1 \leq y \leq 0.15$)] have been prepared on Fluorine coated Tin Oxide (FTO) glass by the thermal decomposition method. The films were characterized by scanning electron microscopy (SEM), energy dispersive X-ray spectrometry (EDX), X-ray diffraction (XRD) analysis and cyclic voltammetry (CV), to link the surface morphology, stoichiometric composition, spinel phase information, and electrocatalytic activity. The SEM analysis shows that the prepared spinel oxide electrodes are uniformly distributed over the substrate and can be quite porous. The formation of a spinel structure was confirmed by XRD analysis for all our samples and their composition is, with a few exceptions, very close to the expected one. In our $Ni_{1-x}Cu_xCo_2O_4$ ($0 \leq x \leq 0.75$) samples, an increase of lattice parameter with the increase of copper content was observed. The modification of cobalt-based electrodes to form $Fe_yCu_{x-y}Co_{3-x}O_4$ [($0.5 \leq x \leq 1$), ($0.1 \leq y \leq 0.15$)] enhances their catalytic activity towards the oxygen evolution reaction in an alkaline media as confirmed by CV. The $Fe_{0.1}Cu_{0.9}Co_2O_4$ shows the highest current density of 0.45 $mA/cm^2$ at 900 mV among all other electrodes studied. The correlation between composition, surface morphology, phase information, and electrocatalytic activity is discussed in this thesis. Finally, all ternary spinel oxide samples will be compared with those of binary spinel oxide prepared in the Morin group and other materials prepared in the literature.

# Dedication

To my beloved Children

(Sharar & Nabil)

**Acknowledgements**

First, I would like to express my deepest thanks to Prof. S. Morin for providing me with this great opportunity to continue my higher education and acquire further knowledge in the field of electrochemistry and materials science. Moreover, this work would not have been successfully done without her supervision and continue help, guidance and patience during the course of my studies.

Second, I would like to acknowledge the valuable help of Magdalena Jaklewicz, York University for SEM and EDX measurements and analysis and Victoria Jarvis, McMaster University for XRD measurements and X-ray pattern analysis.

Third, I would like to thank my supervisory committee members, Prof. R. Fournier and Prof. C. Caputo for their informative advice, instruction and feedback on my research project. Also, I would like to thank Prof. G. Lavoie (former Graduate Program Director, Department of Chemistry) for his advice and guidance.

Fourth, I would like to thank all members of Prof. Morin's research group for their help, time and co-operation. I would also like to extend my deepest thanks to my beloved children (Sharar and Nabil), my husband, all my brothers and sisters for their continuous encouragements and moral support.

Finally, I would like to acknowledge the Natural Science and Engineering Research Council (NSERC) of Canada and York University for their financial support.

## Table of Contents

**List of Tables**

**List of Figures**

## List of Acronyms

OER Oxygen evolution reaction

SEM Scanning electron microscopy

EDX Energy dispersive X-ray spectroscopy

XRD X-ray diffraction

CV Cyclic voltammetry

FTO Fluorine doped tin oxide

SCE Saturated calomel electrode

NHE Normal hydrogen electrode

## List of Symbols

| | |
|---|---|
| $A$ | Area of the working electrode |
| $A_g$ | Geometrical surface area |
| $A_r$ | Real surface area |
| $C$ | Capacitance |
| $C_{dl}$ | Double layer capacitance |
| $d_{hkl}$ | Spacing between the atomic planes |
| $E$ | Electrode potential |
| $\sigma$ | Electrical conductivity |
| $E_{pa}$ | Peak anodic potential |
| $E_{pc}$ | Peak cathodic potential |
| $j_{cap}$ | Capacitive charging current density |
| $i_{pa}$ | Peak anodic current |
| $i_{pc}$ | Peak cathodic current |
| $L_{view}$ | Viewing screen |
| $O$ | Oxidized forms of electroactive species |
| $Q$ | Electrical charge |
| $R$ | Reduced forms of electroactive species |
| $R_f$ | Roughness factor |
| $\rho$ | Resistivity |
| $S_{pec}$ | Scanned specimen |
| $v$ | Scan rate |
| $\lambda$ | Wavelength |

# Chapter 1: Introduction

Since the beginning of the Industrial Revolution there has been a large increase in global energy consumption in peoples daily lives. The major portion of the world's electrical energy is generated by the combustion of fossil fuels and nuclear energy. According to the International Energy Agency in 2017, fossil fuels accounted for 66.8% of electricity generated globally, and nuclear energy contributed another 10.2% [1]. The major source of carbon dioxide in the atmosphere arises from the burning of fossil fuels in the generation of electricity or emissions from automobiles, heating and various industries [2]. Due to the burning of fossil fuels, environmental pollution, which is responsible for global warming and climate change have become major issues. On the other hand, nuclear energy has safety and waste disposal problems.

In past decades, due to rising global warming, climate change, and pollution issues, there has been more interest in alternative clean energy sources [3, 4]. Water electrolysis has received great attention due to global energy conservation as it can be used to produce hydrogen gas. However, hydrogen gas needs to be produced in an environmentally sound and efficient way. The inefficiency of this process comes from the high overpotential of the oxygen evolution reaction (OER) at the anode due to its irreversibility [5 - 9]. Therefore, producing hydrogen fuel from water electrolysis remains inefficient. A great deal of effort is dedicated to design an optimize the anode in order to achieve a low OER overpotential. These anode materials can be readily applied to other energy technologies, such as batteries, solar panel, capacitor, etc.

According to Lee *et al*. Iridium oxide ($IrO_2$) and ruthenium oxide ($RuO_2$) catalysts are among the most active catalysts for OER up to date with an overpotential of 0.25 V in alkaline media [10]. Trasatti *et al.* also mentioned that they are very active oxides, however, they are costly and low in abundance [11, 12]. Therefore, the replacement of these precious metals is necessary.

The behavior of electrode material is directly associated with overpotential and hence the energy cost of the overall process. Among the oxide electrodes, transition metal oxides with spinel structures are of great interest as they have the ability to switch between different valence states and exhibit good catalytic activity by lowering the overpotential in the oxygen evolution reactions [7]. Therefore nanostructured transition metals play a significant role in research and industrial applications such as water electrolysis, fuel cell, and metal-air batteries as their high surface area to volume ratio tends to lower overpotential [13 - 15].

Many different types of oxides such as perovskites ($LaCaCoO_3$) [16, 17] and pyrochlores ($Pb_2Ru_2O_{6.5}$) [18] have been successfully applied in oxygen and chlorine evolution reactions. Among the oxide electrodes, Cobalt oxide ($Co_3O_4$) spinel types inherently possess appreciable electrocatalytic activity [19, 15], their components are high in abundance, of low cost, and possess optimum corrosion stability [20, 11].

## 1.1. Spinel structure and properties

A normal spinel structure are usually cubic close-packed oxides with eight tetrahedral and four octahedral sites per formula unit. The general formula of a spinel oxide can be expressed as $[A][B_2]O_4$ where A represents a divalent cation ($A^{2+}$), where $A^{2+}$ ions occupy one - eighth of the tetrahedral sites. On the other hand, B represents a trivalent cation ($B^{3+}$), where $B^{3+}$ ions occupy one - half of the octahedral sites [21, 22]. In the inverse spinel oxide $[B][AB]O_4$, all divalent cations occupy the octahedral sites while half of the trivalent cations occupy the tetrahedral sites and the other half occupies the octahedral sites [23]. A mineral spinel $MgAl_2O_4$ has a normal spinel structure which is illustrated in Figure 1.1[24].

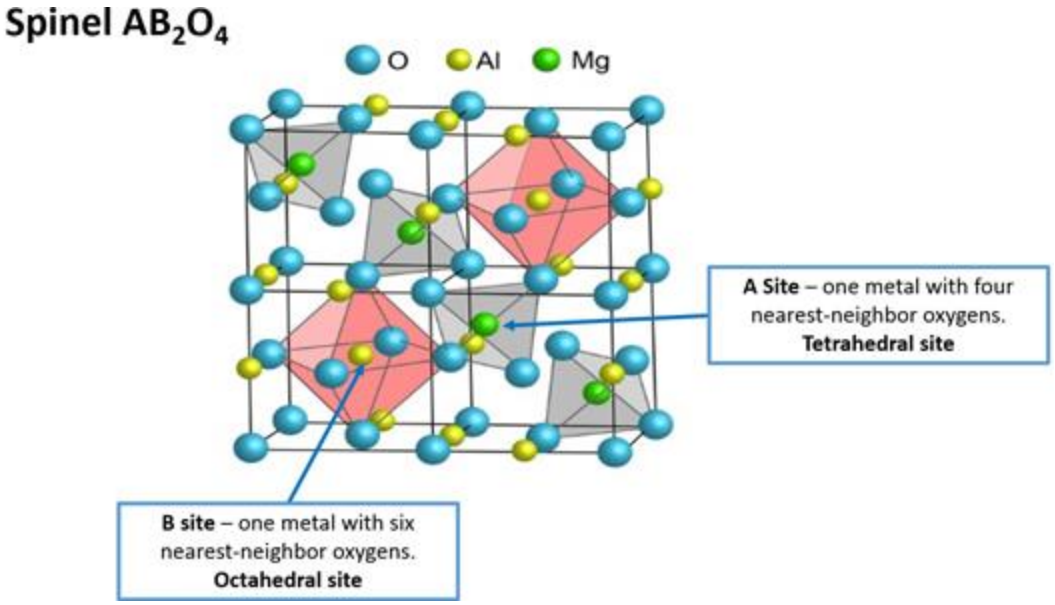


**Figure 1.1:** Schematic diagram of the spinel crystal structure for $MgAl_2O_4$ containing 4 formula units. Image is reproduced with author's permission [24].

Among metal oxides, spinel cobaltites [$M_xCo_{3-x}O_4$ where M = Ni, Cu, Mn, Fe, Mg, Zn] have received the most attention as they can be optimized for optimal catalytic activity towards the OER [25 - 27]. Cobalt transition metal oxides spinel structure has the ability to switch between different valence states. Cobalt oxide spinel ($Co_3O_4$) can be represented as $Co^{2+}[Co^{3+}]_2O_4$. The divalent site can be filled by other divalent metal ions, such as Ni, Cu, Mn, Zn, and produce binary spinel-type oxides. Introducing two divalent metal ions in cobalt-based spinel oxide is known as ternary spinel oxide. The substitution of more octahedral sites is expected to increase the conductivity of the material as a p-type semiconductor, which enhances electrocatalytic activity in the oxygen evolution reaction. The conductivity associated chain is followed by this mechanism [28, 11]:

$$M^{4+} \rightleftharpoons M^{3+} + \text{hole} \qquad (1)$$

Since the cation distribution between the tetrahedral and octahedral sites determines the properties of the material, a detailed study of the distribution of the cation is necessary to develop electrochemical applications for spinel oxides.

### 1.1.1. Objective

In order to develop a suitable catalyst for various applications, it is necessary to understand the relationship between morphology, structure, composition and electron transfer properties. This research main objective is to synthesize $M_{1-x}M_xCo_2O_4$ ($0 \leq x \leq 1$), where M and *M* = Ni, Cu or Fe spinel oxide electrodes of various compositions ($NiCo_2O_4$, $Ni_{0.95}Cu_{0.05}Co_2O_4$, $Ni_{0.9}Cu_{0.1}Co_2O_4$, $Ni_{0.75}Cu_{0.25}Co_2O_4$, $Ni_{0.5}Cu_{0.5}Co_2O_4$, $Ni_{0.25}Cu_{0.75}Co_2O_4$, $Fe_{0.1}Cu_{0.9}Co_2O_4$, $Fe_{0.15}Cu_{0.35}Co_{2.5}O_4$, $Fe_{0.1}Ni_{0.9}Co_2O_4$, and $Fe_{0.15}Ni_{0.35}Co_{2.5}O_4$) as well as $Fe_{0.15}M_{0.35}Co_{2.5}O_4$ ($0 \leq x \leq 0.5$) where M = Ni or Cu on FTO (Fluorine doped Tin Oxide) glass through the thermal decomposition method. We observed how the spinel's electrolytic properties correlate with surface morphology and structure upon changing their composition. The surface morphology, composition, unit cell parameter, and electrocatalytic activity were studied by scanning electron microscopy (SEM), energy dispersive X-ray spectroscopy (EDX), X-ray diffraction (XRD) and cyclic voltammetry (CV), respectively. We will also pay additional attention to the reproducibility of the prepared electrodes. Finally, we must understand the role of active sites and establish the trends in order to suggest future work to produce electrocatalysts for the production of cleaner energy.

## 1.2. Nanostructured metal oxide as Electrocatalysts

Many metal spinel oxides have received great attention due to their wide range of application as electrode materials in batteries, magnetic materials as data storage, capacitors, and oxygen reduction catalysts in fuel cells [29 - 35].

### 1.2.1. Overview of critical literature for Spinel oxides as Electrocatalysts ($M_xCo_{3-x}O_4$, where M = Ni, Cu, Fe, and $0 \leq x \leq 1$)

Singh *et al*. reported that among metal oxides, Cobalt- based metal oxides have received much attention as they possess both catalytic activity and corrosion stability [25, 36, 37]. Copper substitution is more advantageous due to its low cost, high abundance, high stability and good electrochemical properties [38 - 40]. Nikolov *et al.,* Angelov *et al.* and Li *et al.* studied the binary structures of $Cu_xCo_{3-x}O_4$ [41, 42, 43, respectively] and reported that copper to cobalt ratio at the surface is higher than that of the bulk material by X-ray photoelectron and Atomic absorption spectroscopy methods. Marsan *et al*. also noticed that catalytic activity was enhanced with the introduction of copper into cobalt oxide lattice [44].

According to Li *et a*l., nickel substitution has the advantage of low intrinsic electrical resistivity, stability and is reported to be a very active anode for oxygen evolution reaction [45]. Singh *et al.* reported that cobalt based ternary spinel oxide with nickel and copper showed higher catalytic activity compared to other cobaltite [46, 47]. On the other hand, spinel ferrites $M_xFe_{3-x}O_4$ (where M= Ni, Co, Mn, Mg) also received attention due to their magnetic, catalytic, optical and electrical properties [48].

In the context of developing a better catalyst for fuel cell applications, the Stahl group has recently developed a combinatorial methodology to study metal oxide properties [49]. They reported that trimetallic (ternary) mixed metal oxides enhanced greatly the electrocatalytic activity for water oxidation [50]. In cobalt based Ni, Cu, ternary spinel oxide electrodes, cobalt or nickel was found to lower the overpotential in the water oxidation reaction while copper possessed the highest electrochemical activity for oxygen evolution [51, 52]. Different combinations and ratios of these elements are targets for catalyst design due to their high chemical stability and relatively

low cost over noble metals. Other studies point to the importance of active sites and their oxidation state [53 - 56]. Therefore, a relationship between surface active sites and catalytic activity has become a subject of interest in the field of renewable energy production.

In our lab, we have found that nickel-copper containing cobalt-based ternary spinel oxides are promising electrode materials. Alternatively, Fe - which also can be a divalent or trivalent cation - can occupy the tetrahedral sites [57, 58]. According to Ting Lu *et al.*, Fe-doped $NiCo_2O_4$ electrodes enhanced electrocatalytic activities towards both oxygen evolution reactions and oxygen reduction reactions; as such it can act as a bifunctional catalyst for metal-air battery and fuel-cell applications [59]. However, the properties of Fe-doped $CuCo_2O_4$ electrodes have not been studied extensively.

### 1.2.2. Oxygen evolution reaction as a model reaction

Oxygen evolution reaction (OER) is one of the basic chemical reactions in water electrolysis. The generation of the current is due to the oxidation/reduction of the materials at the working electrode. The produced current as a function of potential can give information about electron transfer kinetics and mechanism at the electrode/solution interface. Two different types of OER have been reported, a four - electron and a two - electron reaction shown in equations *(2)* [60] and *(3)* [61], respectively.

$$4\ OH^- \longrightarrow O_2 + 2\ H_2O + 4e^- \qquad (2)$$

$$H_2O \longrightarrow \tfrac{1}{2}\ O_2 + 2\ H^+ + 2e^- \qquad (3)$$

Oxygen evolution reactions with a minimum anodic overpotential are required to obtain better electrocatalytic behaviour and to fabricate inexpensive electrocatalysts. Nanostructured materials with high surface area to volume ratios generally enhance electro-transfer properties at lower overpotential [62, 8].

Two electron transfer mechanism is applicable for the oxygen reduction reaction when the electroactive species concentration is high enough to remain unchanged during the potential sweep. (e.g. $CO_3^{2-}$ or possibly $O_2^{2-}$) [63, 64].

The four- electron transfer mechanism is illustrated below.

$$M + OH^- \xrightarrow{\Delta G_1} MOH^* + e^- \quad (4)$$

$$MOH + OH^- \xrightarrow{\Delta G_2} MO^* + H_2O + e^- \quad (5)$$

$$MO + OH^- \xrightarrow{\Delta G_3} MOOH^* + e^- \quad (6)$$

$$MOOH + OH^- \xrightarrow{\Delta G_4} M + O_2 + H_2O + e^- \quad (7)$$

The above model reaction mechanism is associated with the oxygen evolution reaction, where M is an active site and $\Delta G_1$ to $\Delta G_4$ is the Gibbs free energy of each reaction step [65]. It is noted that each reaction step involves the transfer of one electron and $\Delta G_3$ remains positive at the reversible potential [65]. Dau *et al.* stated that the reaction energies for each step differs due to difference in adsorption energies of the intermediate species [66]. According to Halck *et al*., 1.23 eV energy is transferred by each electron in the oxidation reaction [67]. The free energy of $OH^*$ and $OOH^*$ intermediates show a difference in energy of 3.2 eV, while the ideal catalyst shows 2.46 eV [68]. The two main factors that are directly related to the electrocatalytic activity of the oxygen evolution reaction are the bond strength of the M-$O^*$ in the intermediate state and the rate of electron transfer, which mainly depends on the active sites of the materials [69]. The Sabatier principle is based on a relationship between the binding of adsorbed species and the catalytic activity. According to the Sabatier principle, the active site of the catalyst and the adsorbed species should bind neither too strongly nor too weakly in the oxygen evolution reaction [70, 71].

The mechanism of OER is more complex as many intermediate states are involved in the reaction states. Other factors, such as mass transport, also control the rate of the OER [72].

It is necessary to know about mass transfer and electron transfer in order to understand the properties of a specific electrode. Therefore, the interpretation of the kinetic parameters can be quite complicated for the oxygen evolution reactions.

## 1.3. Structure of the thesis

This thesis consists of five chapters: Chapter 1 gives a brief introduction of nano-structured spinel oxides and their properties, concepts behind this research and its objectives. Chapter 2 outlines the preparation methodology, and resultant characterization techniques. Chapter 3 highlights results from various characterizations such as SEM, EDX, and XRD, its analysis and their underlying principles. This chapter also draws comparisons with previous studies and literature. Chapter 4 presents discussions on the experimental data from cyclic voltammetry. Lastly, chapter 5 summarizes the conclusion of this study and creates suggestions for future work.

# Chapter 2- Methodology and Characterization

## 2.1. Thermal decomposition method

The efficiency of electrocatalyst normally dependents on parameters, such as its composition, its structure, its particle size, nature of precursors and method of preparation. Several methods have been used to prepare spinel cobaltites including thermal decomposition [73, 12], co-precipitation [37, 74], sol-gel [36, 75, 76], spray-pyrolysis [77, 78], hydrothermal [79], electrodeposition [80]. A careful choice of the synthesis methodology can tailor the electrocatalyst nanostructure and morphology. According to many studies, small changes in experimental parameters can greatly affect the nanostructure and properties of these materials [81, 30, 31,]. The nitrate precursor was chosen as it involves atomic level mixing by forming a solid solution [48]. A thermal decomposition method has been chosen for the preparation of the electrode since it produces films with high mechanical stability. It is also a convenient and rapid preparation method [45, 12].

### 2.1.1 Preparation of electrolyte solution

During the cyclic voltammetry experiment, electron transfer can occur. The electrical neutrality is maintained through the migration of ions in solution. When electrons transfer from the electrode to the analyte, ions move in solution to compensate the charge and close the electrical circuit. A salt that is highly purified, chemically inert and soluble in the appropriate solvent must be chosen in order to decrease the resistivity of the solution. The concentration of the electrolytes increases the solution's conductivity and can also limit analyte migration. 1 M KOH- electrolyte solution is prepared for the cyclic voltammetry experiment. The temperature of the experiments

was carried out at room temperature (21 ± 2°C) . High purity USP grade Argon gas is used in this work to purge the electrolyte solution.

### 2.1.2. Preparation of (AB) $Co_2O_4$ with A, B = Cu, Ni, Fe ternary spinel oxides

All chemicals were analytical reagent grade and used without additional purification. Cobalt nitrate hexahydrate - $Co(NO_3)_2{\cdot}6H2O$ (98%), nickel nitrate hexahydrate - $Ni\ (NO_3)_2{\cdot}6H_2O$ (98.5%), copper nitrate trihydrate - $Cu(NO_3)_2{\cdot}3H_2O$ (99%), iron nitrate nonahydrate – $Fe(NO_3)_3{\cdot}9H_2O$ (98%), isopropanol - $(CH_3)_2CHOH$ (98%) and Triton X-100 were purchased from Sigma Aldrich. Reagent water (Millipore water) was used in this work from Millipore, Milli-Q Synthesis A10 filter through 0.22μm. The individual 0.5 M stock salt solutions were prepared by dissolving $Co(NO_3)_2{\cdot}6H_2O$, $Ni(NO_3)_2{\cdot}6H_2O$, $Cu(NO_3)_2{\cdot}3H_2O$ and $Fe(NO_3)_3{\cdot}9H_2O$ precursors in isopropanol-Millipore water mixture (volume ratio 4:1). In this work, three different sets of ternary spinel oxides were prepared by the thermal decomposition method.

#### 2.1.2.1. Preparation of $Ni_{1-x}Cu_xCo_2O_4$ ternary spinel oxides ($0 \leq x \leq 0.75$)

Glass coated with a thin fluorine-doped tin oxide layer ((FTO coated glass, surface resistivity ≈ 7 Ω/sq) FTO glass, Pilkington), was cut into 1.5 cm x 1.5 cm in size, washed with Millipore water and sonicated in isopropanol.

Six different precursor solution (0.3 M) were prepared to produce $Ni_{1-x}Cu_xCo_2O_4$ with (x = 0.00, 0.05, 0.10, 0.25, 0.50, 0.75). 10 μL of Triton X-100 were added to the solution to reduce the surface tension of the liquid film. The solutions were stirred well before the deposition. These nitrate salts solutions were deposited directly with a micropipette onto the pre-treated piece of FTO glass. The solvent was evaporated by heating the samples at 60°C on a heating plate. Subsequently, samples were heated in a box furnace (Lindberg BF51732BC) at 300°C for ten minutes. Typically, five oxide layers were deposited by repeating the procedure described above. Finally, the samples

were annealed at 300ºC for one hour [4, 6] to complete the thermal decomposition in order to obtain the ternary spinel oxide films. The amount of material deposited was also calculated by weighing the substrate before and after each layer was deposited and annealed.

### 2.1.2.2. Preparation of $Fe_yCu_{x-y}Co_{3-x}O_4$ ($0 \leq x \leq 1$), ($0 \leq y \leq 0.1$)

Similarly, two different compositions of $Fe_{0.1}Cu_{0.9}Co_2O_4$ and $Fe_{0.15}Cu_{0.35}Co_{2.5}O_4$ were prepared by the thermal decomposition method followed by the same procedure. These samples were calcined at 400°C for ten minutes and the final annealing was set for 400°C for two hours to complete thermal decomposition [27].

### 2.1.2.3. Preparation of $Fe_yNi_{x-y}Co_{3-x}O_4$ ($0 \leq x \leq 0.5$), ($0 \leq y \leq 0.15$)

The same procedure was followed for the preparation of $Fe_{0.1}Ni_{0.9}Co_2O_4$ and $Fe_{0.15}Ni_{0.35}Co_{2.5}O_4$ by a thermal decomposition method.

## 2.2 Characterization

The prepared materials were characterized to observe and confirm their morphology, compositions, crystalline phase, lattice parameters and their redox properties.

### 2.2.1. Scanning electron microscope (SEM)

Scanning electron microscopy is the most widely used type of powerful electron microscope for analyzing the morphology of organic and inorganic materials on a nanometer to micrometer scale. It examines microscopic structure by scanning an electron beam over the surface of materials and provides topographic and morphological information, which is necessary to understand surface behaviours. The SEM can also be used to obtain compositional information using characteristic X-rays signal emitted during irradiation.

### 2.2.1.1 The principle of scanning electron microscopy

In scanning electron microscopy, the electron beam emitted from the electron gun interacts with atoms in the specimen and produce various signals, which contain information about the sample's morphology. The most important feature of the SEM is the large depth of field that provides three dimensional and high resolution (1 nm – 5 nm) images [82].

### 2.2.1.2. Instrumentation

A scanning electron microscope consists of an electron gun, multiple electromagnetic lenses, apertures, and detector. A schematic of the electron microscope is shown in Figure 2.1. The electron gun generates electrons and accelerates them to energy from 0.1 to 10 keV [83]. The electron beam is then condensed to a fine probe for surface scanning. The two condenser lenses decrease the crossover diameter of the electron beam. The objective lens focuses the electron beam as a probe with a diameter of less than 10 nm. The beam passes through the aperture, which is a metal films that consists of micron-scale holes. The beam moves over the specimen and scans point - by - point until a rectangular area (raster) is generated. Simultaneously, the detector records the signal coming from the surface and an image is created on the viewing screen. The magnification (M) is determined by the ratio of the length of the raster on the viewing screen ($L_{view}$) to the corresponding length of the raster on the scanned specimen ($S_{pec}$). Therefore, the size of the area scanned on the specimen acts as a function of magnification. A 100 μm wide raster on the specimen displayed 10 cm wide viewing screen generates an image of 1,000X magnification. For our samples all SEM images were collected under high vacuum mode (ca. $3.35 \times 10^{-4}$ Pa).

There are two different types of scattering (inelastic and elastic) that occur when incoming electrons interact with the atom of the specimen. An inelastic scattering is produced when an incident electron transfers kinetic energy to an electron in the atom of the specimen.

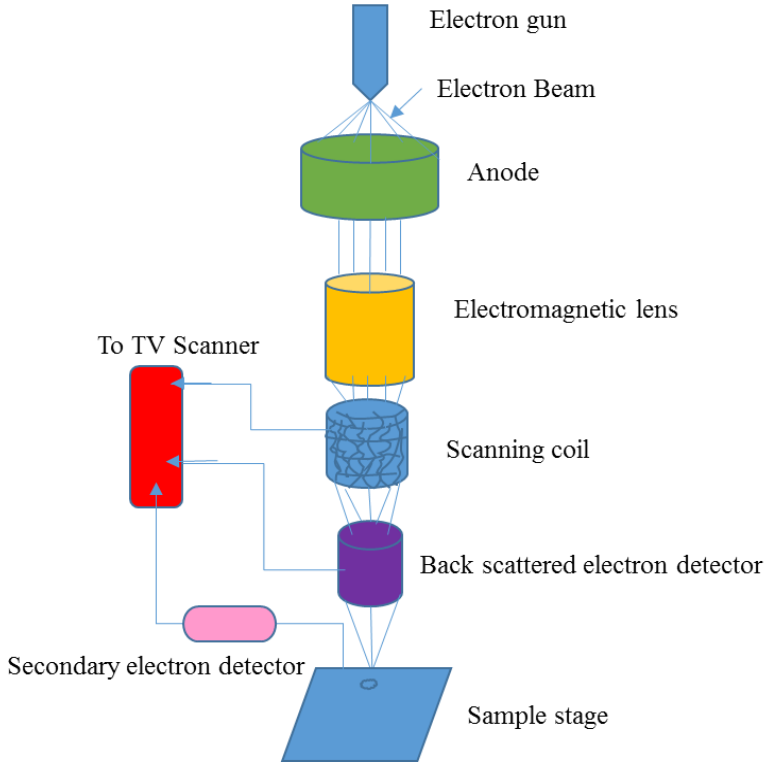


**Figure 2.1:** Schematic part of the scanning electron microscope (SEM), adapted from [84].

These higher energy electrons leave their orbital with a small deflection angle and produce a low energy electron (3 - 5 eV) called secondary electrons, which are useful for topographic information. On the other hand, the elastic scattering produces incident electrons scattered with a large angle by atoms in the specimen, called backscattered electrons. These electrons are useful for determining the composition of the specimens. The electron signals from the raster are collected by a detector. The SEM detector was designed to collect secondary electrons and backscattered electrons. The secondary electrons are detected by-Everhart and Thornley detectors (ETD). The main part of the ETD detector is a scintillator that has a fluorescent substance is coated on the tip of the detector and a high voltage (10 kV) is applied to it. When the secondary electrons from the specimen are attracted by this high voltage and hit by the scintillator, then the light is

generated. This light is directed to a photomultiplier and converted to electrons which are later amplified as an electrical signal, that then is displayed on a screen [82, 83]. Figure 2.2 shows a Scanning Electron Microscope (SEM - FEI, QUANTA 3D PEG) used in this work for topographic information of our prepared samples at York University.

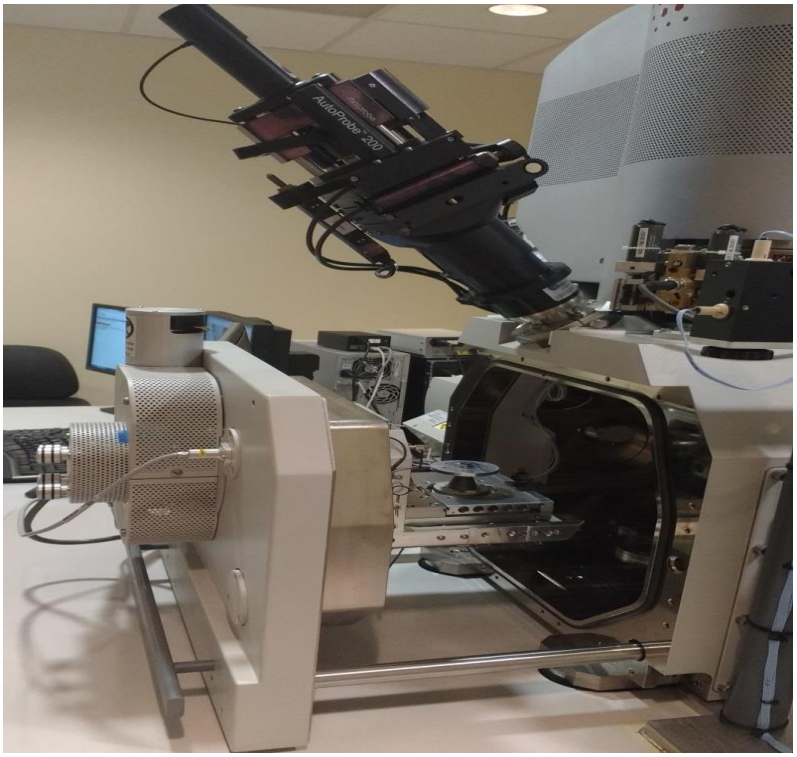

**Figure 2.2:** Picture of the loading chamber of the scanning electron microscope (SEM-FEI, QUANTA 3D) used in this work.

### 2.2.1.3. Sample preparation

For SEM and EDX analysis, the samples were prepared on (1.5 cm x 1.5 cm) FTO conductive glass, to avoid the charging effect. The charging, an accumulation of positive charge occurs, when a secondary electron is ejected away from the solid sample upon introduction of the incident electron. A small piece of carbon tape was placed between the sample holder and FTO glass so that the sample properly adhered to the sample holder.

## 2.2.2. Energy dispersive X-ray spectroscopy (EDX)

Energy dispersive X-ray spectroscopy is an electron microscope technique, suitable for the elemental analysis of microscopic volume which is known as microanalysis and their relative proportions in atomic percentage or weight percentage. The EDX system is attached to a scanning electron microscope (SEM). The primary electron beam is used to generate a characteristic X-ray from the tightly bound inner shell electrons of a specimen's atom.

### 2.2.2.1. Principle of Energy dispersive X-ray spectroscopy (EDX)

The principle of EDX is based on X-ray energy which is the characteristic of the element from which it was emitted. There are two basic types of X-ray produced when the interaction occurs between electron beams and atoms of the specimen.

The characteristic X-ray is generated when the beam radiation energy is high enough to knock out (eject) an electron from the inner shell (K) and the inner shell electron vacancy is filled by an outer shell (L or M) electron. The X-ray is emitted to balance the energy difference between the two electron states, which are characteristic of the particular atom [82, 83].

The atom consists of a central nucleus surrounded by electrons lying in various shells such as K, L, M, corresponds to the principal quantum number (n = 1, 2, 3, respectively), represented in Figure 2.3. It is possible to fill K shell vacancy from either L or M shell so that $K_\alpha$ or $K_\beta$ radiation can be emitted accordingly. Since the intensity of $K_\alpha$ ray is higher than that of $K_\beta$, it is possible to fill a K shell vacancy by an L shell electron rather than a M shell electron. The $K_\alpha$ characteristic contains two characteristic lines such as $K_{\alpha1}$ and $K_{\alpha2}$. The continuous X-ray must be filtered out in order to obtain monochromatic $K_\alpha$. However, in the diffraction radiation the $K_{\alpha1}$, $K_{\alpha2}$ and, $K_\beta$ are known as the three strongest characteristic X-rays shown in Figure 2.3.

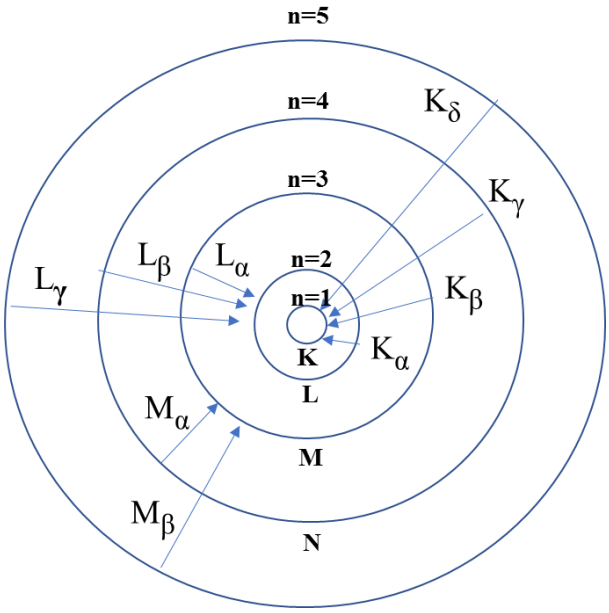


**Figure 2.3:** Electron transition that gives rise to *K*, *L*, *M*, and *N* characteristic X-rays detectable by EDX, adapted from [ 85].

### 2.2.2.2. Instrumentation

The EDX detector measures the relative abundance of emitted X-rays versus their energy. A solid-state Lithium- Silicon detector sometimes called a photon detector is used to separate the characteristic X-ray photons for better energy resolution. The Octane elects plus detector (by EDAX-AMETEX), 20 kV is used in this work for the elemental analysis of the specimens. When an incident X-ray strikes the detector, it creates a charge pulse that is proportional to the energy of the X-ray. The charge pulse is converted to a voltage pulse by a charge-sensitive amplifier, located close to the detector. Both detector and amplifier are cooled with liquid nitrogen to minimize electronic noise. Each incident X-ray is sent to a computer for display and further data evaluation. The spectrum of X-ray energy versus intensity is evaluated

to determine the elemental composition of the elements [3]. The beam current is directly related to X-ray intensity. The low beam current is suitable as some samples are prone to beam damage.

A typical EDX spectrum is plotted as an X-ray count vs. energy (keV). Energy peaks correspond to the various elements in the sample. Many elements yield multiple peaks such as iron commonly depicting strong $K_\alpha$ and $K_\beta$ peaks. Elements in low abundance will generate X-ray peaks that may not be resolvable from the background radiation. The background intensity is equivalent to the peak count. The more counts can be obtained by either increasing the counting time or increasing the beam current. In EDX analysis, the detection limit must be reduced in order to have an increased more count. The detection limit is normally 0.1%. Heavy elements give higher detection limits due to peak to higher background ratio. The lightest elements hardly can be detected by EDX. However, this disadvantage can be outweighed by the advantages of the EDX system such as low cost and fast analysis. The EDX analysis is useful for qualitative analysis because a complete spectrum can be obtained within a short period of time.

#### 2.2.2.3. Sample preparation

The sample preparation was the same as the SEM sample preparation.

### 2.2.3. X-ray diffraction (XRD)

X-ray diffraction was discovered by Von Laue, Friederichs, and Kneipping in 1912. Using the crystal of $CuSO_4$ and ZnS, they demonstrated that crystals can diffract X-rays. In 1913, Henry and Bragg applied X-rays to solve the first crystal structure and the Bragg equation was derived.

### 2.2.3.1. The principle of X-ray diffraction (XRD)

XRD is a rapid analytical technique used for material characterization, such as phase identification of the structure of a crystalline material, grain size and obtaining information on unit cell dimensions. Crystalline materials possess a regular arrangement of atoms, molecules or ions with an interatomic distance of the order of 100 picometers (pm). The diffraction patterns are produced when the spacing between the planes is the same order of the wave length of the X-ray. According to Bragg's law, the diffraction pattern obtained can tell us about the internal arrangement of atoms in crystal planes [86]. Bragg's Law state that:

$$n\lambda = 2d_{hkl} \sin \theta \qquad (8)$$

where $\lambda$ = incident wavelength (defined by the X-ray tube used), $d_{hkl}$ = spacing between atomic planes, $\theta$ = incident angle and n = the order of the diffracted beam. The spacing between the planes is the same order of magnitude as the wavelength of the X-rays. Diffraction occurs only when Bragg's law has satisfied the condition for constructive interference from planes with spacing $d_{hkl,}$ where h, k, and l are Miller indices, such as the series of parallel planes with a d spacing [86, 87] shown in Figure 2.4. In the face-centred cubic lattice, h, k, l diffractions, such as (111), (200), (220), (311), (222), (331), are present. The peak position in terms of 2$\theta$ is defined by the lattice spacing d. The peak intensities are defined by the geometrical and elemental structure of the lattice. For a cubic crystal lattice parameter ($a_0$) can be calculated from the plane (220) and (311), i.e., peaks of highest intensity, from the equation:

$$(a_0) = d_{hkl} (h^2 + k^2 + l^2)^{1/2} \qquad (9)$$

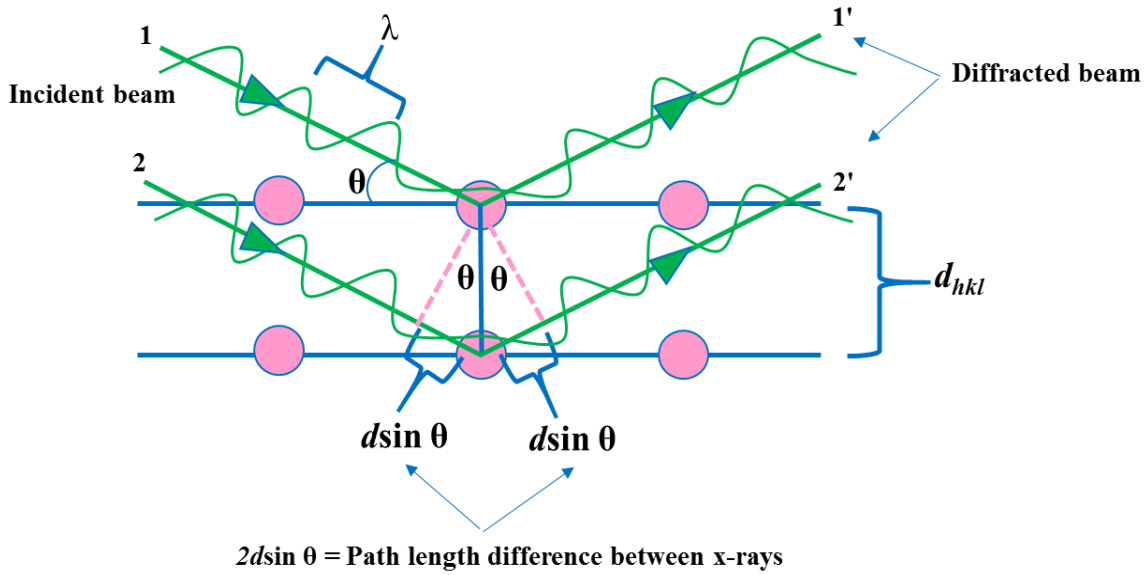


**Figure 2.4:** Bragg reflection from a set of crystal planes, adapted from [83], p - 50.

### 2.2.3.2. Instrumentation

The X-ray diffractometer detects X-ray diffraction from materials and records the diffraction intensity as a function of the diffraction angle (2θ). The diffractometer consists of an X-ray source, a specimen holder, and a detector. The X-ray diffractometer is shown in Figure 2.5 [83]. The X-ray produced from the cobalt sealed tube source - Co $K_\alpha$ ($\lambda$ = 1.79026 Å) Bruker D8 DISCOVER, are diffracted from the sample; resultant diffracted beams are formed. The diffracted beams pass through the monochromatic filter before entering the detector so that only $K_\alpha$ radiation can reach the detector and background radiation can be reduced. The intensity of the diffracted beam is measured directly by the detector in a range of 2θ [83, 86]. It is noted that the θ angle is the angle between the incident beam and the crystallographic plane, not specimen surface, that generates the diffraction. The XRD data were collected using the Bruker D8 DISCOVER with DAVINCI. DESIGN diffractometer, detector: Vantec 500 (MikroGap TM technology) shown in

Figure 2.6. Data was collected with DEFRA center version 3.0 software. The unit cell refinements were carried out using Topas Version 4.0 software. The Rietveld refinement method was used in the characterization of crystalline materials because it can deal with overlapping reflections. This instrument was run by Victoria Jarvis (XRD specialist) at McMaster University.

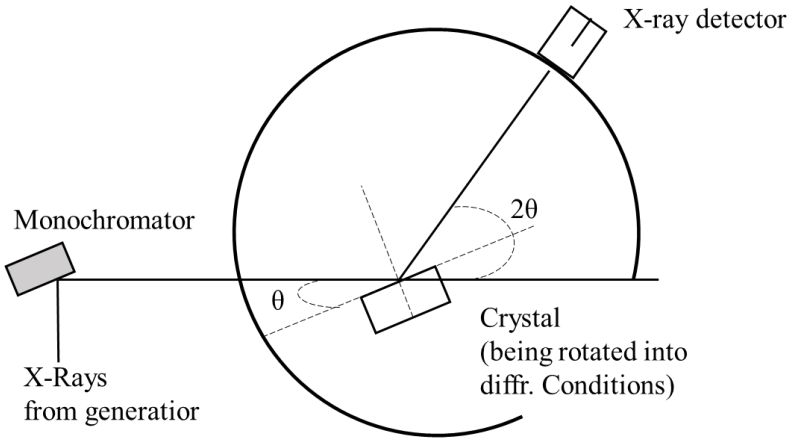


**Figure 2.5:** Geometric arrangement of X-ray diffractometer, adapted from [83], p- 59.

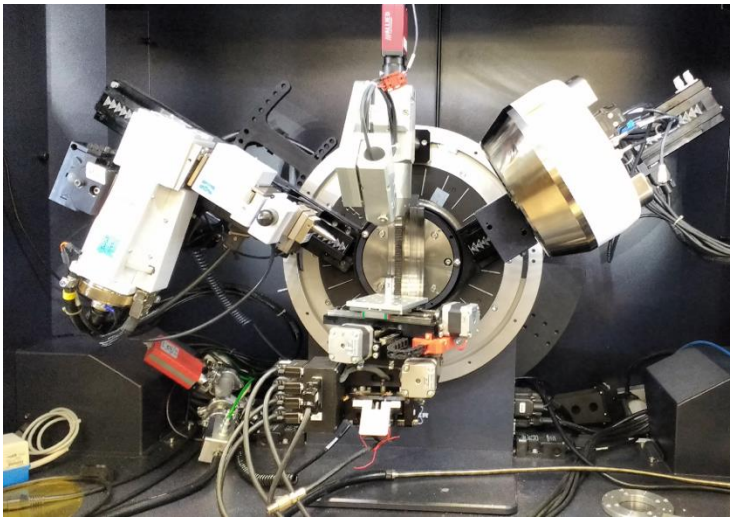

**Figure 2.6:** Picture of Bruker D8 - diffractometer used in this work (Picture from McMaster University)

### 2.2.3.3. Sample preparation

For XRD analysis the materials were deposited on 1 $cm^2$ nonconductive glass. Nonconductive glass was used to avoid detecting other crystalline phases, such as fluorine doped tin oxide present in the conductive glass employed in our work.

### 2.2.4.1 Cyclic Voltammetry (CV)

Cyclic voltammograms (CV) represent current as a function of the potential difference between the reference and working electrodes in an electrochemical cell as the potential is cycled between two pre-set values. It has the ability to provide information about the redox potential of electroactive species, the kinetics of electron transfer reaction, and adsorption processes. When a potential is applied, the presence of electrochemical processes at the working electrode are usually identifiable by the presence of characteristic peaks in the CV (see example shown in Figure 2.7 for the oxidation/reduction of a redox pair in solution).

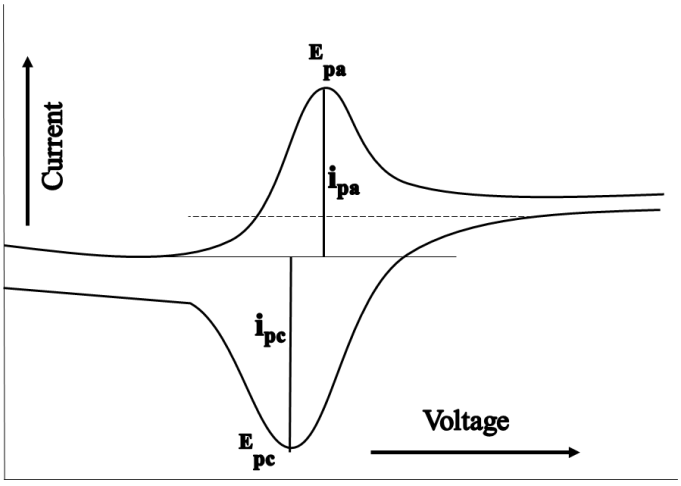


**Figure 2.7:** A typical Voltammogram for redox species in solution ($E_{pc}$=cathodic peak potential, $E_{pa}$= anodic peak potential $i_{pc}$ = cathodic peak current, and $i_{pa}$ = anodic peak current), adapted from [88], p- 45.

### 2.2.4.2. Principle of Cyclic Voltammetry in the context of capacitance measurements

An electrode at which no charge transfer occurs across the metal- solution interface when the potential is imposed, called an ideally-polarized electrode. This type of behaviour is analogous to that of a capacitor. A capacitor consists of two metal plates separated by dielectric material and its response to an applied potential is governed by the following equation [60]:

$$C = q/E \qquad (10)$$

where q is charge stored on the plates of the capacitor, expressed in coulomb (C); E is the potential across the capacitor in Volt (V); and C is the capacitance in Farad (F). At a given potential, a charge on the metal electrode and the opposite compensating charge can exist in the solution near the electrode surface. These charges are divided by the electrode area and expressed as capacitance ($\mu C/cm^2$). The somewhat structured arrangement of charged species and solvent dipoles at the metal - solution interface is called the electrical double layer. The electrode – solution interface is characterized by a double layer capacitance ($C_{dl}$ ), typically in the range of (10 - 60 $\mu F/cm^2$) [60].

A capacitive charging current density ($j_{cap}$) is generated at any interface between the two phases, electrode and electrolyte, when positive and negative charges are accumulated. In a cyclic voltammetry experiment, the capacitive charging current density ($j_{cap}$) is directly proportional to the scan rate and can be expressed by the following equation, [88, 89]:

$$(j_{cap})/A = (dq/dt)/A = C_{dl} \,.\, (dE/dt) = C_{dl} \,.v \qquad (11)$$

where q is the charge, t is time , A is the area of the working electrode, E is the applied potential, $C_{dl}$ is the double layer capacitance per unit area, and dE/dt = v is the scan rate[90, 88]. The faster the scan rate, the thinner the diffusion layer. The capacitive current is the largest at higher scan

rates. On the other hand, the faradaic current due to oxidation and reduction processes is proportional to the square root of the scan rate [90].

The roughness factor can be calculated by taking the ratio of double layer capacitance of the sample and double layer capacitance of a smooth electrode. Both anodic and cathodic capacitive current densities were plotted against the different sweep rates for a narrow potential range (-100 mV to 100 mV). Then the average slope was calculated, which is equal to the double layer capacitance in Farads (F). The average slope was divided by 60 x $10^{-6}$ F in order to get the roughness factor.

$R_f = A_r / A_g$ ($A_r$ = real surface area , $A_g$ = geometric surface area ) *(12)*

Or

$R_f = C_{dl} / C_{dl(smooth)}$ ($C_{dl}$ = the double layer capacitance of the sample, $C_{dl(smooth)}$ = the double layer capacitance of smooth surface.

The error in the roughness factor was calculated using the following equation:

$\Delta R_f = R_f [(\Delta \text{ slope} / \text{Avg. slope}) + (\Delta C_{dl\ \text{Smooth surface}} / C_{dl\ \text{smooth surface}})]$ *(13)*

The error in the slope ($\Delta$ slope) can be calculated by taking the standard deviation of anodic and cathodic slopes. The error in the double layer capacitance of smooth surface ($\Delta C_{dl\ \text{Smooth surface}}$ ) is assumed to be 6 μF $cm^{-2}$ and the double layer capacitance of smooth surface is assumed to have 60 μF $cm^{-2}$ . A relative error of 10% of a double layer capacitance for smooth surface was taken for the calculation of errors in the roughness factor.

### 2.2.4.3. Principle of Cyclic Voltammetry in the context of the identification of the electrochemical process

Cyclic Voltammetry is a type of analytical technique generally used for the study redox processes and electrochemical properties of an analyte in solution. In cyclic voltammetry, the

sweep rate is reversed at a predetermine potential value (switching potential). Since the initial and switching potential is known and the sweep rate is constant, therefore the current versus potential can be recorded easily in a cyclical fashion. The cyclic voltammogram of $Ni_{1-x}Cu_xCo_2O_4$ with various compositions provides us the information about redox potential, the corresponding current and how the electrocatalytic properties of the film can be affected by a concentration of the analyte, sweep rate or temperature.

Oxidation or reduction of the material at the working electrode results in the generation of the current. During the anodic process a positive current can be measured, since the increase in potential can result in the oxidation of electroactive species due to the loss of electrons. On the other hand, during a negative scan (decrease of the potential), a negative current appears and electroactive species can be reduced by the gain of electrons. The response current gives information about electron transfer mechanism at the electrode solution interface [91]. When electron transfer at the electrode surface is fast compared to mass transport, the process is called electrochemically reversible. In a reversible CV, the rate of electron transfer is controlled by diffusion and the peak potential is independent of scan rate. The ratio of cathodic to anodic current is constant at all different scan rates. An electron transfer process in the reversible reaction [88, 89] at the electrode can be expressed as,

$$O + ne^- \rightleftharpoons R \qquad (14)$$

Where O, R, and n are oxidized forms of electroactive species, the reduced form of electroactive species and the number of electrons is transferred in the reaction, respectively. These electroactive species are either soluble in solution, adsorbed on the electrode surface or transported by diffusion alone. In reversible cyclic voltammograms, both O and R are stable, and the kinetic process is fast so that the electron transfer processes on the surface are at equilibrium [91].

## 2.2.4.4. Instrumentation

The main components of the cyclic voltammetry are the electrode cell, potentiostat, generator, and the computer. An electrochemical cell is made up of three electrodes immersed in a solution containing the supporting electrolyte, shown in Figure2.8. One of the three electrodes is the working electrode, whose potential is varied linearly with time. Its dimensions are kept small so that it can polarize easily. The second electrode is a reference electrode and has stable equilibrium potential which is independent of the electrolyte used in the cell. There are few commonly used electrodes available such as silver/used electrode silver chloride (Ag/AgCl) electrode or a saturated calomel electrode, whose potential remains constant during the experiment. The saturated Calomel electrode potential is + 0.242 V vs. the standard hydrogen electrode (SHE).

The half- cell reaction of both electrodes [88, 89] can be written as,

$$AgCl_{(solid)} + e^- \rightleftharpoons Ag_{(solid)} + Cl^-_{(solution)} \quad (15)$$

$$\tfrac{1}{2} Hg_2Cl_{2(solid)} + e^- \rightleftharpoons Hg_{(liquid)} + Cl^-_{(solution)} \quad (16)$$

The third electrode is a counter electrode, which is often a platinum grid or coiled wire. The purpose of the counter electrode is to complete the electrical circuit, when a potential is applied, the same amount of current flows to the counter electrode but with the opposite sign. It is important for this electrode to be of higher surface area than the working electrode so that the current density remains low (and hence side reaction is avoided). The potentiostat is used to control the applied potential of the working electrode. The applied potential is measured as the potential difference between the working and the reference electrodes. The electrodes are

connected to the potentiostat and the experimental parameters are selected through the potentiostat software (Volta lab –PGZ-402).

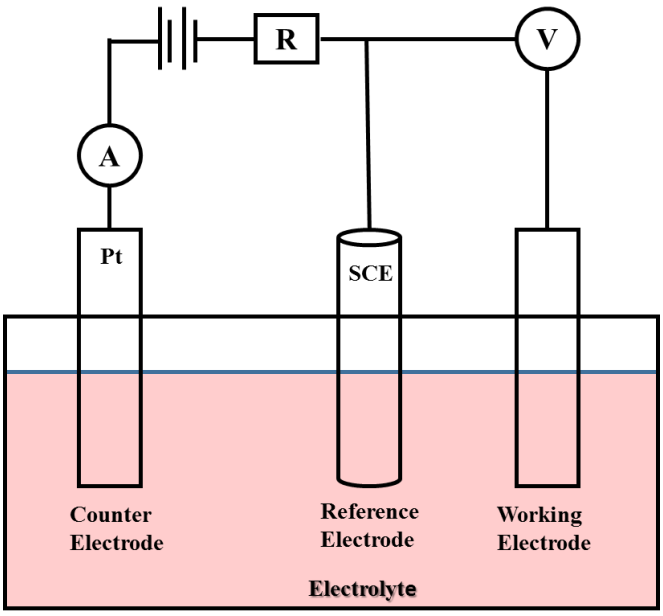


**Figure 2.8:** Three electrode cell diagram, adapted from [88], p - 34.

## 2.2.4.5. Sample preparation

For CV analysis the materials were deposited on pre-treated (1.5 cm x 1.5 cm) FTO conductive glass. 1M KOH electrolyte solution was used in order to perform cyclic voltammetry analysis. The electron transfer rate, and the catalytic activity depend on the concentration of the electrolyte. Three electrodes chemical cell (vessel) was prepared to perform CV experiments.

## 2.2.4.6. Reproducibility measurement and electrocatalysis

For this research, we were interested to check the consistency of our experimental technique, therefore reproducibility measurement was performed. Reproducibility is one of the

most important parameters in the research field to check whether the experimental parameters provide the same result consistently. In this work, obtained data are discussed for samples prepared March 26$^{th}$, 2019 (denoted as 2019), and samples prepared in different months in 2018 namely February 23$^{rd}$, 2018 and October 5$^{th}$, 2018 labeled as 2018a and 2018b, respectively. The results from this analysis can be a resource for other researchers to be able to reproduce similar research and reduce errors. When we ensure reproducibility, we can provide transparency with our experimental data and provide a reference to others to understand what was done, and if the information would be helpful for future research. This applies to reporting on an experiment performance, techniques, and tools used for data collection method and analysis. In this work we have tested true catalytic activity, elemental composition and surface morphology for the samples prepared on different dates.

## 2.3. Conclusion

In this chapter, we highlighted our methodology and characterization techniques. In the methodology section, we expanded more about the preparation of precursor solution for the thermal decomposition method as well as preparation of electrolyte solution for the cyclic voltammetry analysis. The characterization section discussed the different instruments used in this research, such as SEM, EDX, XRD and CV and their principles. In addition, the importance of our reproducibility measurement was mentioned.

# Chapter 3 - Spinel oxide characterization- Results and Discussion

## 3.1 Introduction

Spinel metal oxides are semiconductors surfaces which are of important for different electrocatalytic reactions such as electrolysis of water at the surface, leading to oxygen evolution. Research of this sort are important in clean and renewable energy source [61]. Different metal oxides ($Ni_{1-x}Cu_xCo_2O_4$, $Fe_yCu_{x-y}Co_{3-x}O_4$ and $Fe_yNi_{x-y}Co_{3-x}O_4$) were prepared in this work, to investigate the different parameters (i.e. different metal, concentrations and temperature) required to optimize the electrocatalytic activity of the prepared samples. Characterization of the prepared surfaces are of importance to determine the surface properties of the materials, such as morphology, composition and lattice parameters. This will be crucial for understanding the effect of this parameters on the electrolytic reaction via cyclic voltammetry. In this chapter, the spinel oxides prepared from this work will be characterized by scanning electron microscope (SEM), energy dispersive X-ray spectroscopy (EDX), and X-ray diffraction (XRD). The results will be discussed accordingly.

## 3.2 Film morphology – Scanning electron microscopy

The surface morphology of the $Ni_{1-x}Cu_xCo_2O_4$ ($0 \leq x \leq 0.75$) and $Fe_yCu_{x-y}Co_{3-x}O_4$, $Fe_yNi_{x-y}Co_{3-x}O_4$, ($0.15 \leq x \leq 1.0$) electrodes prepared by thermal decomposition method at various composition were analyzed by scanning electron microscopy (SEM). In figures 3.1 and 3.2 are the SEM micrographs of all prepared $Ni_{1-x}Cu_xCo_2O_4$ spinel oxides, showing the surface morphology.

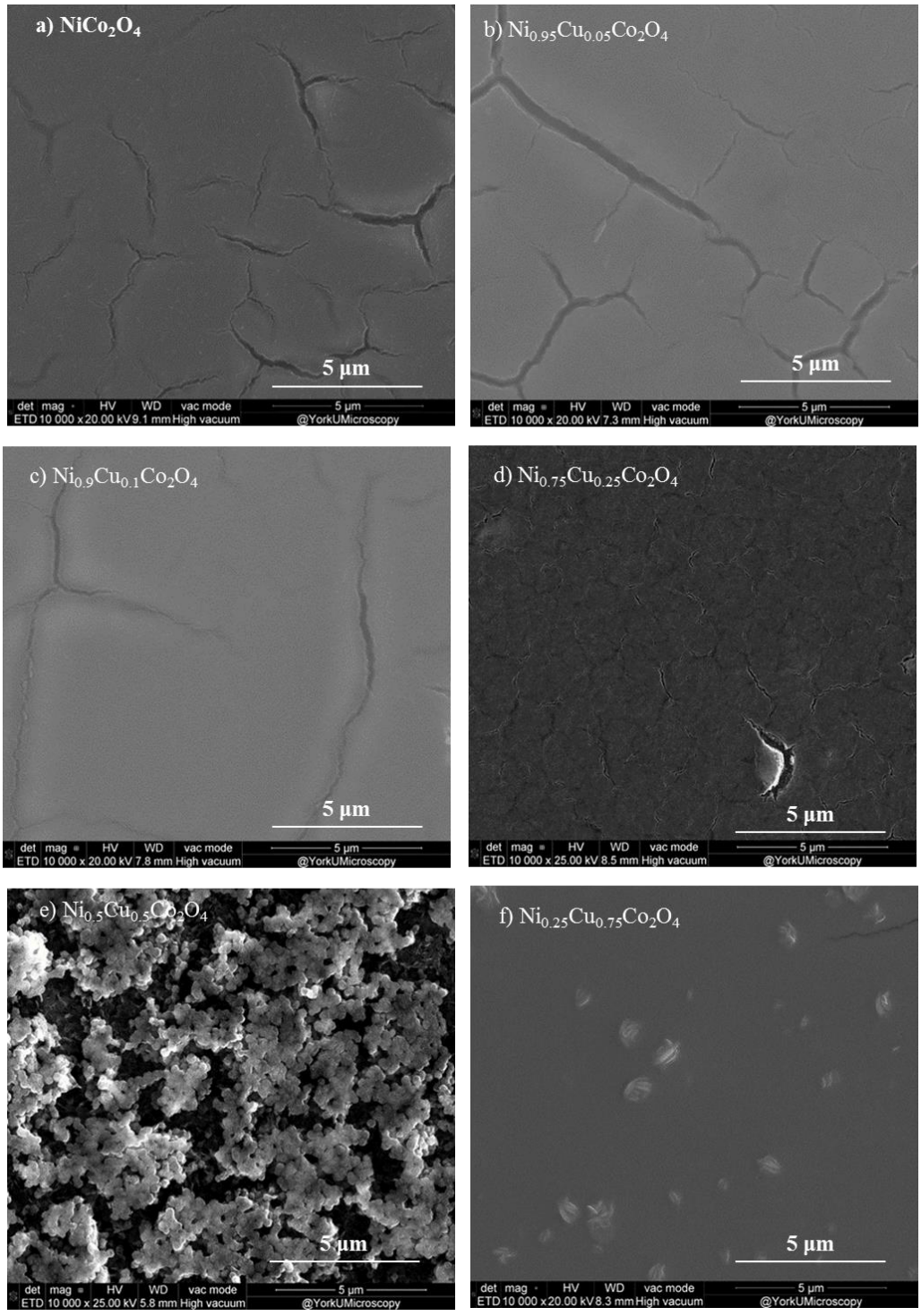


**Figure 3.1:** SEM micrograph showing the morphology of the different spinel oxide composition a) $NiCo_2O_4$, b) $Ni_{0.95}Cu_{0.05}Co_2O_4$, c) $Ni_{0.9}Cu_{0.1}Co_2O_4$, d) $Ni_{0.75}Cu_{0.25}Co_2O_4$, e) $Ni_{0.5}Cu_{0.5}Co_2O_4$, f) $Ni_{0.25}Cu_{0.75}Co_2O_4$. Image size is 15µm.

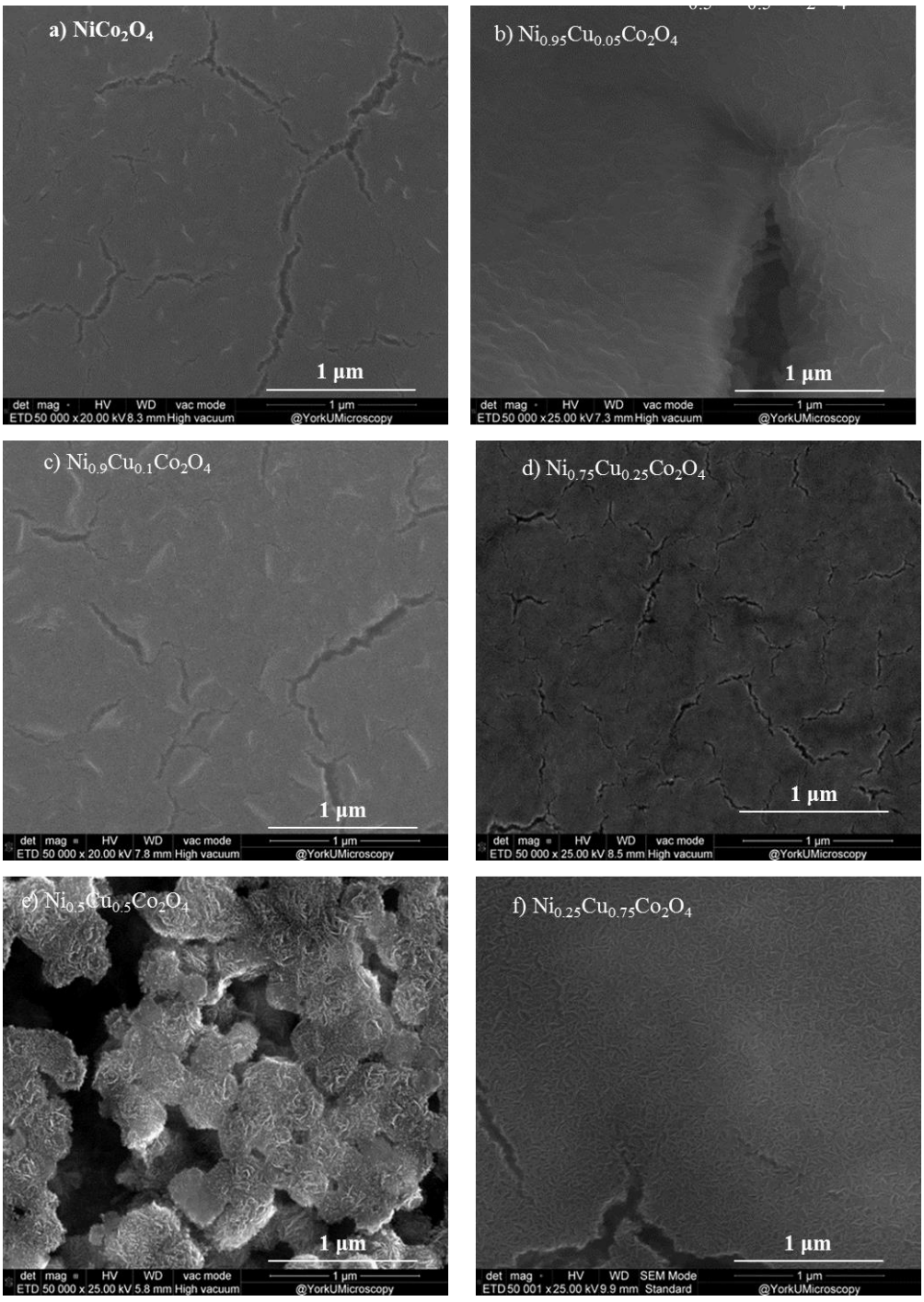


**Figure 3.2:** SEM micrograph showing the morphology of the different spinel oxide composition a) $NiCo_2O_4$, b) $Ni_{0.95}Cu_{0.05}Co_2O_4$, c) $Ni_{0.9}Cu_{0.1}Co_2O_4$, d) $Ni_{0.75}Cu_{0.25}Co_2O_4$, e) $Ni_{0.5}Cu_{0.5}Co_2O_4$, f) $Ni_{0.25}Cu_{0.75}Co_2O_4$. Image size is 3µm.

SEM allows the comparison of the surface porosity of the different spinel oxides, which is an important factor for electrocatalytic activity. Two different imaging sizes were chosen for a better understanding of the surface morphology for all prepared electrodes by thermal decomposition method are shown in Figure.3.1 and Figure 3.2. The SEM images show significant changes with copper substitution. A smooth surface is observed in the case of $NiCo_2O_4$ electrode, and as we introduce and increase copper content the surfaces display more porous morphology. In the SEM image of the spinel oxide with the $Ni_{0.5}Cu_{0.5}Co_2O_4$ (Figure 3.2e) grains are visible. Also, when substitute the Ni for Fe in order to compare the electrocatalytic of a different metal at different concentration. Figure 3.3 and 3.4 shows the SEM images of the Fe substituted spinel oxide complexes. The morphology of $Fe_{0.1}Cu_{0.9}Co_2O_4$ ternary spinel oxides exhibit porous surfaces and grain are uniformly distributed over the whole area of the sample. This porosity may increase both the density of active sites and the surface area.

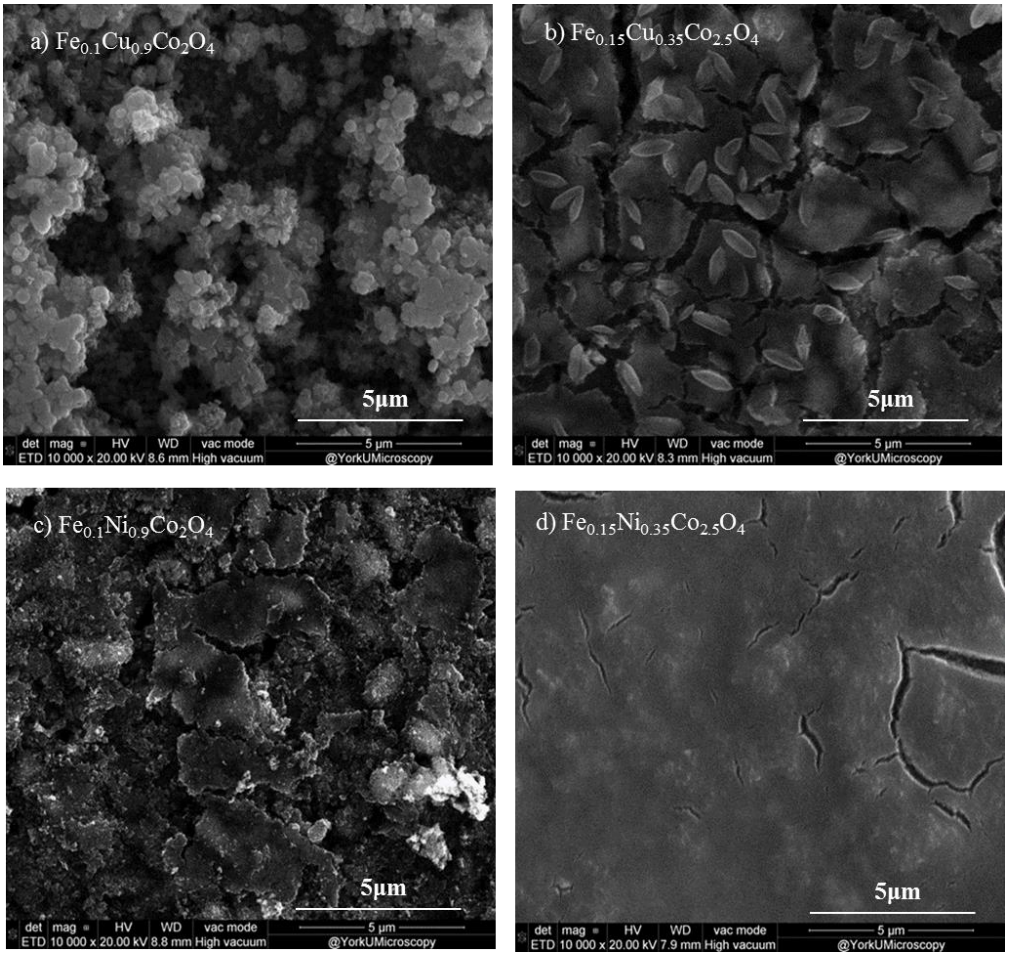


**Figure 3.3:** SEM micrographs showing the morphology of prepared spinel oxide electrodes by thermal decomposition method. a) $Fe_{0.1}Cu_{0.9}Co_2O_4$, b) $Fe_{0.15}Cu_{0.35}Co_{2.5}O_4$, c) $Fe_{0.1}Ni_{0.9}Co_2O_4$, d) $Fe_{0.15}Ni_{0.35}Co_{2.5}O_4$. Image size is 15µm.

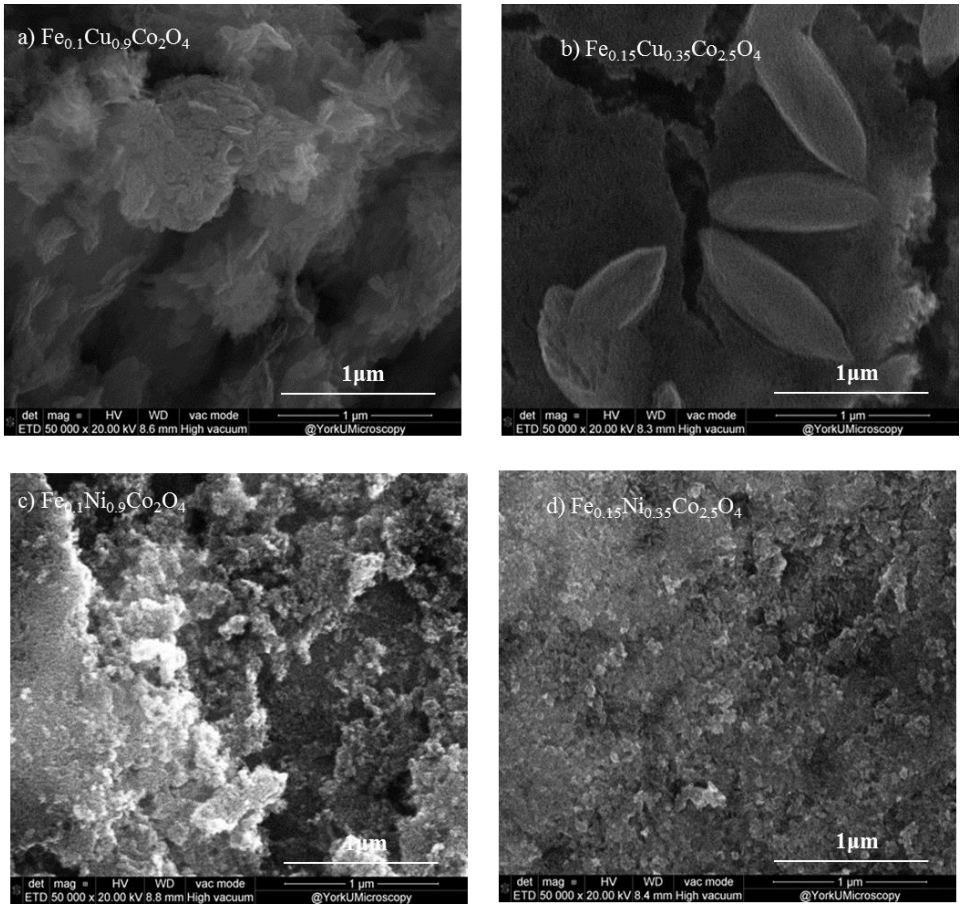


**Figure 3.4:** SEM micrographs showing the morphology of prepared spinel oxide electrodes by thermal decomposition method. a) $Fe_{0.1}Cu_{0.9}Co_2O_4$, b) $Fe_{0.15}Cu_{0.35}Co_{2.5}O_4$, c) $Fe_{0.1}Ni_{0.9}Co_2O_4$, d) $Fe_{0.15}Ni_{0.35}Co_{2.5}O_4$. Image size is 3µm.

## 3.3. Electrode composition - energy Dispersion X-ray spectroscopy (EDX)

Energy Dispersion X - ray spectroscopy provides a way to identify the elements that are present in the specimen and their relative proportions such as atomic %, and weight %. The elemental analysis of the $Ni_{1-x}Cu_xCo_2O_4$ and $Fe_yCu_{x-y}Co_{3-x}O_4$, $Fe_yNi_{x-y}Co_{3-x}O_4$, ternary spinel oxide was performed by EDX. The EDX spectra shown in Figure 3.5 and Figure 3.6 display all similar elements corresponding to the elements in the prepared spinel oxide complex. The Fe containing spinel oxide complexes shows the presence of iron (see Figure 3.6 a) and b)). All EDX spectra also shows an additional peak of tin (Sn) that originates from FTO glass on which the samples were deposited. EDX analysis of the prepared $Ni_{1-x}Cu_xCo_2O_4$, $Fe_yCu_{x-y}Co_{3-x}O_4$,and $Fe_yNi_{x-y}Co_{3-x}O_4$, electrodes allow the determination of the elemental ratios to compare the stoichiometric and EDX elemental compositions. The stoichiometric ratio and EDX analysis ratio of Ni/Co and Fe/Co are summarized in Table 3.1 (a) and Table 3.1(b), respectively. The ratio calculated from the EDX analysis for $Ni_{1-x}Cu_xCo_2O_4$ electrodes are relatively close to the ratio from stoichiometric calculations. However, in the case of $Fe_yCu_{x-y}Co_{3-x}O_4$,and $Fe_yNi_{x-y}Co_{3-x}O_4$ electrodes, EDX compositions does not correlate with stoichiometric values very well. To evaluate the error from the EDX analysis, three different spots of the same sample was chosen for the nickel -cobalt ratio or iron -cobalt ratio measurements. Eventually the standard deviations and relative errors were calculated. The resulting errors associated with the Ni/Co Fe/Co ratios are ranging from 0.6 to 2.4% and from 2.6 to 3.1%, respectively.

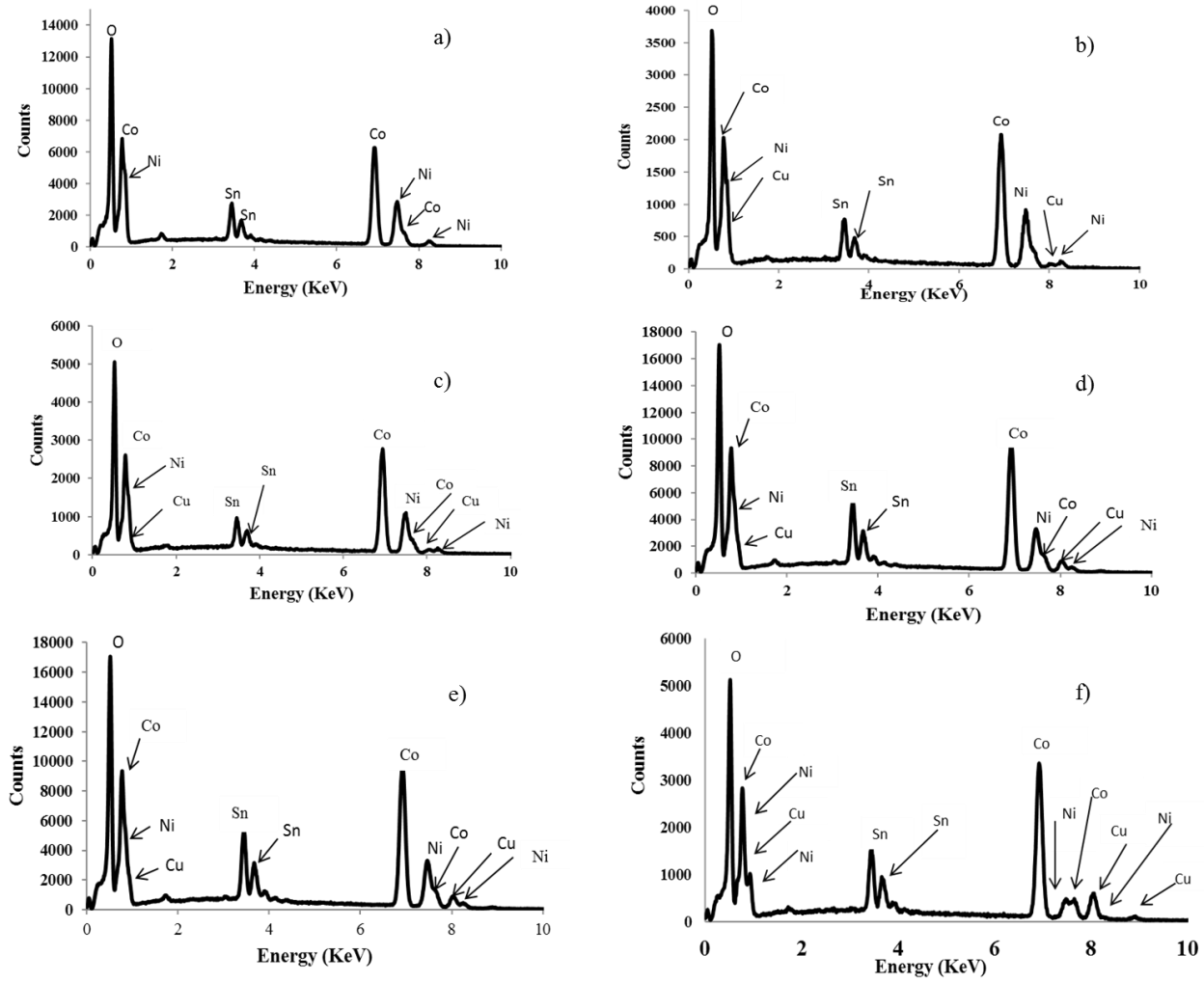


**Figure 3.5:** EDX spectra of a) $NiCo_2O_4$, b) $Ni_{0.95}Cu_{0.05}Co_2O_4$, c) $Ni_{0.9}Cu_{0.1}Co_2O_4$, d) $Ni_{0.75}Cu_{0.25}Co_2O_4$, e) $Ni_{0.5}Cu_{0.5}Co_2O_4$, f) $Ni_{0.25}Cu_{0.75}Co_2O_4$ electrodes.

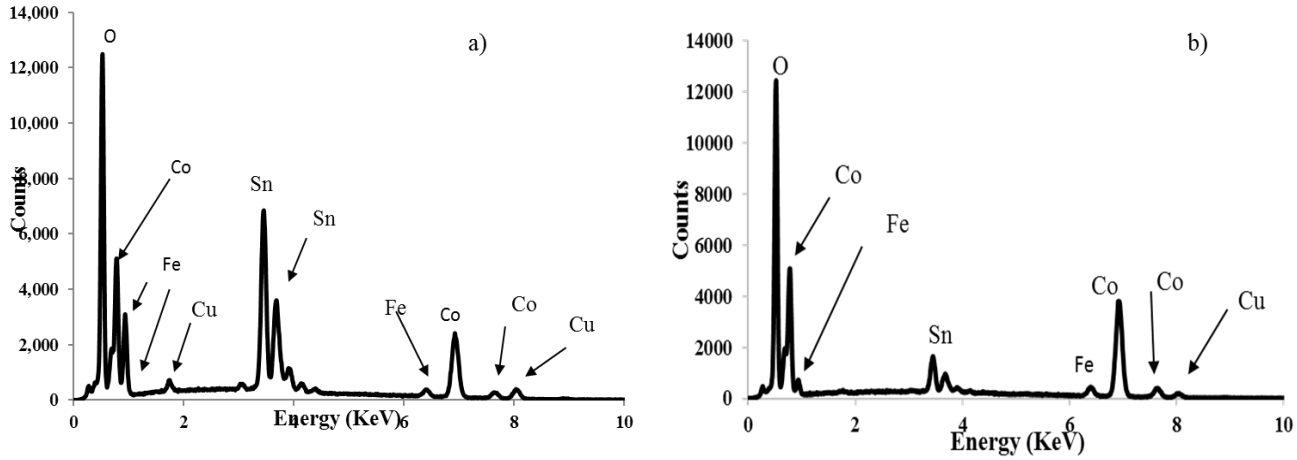


**Figure 3.6:** EDX spectra of a) $Fe_{0.1}Cu_{0.9}Co_2O_4$, and b) $Fe_{0.15}Cu_{0.35}Co_{2.5}O_4$.

**Table 3.1 (a):** Stoichiometric composition and EDX composition of Ni/Co.

| Composition | Stoichiometric ratio (Ni/Co) | EDX ratio (Ni/Co) | Composition determined by EDX | Relative error % |
|---|---|---|---|---|
| $NiCo_2O_4$ | 0.500 | 0. 492 ± 0.004 | $Ni_{0.99}Co_{1.99}O_4$ | 0.8 |
| $Ni_{0.95}Cu_{0.05}Co_2O_4$ | 0.475 | 0.461 ± 0.003 | $Ni_{0.95}Cu_{0.05}Co_{2.06}O_4$ | 0.6 |
| $Ni_{0.9}Cu_{0.1}Co_2O_4$ | 0.450 | 0.425 ± 0.006 | $Ni_{0.91}Cu_{0.06}Co_{2.12}O_4$ | 1.4 |
| $Ni_{0.75}Cu_{0.25}Co_2O_4$ | 0.375 | 0.356 ± 0.004 | $Ni_{0.74}Cu_{0.22}Co_{2.12}O_4$ | 1.2 |
| $Ni_{0.5}Cu_{0.5}Co_2O_4$ | 0.250 | 0.219 ± 0.002 | $Ni_{0.48}Cu_{0.29}Co_{2.24}O_4$ | 1.1 |
| $Ni_{0.25}Cu_{0.75}Co_2O_4$ | 0.125 | 0.123 ± 0.003 | $Ni_{0.29}Cu_{0.55}Co_{2.3}O_4$ | 2.4 |

**Table 3.1 (b):** Stoichiometric composition and EDX composition of Fe/Co.

| Composition | Stoichiometric ratio (Fe/Co) | EDX ratio (Fe/Co) | Composition determined by EDX | Relative error % |
|---|---|---|---|---|
| $Fe_{0.1}Cu_{0.9}Co_2O_4$ | 0.050 | 0.094 ± 0.003 | $Fe_{0.22}Cu_{0.41}Co_{2.35}O_4$ | 3.1 |
| $Fe_{0.15}Cu_{0.35}Co_{2.5}O_4$ | 0.060 | 0.080 ± 0.002 | $Fe_{0.21}Cu_{0.13}Co_{2.61}O_4$ | 2.6 |

## 3.4. Film structure - X-ray diffraction

The X-ray powder diffraction method provides information about the crystalline structure and atomic arrangement of the solid samples. Moreover, the phase identification and lattice parameters can be obtained from the X-ray analysis. The X-ray diffraction patterns of $Ni_{1-x}Cu_xCo_2O_4$ and $Fe_yCu_{x-y}Co_{3-x}O_4$ spinel oxides electrodes provides information on how the substitution of copper by nickel or iron change the structure of the lattice. In Figure 3.7 (A) and Figure 3.7 (B) is shown the XRD spectra for the prepared spinel oxide electrodes. XRD pattern of $Co_3O_4$ exhibits characteristic peaks of the cubic spinel structure with the space group Fd3m. The identification of a sample structure from its X-ray diffraction pattern is based on the position of the lines (in terms of 2θ) and their relative intensities. The following peaks (111), (220), (311), (222), (400), (422), (511), and (440) are assigned to the planes a cubic cobalt spinel structure [76].

All our $Ni_{1-x}Cu_xCo_2O_4$ electrode materials show similar XRD patterns (Figure 3.7A) confirming the formation of the cubic spinel structure (Fd3m space group). XRD pattern of $Fe_{0.1}Ni_{0.9}Co_2O_4$ shows NiO (5.8%) cubic phase along with the spinel structure. This could be due to the higher nickel content (0.9) in the sample [92]. Similarly, in $Fe_{0.1}Cu_{0.9}Co_2O_4$ sample 3.1% of monoclinic CuO phase (Figure 3.7B) was formed at a higher copper content (x-y = 0.9, which corresponds to 30% copper in the sample) in the sample.

The lattice parameters ($a_0$) were calculated from the d spacing of the (311) plane, because it has the highest intensity, using the following formula (8) given in Section 2.2.3.1. of Chapter 2. The lattice parameters of $NiCo_2O_4$ found to be 8.1260 ± 0.0004 Å was much closer to the standard JCPDS values of 8.1280 ± 0.002 Å [88].

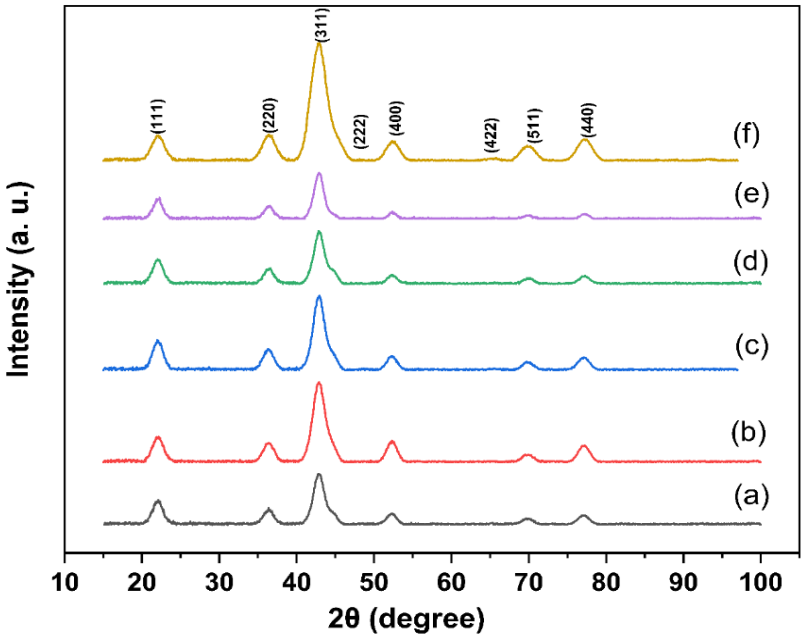


**Figure 3.7 (A):** XRD pattern of (a) $NiCo_2O_4$, (b) $Ni_{0.95}Cu_{0.05}Co_2O_4$, (c) $Ni_{0.9}Cu_{0.1}Co_2O_4$, (d) $Ni_{0.75}Cu_{0.25}Co_2O_4$, (e) $Ni_{0.5}Cu_{0.5}Co_2O_4$, (f) $Ni_{0.25}Cu_{0.75}Co_2O_4$ solid thin films deposited on glass annealed at 300° C for 1hour. For these samples, a total of twelve layers were deposited

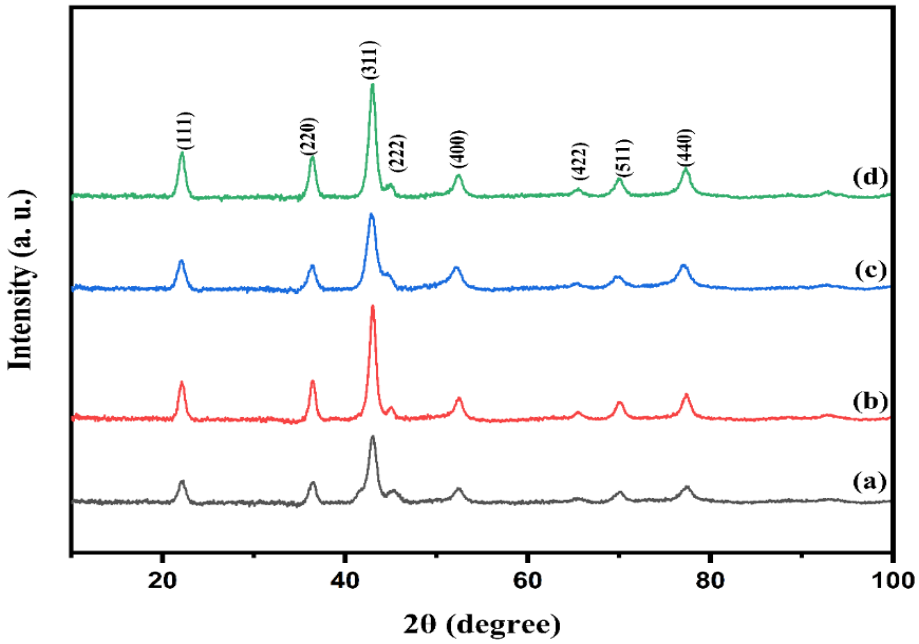


**Figure 3.7 (B):** XRD pattern of a) $Fe_{0.1}Cu_{0.9}Co_2O_4$, b) $Fe_{0.15}Cu_{0.35}Co_{2.5}O_4$, c) $Fe_{0.1}Ni_{0.9}Co_2O_4$, d) $Fe_{0.15}Ni_{0.35}Co_{2.5}O_4$ solid thin films deposited on glass annealed at 400° C for 2hour. For these samples, a total of twelve layers were deposited.

The error associated with lattice parameter was obtained by Reitveld refinement using duplicate measurement (Provided by Jarvis Victoria, XRD technician, McMaster University). Our lattice parameter values were compared with that obtained by Tavares *et al.* [53] and Ting *et al.* [59], our values are found to be higher( see Table 3.2). However, these authors did not report any error values. Increase in the lattice parameters of the ternary oxides can be attributed to the Ni and Fe cation substitution in the $CuCo_2O_4$ and $NiCo_2O_4$ oxide matrix respectively leading to the lattice expansion observed (see also ref 61).

**Table 3.2: The lattice parameter of $Ni_{1-x}Cu_xCo_2O_4$ ($0 \leq x \leq 0.75$), $Fe_y(Ni/Cu)_{x-y}Co_{3-x}O_4$ [($0.5 \leq x \leq 1$), ($0.1 \leq y \leq 0.15$)] electrodes prepared by thermal decomposition method.**

| **Composition** | **Lattice parameter (Å)** | **Lattice parameter (Å) Literature** |
|---|---|---|
| $NiCo_2O_4$ | 8.1260 ±0.0004 | 8.105 [53] |
| $Ni_{0.95}Cu_{0.05}Co_2O_4$ | 8.1233 ± 0.0003 | 8.111 [53] |
| $Ni_{0.9}Cu_{0.1}Co_2O_4$ | 8.1240 ± 0.0003 | 8.112 [53] |
| $Ni_{0.75}Cu_{0.25}Co_2O_4$ | 8.1205 ± 0.0004 | 8.112 [53] |
| $Ni_{0.5}Cu_{0.5}Co_2O_4$ | 8.1202 ± 0.0004 | 8.110 [53] |
| $Ni_{0.25}Cu_{0.75}Co_2O_4$ | 8.1222 ± 0.0006 | 8.115 [53] |
| $Fe_{0.1}Cu_{0.9}Co_2O_4$ | 8.1012 ± 0.0004 | N/A |
| $Fe_{0.15}Cu_{0.35}Co_{2.5}O_4$ | 8.1001 ± 0.0002 | N/A |
| $Fe_{0.1}Ni_{0.9}Co_2O_4$ | 8.1245 ± 0.0003 | 8.111 [59] |
| $Fe_{0.15}Ni_{0.35}Co_{2.5}O_4$ | 8.1048 ± 0.0002 | N/A |

A graphic representation of nickel stoichiometry and the lattice parameter of the prepared films is also shown in Figure 3.8. We have compared lattice parameter values with those of two different studies. In our study the lattice parameters were found to be much closer to (JCPDS) data file [93].

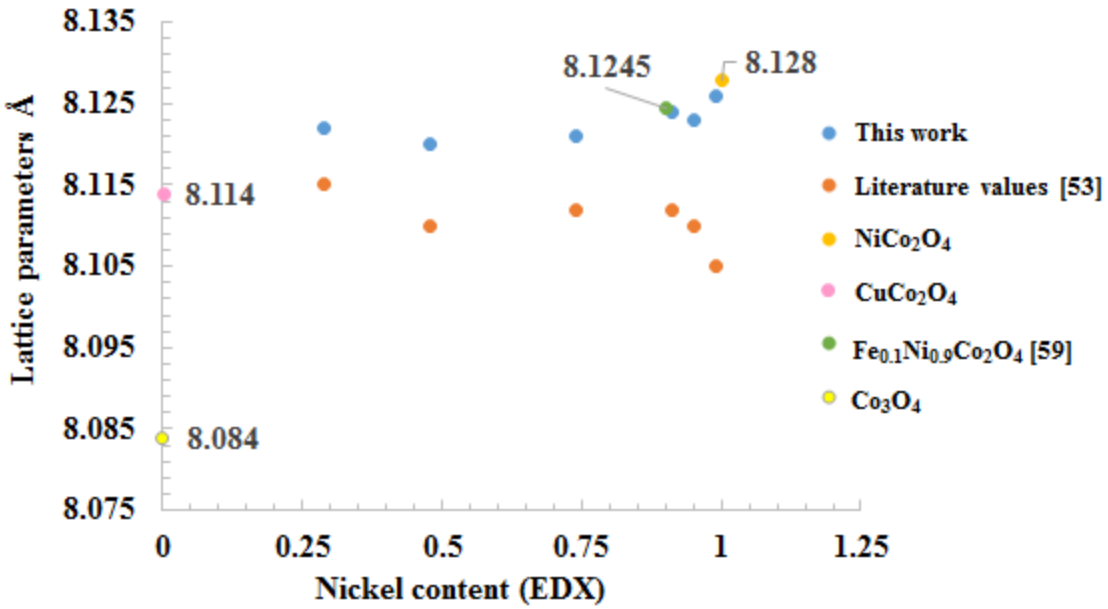


**Figure 3.8:** A graphic representation of nickel stoichiometry in $Ni_{1-x}Cu_xCo_2O_4$ and $Fe_yNi_{x-y}Co_{3-x}O_4$ as a function of the lattice parameter of the prepared film in this work and others' work.

## 3.5. Surface area and roughness factor characterization - CV

The surface area and roughness factor ($R_f$) can be characterized by cyclic voltammetry. The roughness of the electrodes, which a measure of the ratio of the material's real surface area to geometric area, allows the electrochemical results to be compared by considering the films roughness. The roughness factor is a dimensionless parameter which is useful for the study of a surface's topography. This parameter can be defined as the ratio between the real surface area of the topography and the geometrically projected area of the topography. Cyclic voltammetry has been used to determine the real surface area of all our $Ni_{1-x}Cu_xCo_2O_4$ electrodes by recording CV at different scan rates over a potential range where the current is mainly capacitive in nature (i.e., where the Faradaic current on the electrode is negligible). In this way, the measurement of the current will correspond only to the charge /discharge of the electrical double layer. The cyclic voltammograms shown in Figure 3.9 were recorded in 1M KOH solution at different scan rates (10 $mVs^{-1}$ to100 $mVs^{-1}$) for a narrow potential range, -100 mV to 100 mV (SCE). From the CV graph, we can obtain the current at the mid point (0 mV) to produce a plot of the charging current density vs voltage. A plot of charging current density was measured at the midpoint (0 mV) of the scan range. The line of regression for the graphs of charging current density was fitted to pass through the origin (0,0). Each electrode displayed good capacitive behaviour where the positive and negative charging current are very similar in magnitude as a function of sweep rates and a linear graph was obtained when the charging current density ($j_{cap}$) is plotted against the scan rate ($\delta E/ \delta t$) for the positive and negative current values, shown in Figure 3.10. Both positive and negative slopes were measured, and an average slope was calculated.

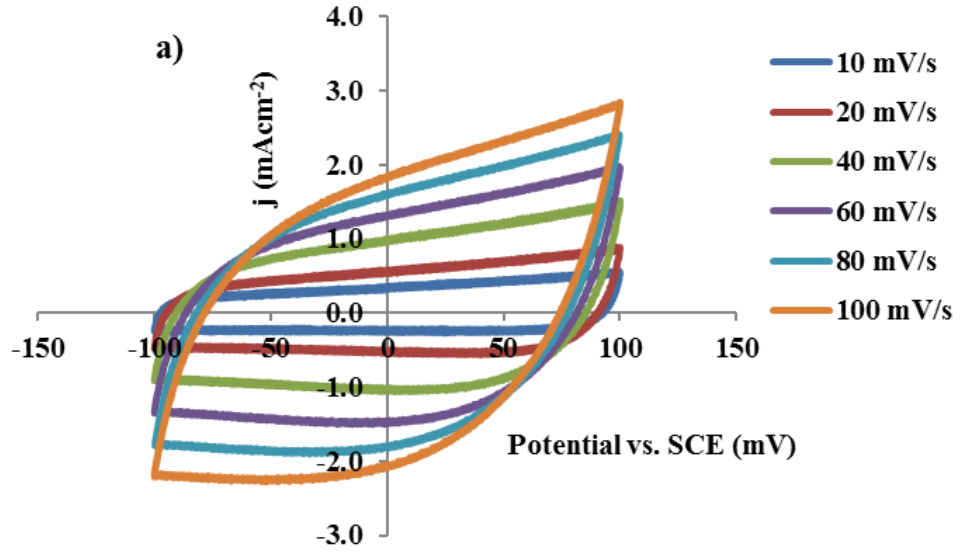
a)
j (mAcm-2)
4.0
3.0
2.0
1.0
0.0
-1.0
-2.0
-3.0
-150
-100
-50
0
50
100
150
Potential vs. SCE (mV)
10 mV/s
20 mV/s
40 mV/s
60 mV/s
80 mV/s
100 mV/s

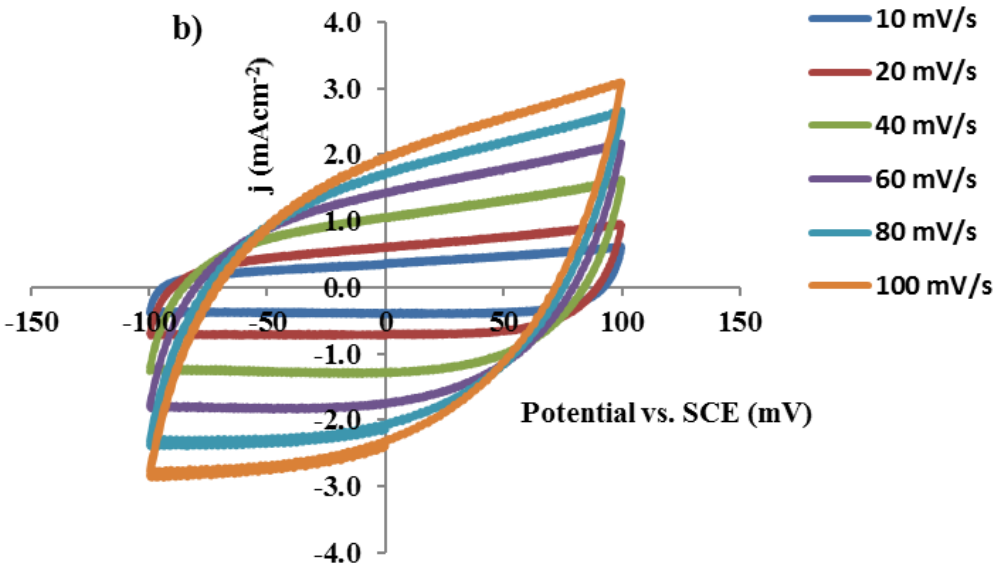
b)
j (mAcm-2)
4.0
3.0
2.0
1.0
0.0
-1.0
-2.0
-3.0
-4.0
-150
-100
-50
0
50
100
150
Potential vs. SCE (mV)
10 mV/s
20 mV/s
40 mV/s
60 mV/s
80 mV/s
100 mV/s

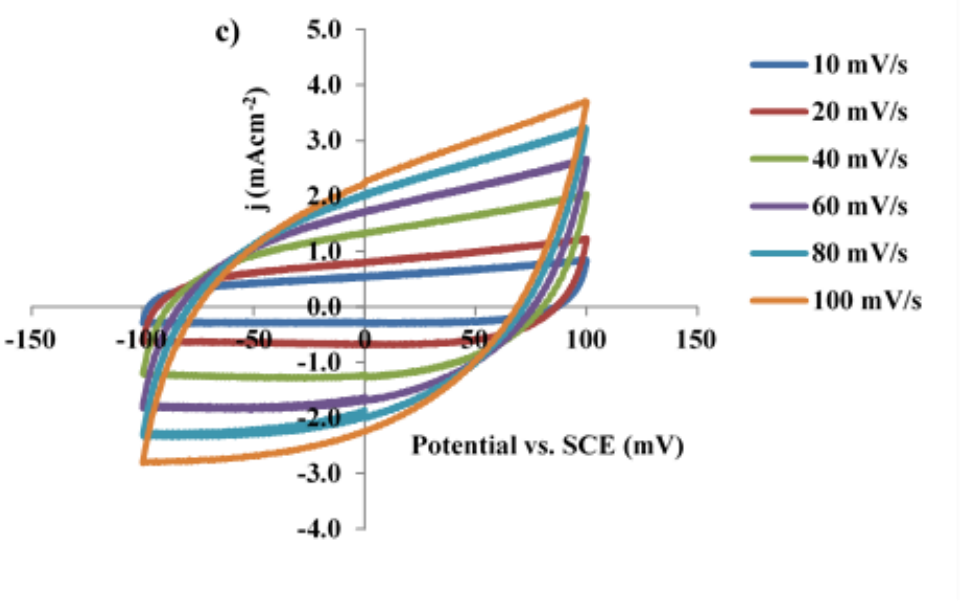
c)
5.0
4.0
3.0
2.0
1.0
0.0
-1.0
-2.0
-3.0
-4.0
j (mAcm-2)
-150
-100
-50
0
50
100
150
Potential vs. SCE (mV)
10 mV/s
20 mV/s
40 mV/s
60 mV/s
80 mV/s
100 mV/s

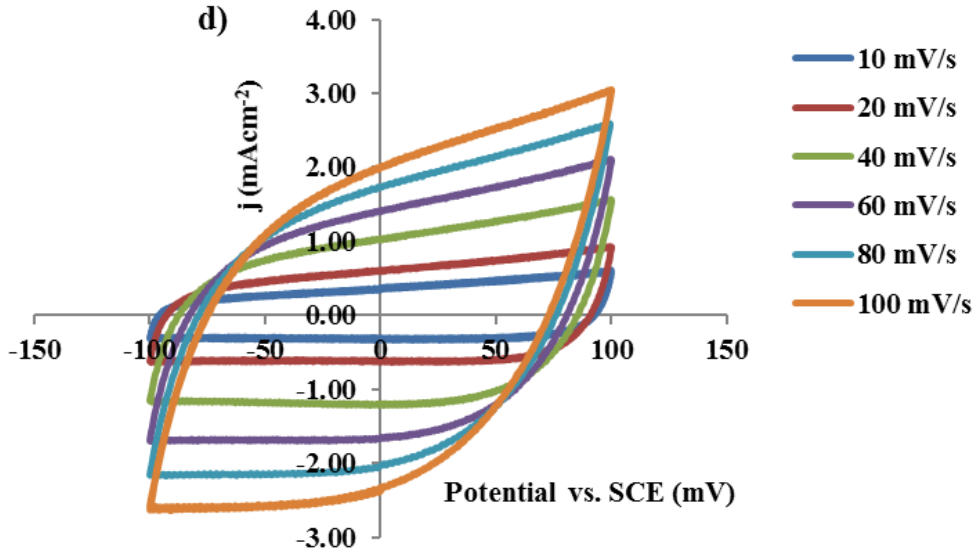
d)
4.00
3.00
2.00
1.00
0.00
-1.00
-2.00
-3.00
j (mAcm-2)
-150
-100
-50
0
50
100
150
Potential vs. SCE (mV)
10 mV/s
20 mV/s
40 mV/s
60 mV/s
80 mV/s
100 mV/s

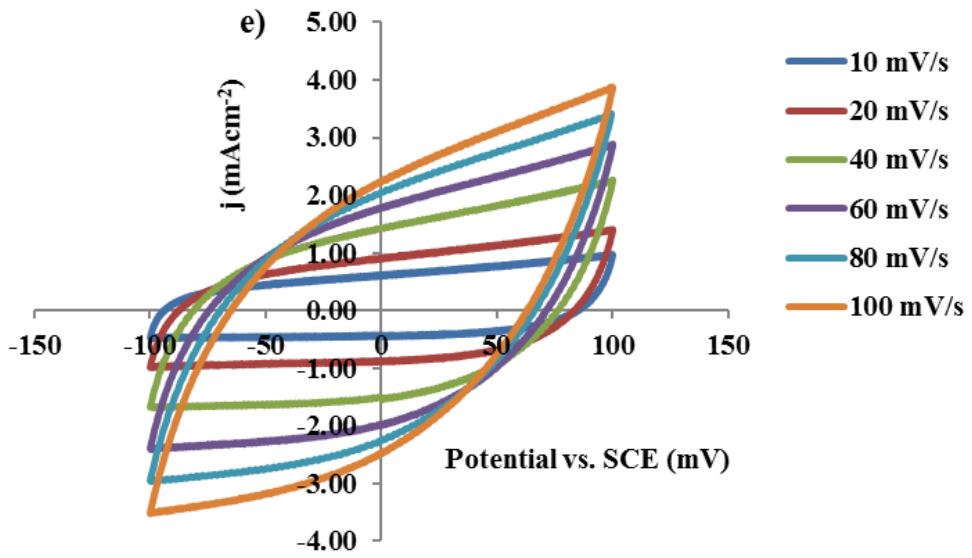
e)
5.00
4.00
3.00
2.00
1.00
0.00
-1.00
-2.00
-3.00
-4.00
j (mAcm-2)
-150
-100
-50
0
50
100
150
Potential vs. SCE (mV)
10 mV/s
20 mV/s
40 mV/s
60 mV/s
80 mV/s
100 mV/s

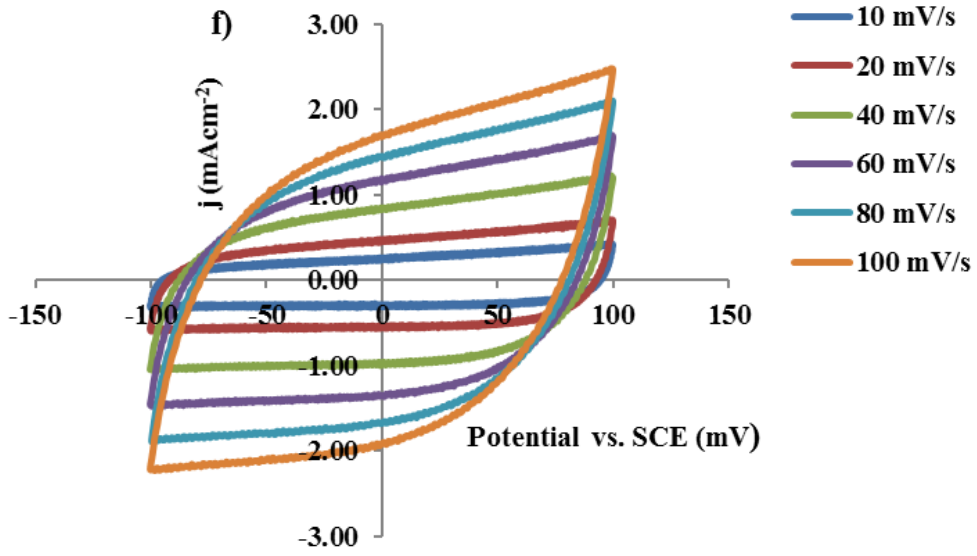
f)
3.00
2.00
1.00
0.00
-1.00
-2.00
-3.00
j (mAcm-2)
-150
-100
-50
0
50
100
150
Potential vs. SCE (mV)
10 mV/s
20 mV/s
40 mV/s
60 mV/s
80 mV/s
100 mV/s

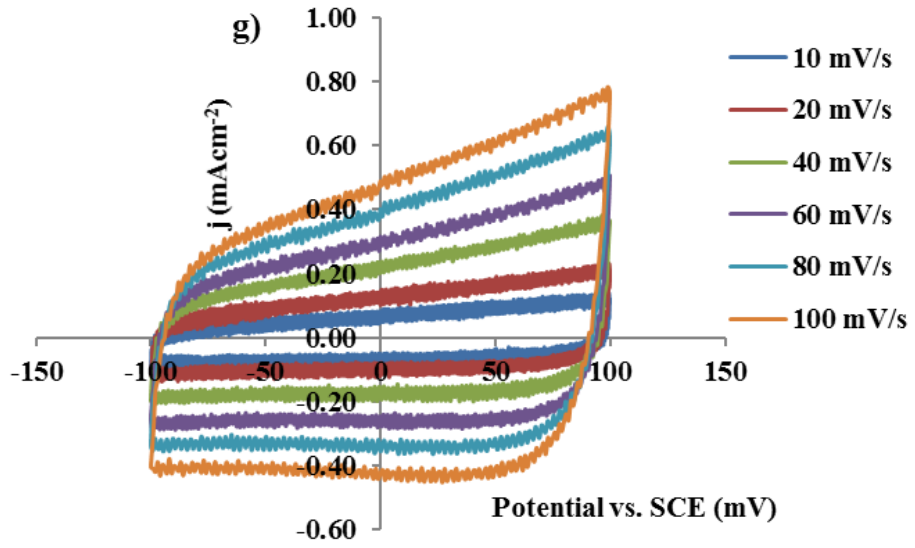
g)
1.00
0.80
0.60
0.40
0.20
0.00
-0.20
-0.40
-0.60
j (mAcm-2)
-150
-100
-50
0
50
100
150
Potential vs. SCE (mV)
10 mV/s
20 mV/s
40 mV/s
60 mV/s
80 mV/s
100 mV/s

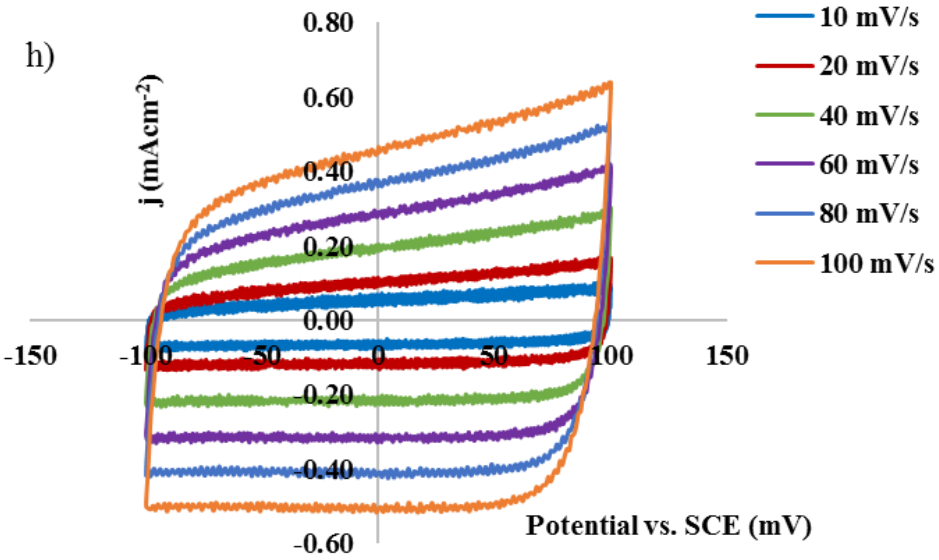
h)
0.80
0.60
0.40
0.20
0.00
-0.20
-0.40
-0.60
j (mAcm-2)
-150
-100
-50
0
50
100
150
Potential vs. SCE (mV)
10 mV/s
20 mV/s
40 mV/s
60 mV/s
80 mV/s
100 mV/s

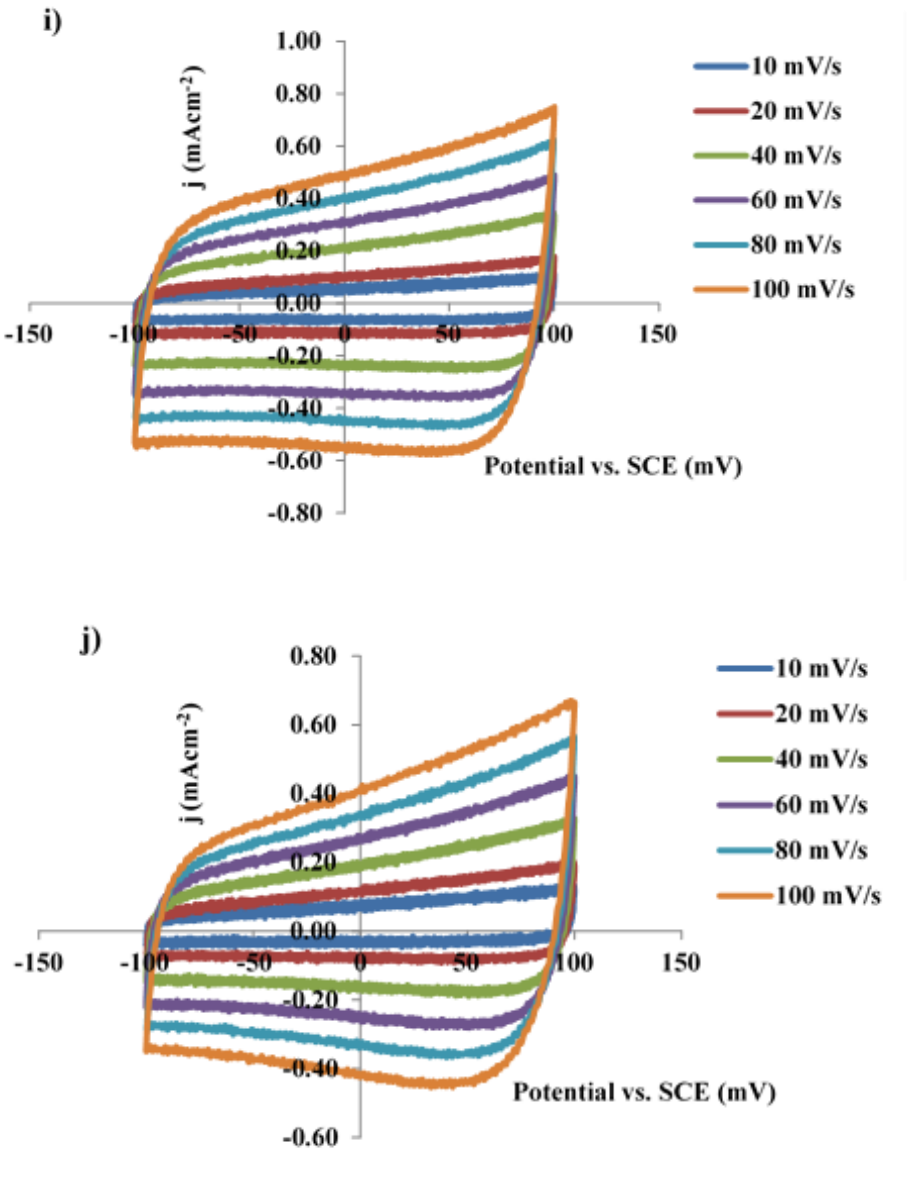


**Figure 3.9:** Cyclic voltammograms of the a) $NiCo_2O_4$, b) $Ni_{0.95}Cu_{0.05}Co_2O_4$, c) $Ni_{0.9}Cu_{0.1}Co_2O_4$, d) $Ni_{0.75}Cu_{0.25}Co_2O_4$, e) $Ni_{0.5}Cu_{0.5}Co_2O_4$ ($j_{cap}$ 0.03744 mA $cm^{-2}$ ± 0.00389), f) $Ni_{0.25}Cu_{0.75}Co_2O_4$ , g) $Fe_{0.1}Cu_{0.9}Co_2O_4$, and h) $Fe_{0.15}Cu_{0.35}Co_{2.5}O_4$ ($j_{cap}$ 0.00490 mA $cm^{-2}$ ± 0.00007), i) $Fe_{0.1}Ni_{0.9}Co_2O_4$, and j) $Fe_{0.15}Ni_{0.35}Co_{2.5}O_4$ , electrodes in 1M KOH for scans recorded in a potential range of -100 mV to 100 mV (SCE) at various sweep rates.

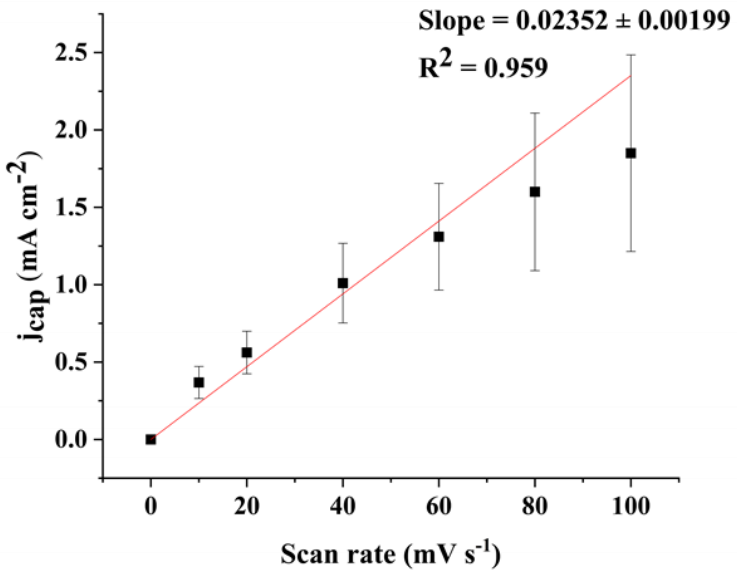
Slope = 0.02352 ± 0.00199
R2 = 0.959
jcap (mA cm-2)
Scan rate (mV s-1)
0.0
0.5
1.0
1.5
2.0
2.5
0
20
40
60
80
100

a)

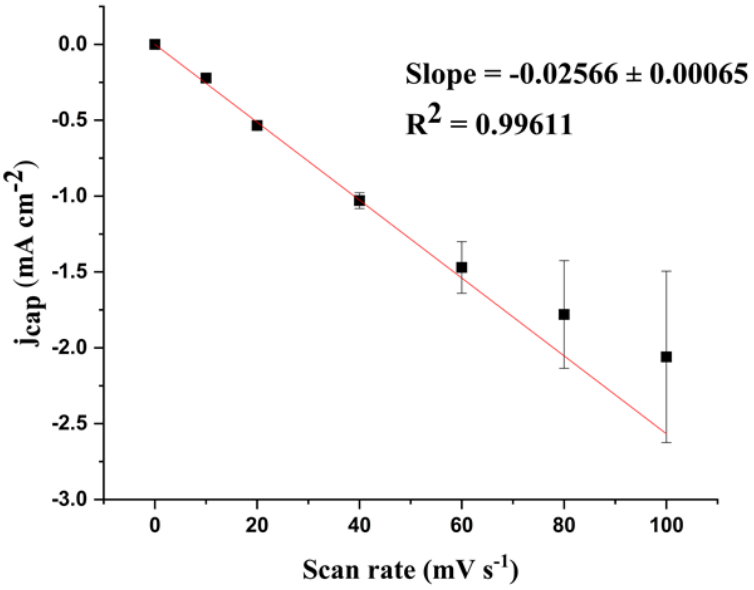
Slope = -0.02566 ± 0.00065
R2 = 0.99611
jcap (mA cm-2)
Scan rate (mV s-1)
0.0
-0.5
-1.0
-1.5
-2.0
-2.5
-3.0
0
20
40
60
80
100

b)

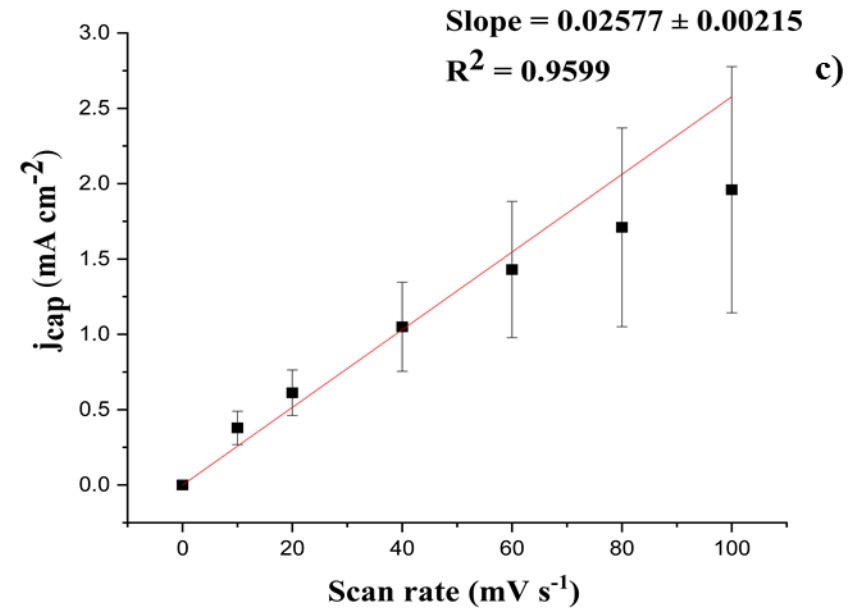
Slope = 0.02577 ± 0.00215
$R^2$ = 0.9599
c)
$j_{cap}$ (mA $cm^{-2}$)
Scan rate (mV $s^{-1}$)
3.0
2.5
2.0
1.5
1.0
0.5
0.0
0
20
40
60
80
100

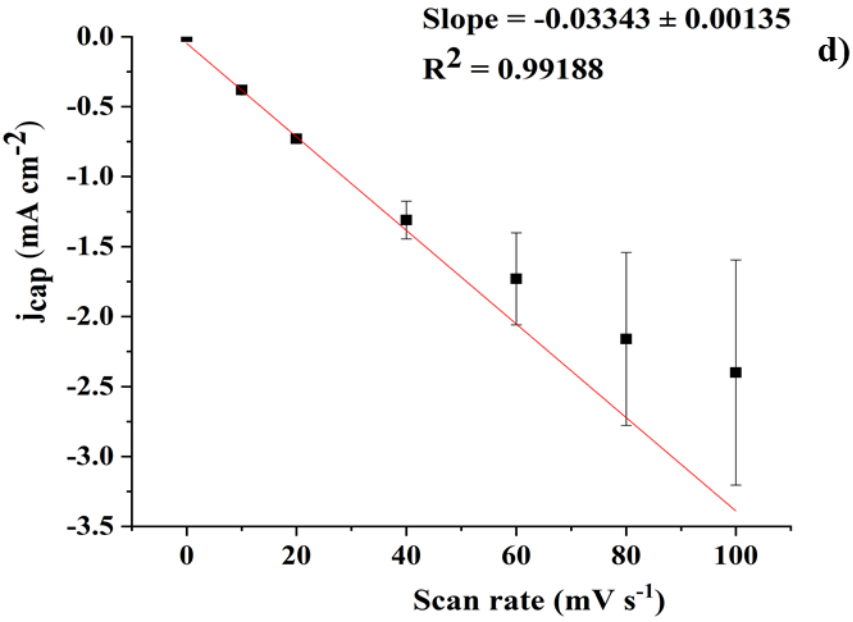
Slope = -0.03343 ± 0.00135
$R^2$ = 0.99188
d)
$j_{cap}$ (mA $cm^{-2}$)
Scan rate (mV $s^{-1}$)
0.0
-0.5
-1.0
-1.5
-2.0
-2.5
-3.0
-3.5
0
20
40
60
80
100

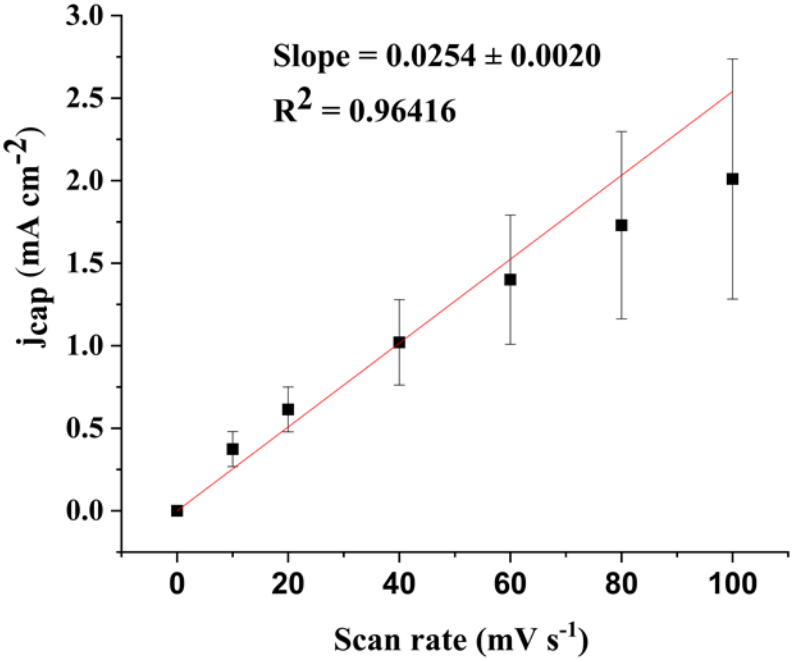
Slope = 0.0254 ± 0.0020
$R^2$ = 0.96416
jcap (mA cm$^{-2}$)
Scan rate (mV s$^{-1}$)
3.0
2.5
2.0
1.5
1.0
0.5
0.0
0
20
40
60
80
100

e)

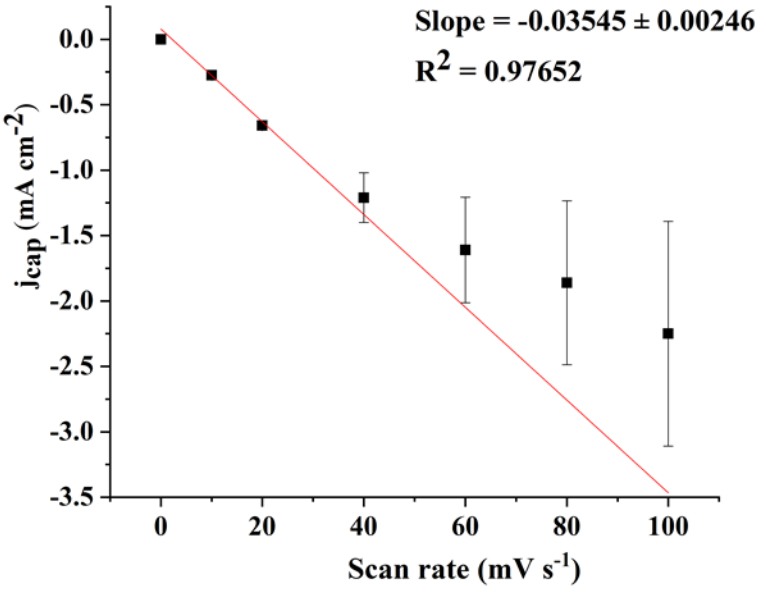
Slope = -0.03545 ± 0.00246
$R^2$ = 0.97652
jcap (mA cm$^{-2}$)
Scan rate (mV s$^{-1}$)
0.0
-0.5
-1.0
-1.5
-2.0
-2.5
-3.0
-3.5
0
20
40
60
80
100

f)

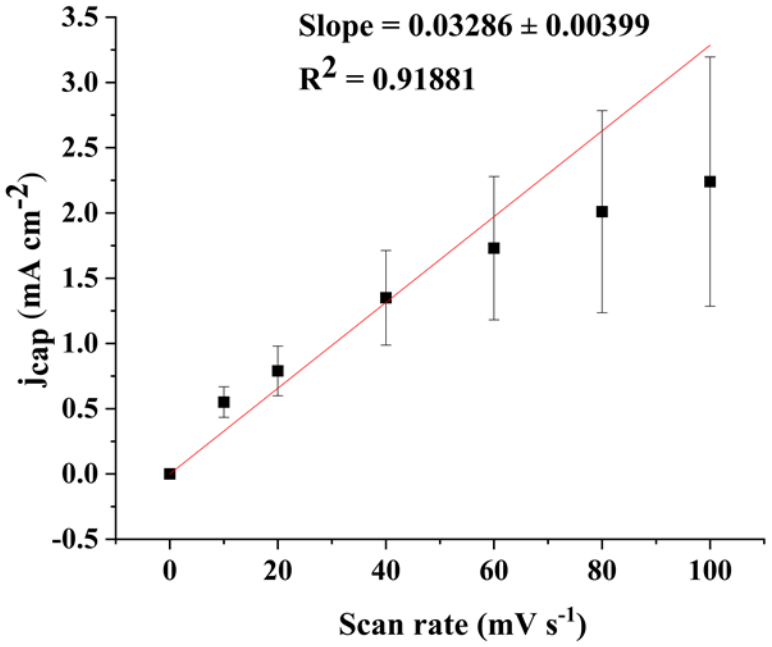
Slope = 0.03286 ± 0.00399
R2 = 0.91881
jcap (mA cm-2)
Scan rate (mV s-1)
3.5
3.0
2.5
2.0
1.5
1.0
0.5
0.0
-0.5
0
20
40
60
80
100

g)

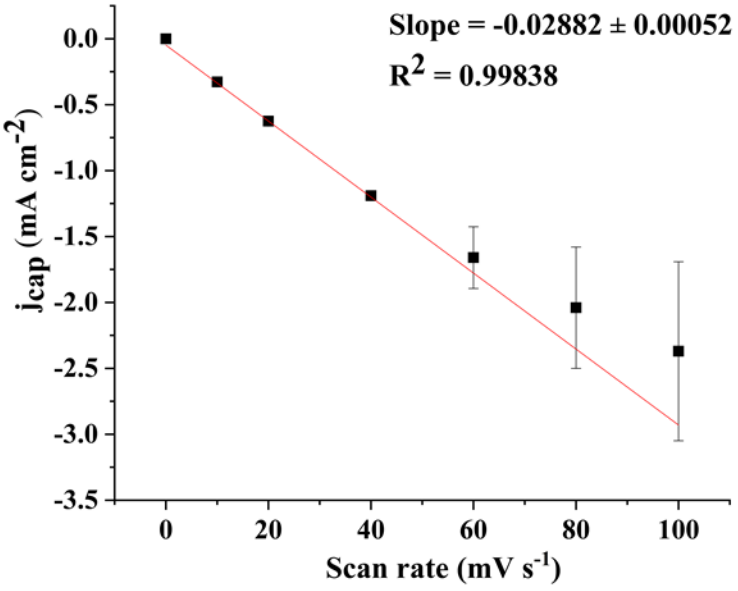
Slope = -0.02882 ± 0.00052
R2 = 0.99838
jcap (mA cm-2)
Scan rate (mV s-1)
0.0
-0.5
-1.0
-1.5
-2.0
-2.5
-3.0
-3.5
0
20
40
60
80
100

h)

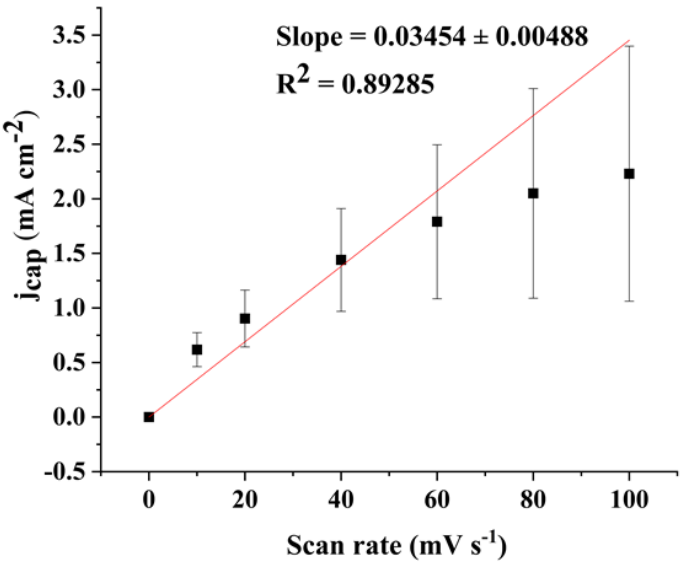
Slope = 0.03454 ± 0.00488
$R^2$ = 0.89285
jcap (mA cm$^{-2}$)
Scan rate (mV s$^{-1}$)
3.5
3.0
2.5
2.0
1.5
1.0
0.5
0.0
-0.5
0
20
40
60
80
100

i)

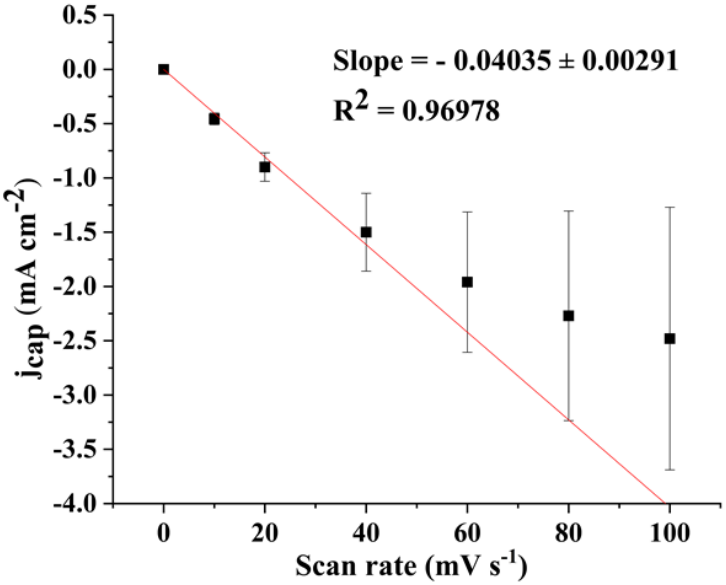
Slope = - 0.04035 ± 0.00291
$R^2$ = 0.96978
jcap (mA cm$^{-2}$)
Scan rate (mV s$^{-1}$)
0.5
0.0
-0.5
-1.0
-1.5
-2.0
-2.5
-3.0
-3.5
-4.0
0
20
40
60
80
100

j)

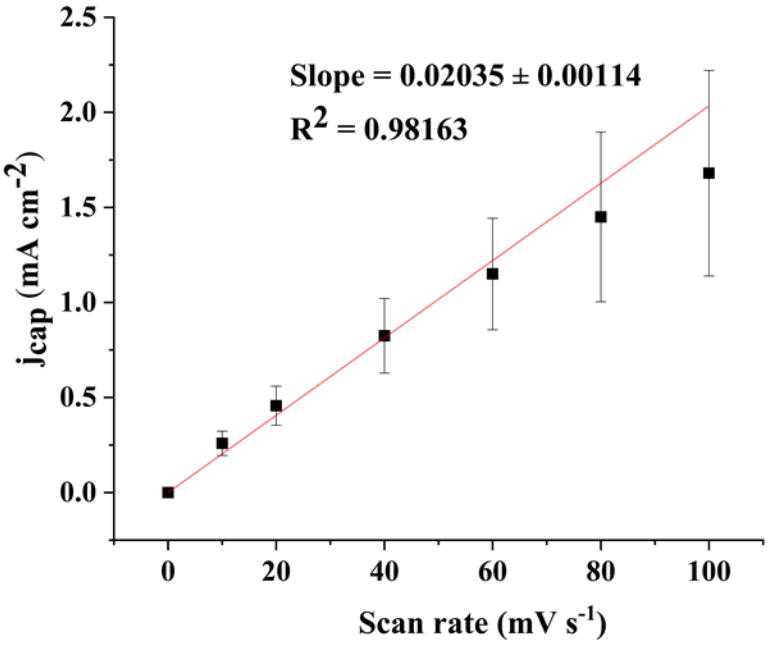
Slope = 0.02035 ± 0.00114
$R^2$ = 0.98163
jcap (mA cm$^{-2}$)
Scan rate (mV s$^{-1}$)
2.5
2.0
1.5
1.0
0.5
0.0
0
20
40
60
80
100

k)

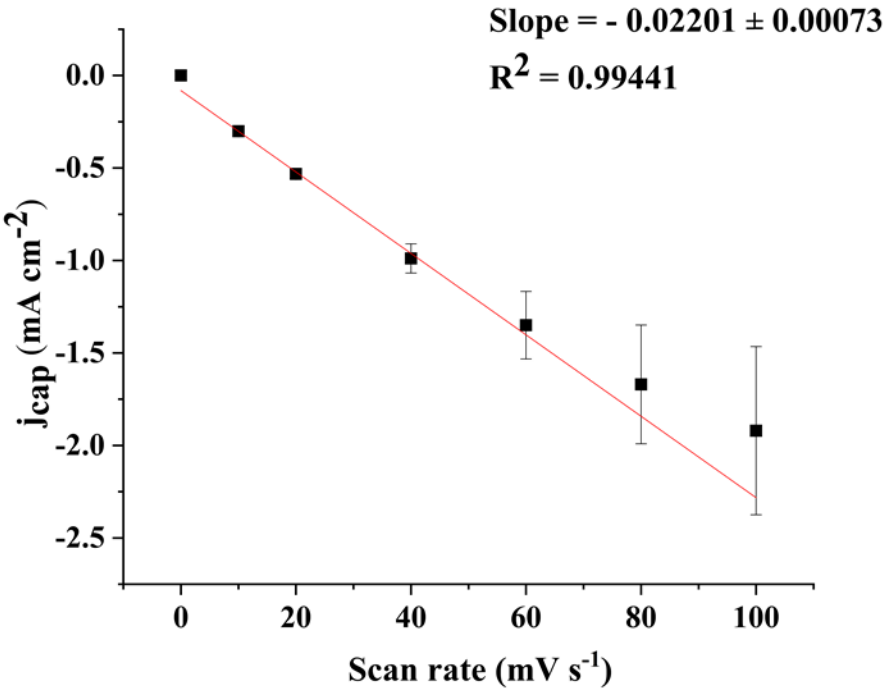
Slope = - 0.02201 ± 0.00073
$R^2$ = 0.99441
jcap (mA cm$^{-2}$)
Scan rate (mV s$^{-1}$)
0.0
-0.5
-1.0
-1.5
-2.0
-2.5
0
20
40
60
80
100

l)

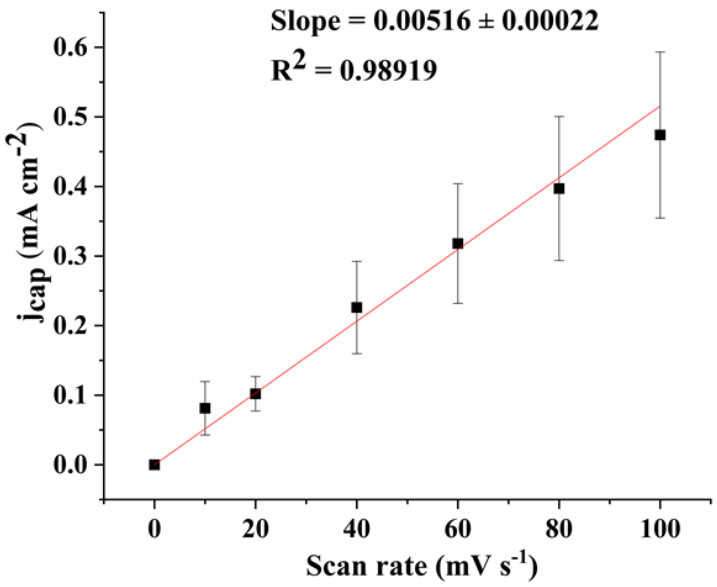
Slope = 0.00516 ± 0.00022
$R^2$ = 0.98919
$j_{cap}$ (mA cm$^{-2}$)
Scan rate (mV s$^{-1}$)
0.0
0.1
0.2
0.3
0.4
0.5
0.6
0
20
40
60
80
100

m)

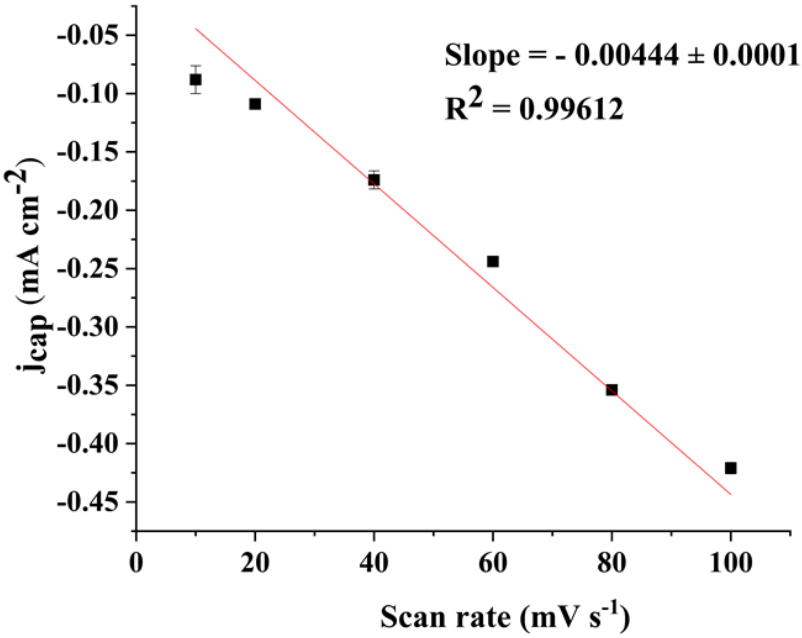
Slope = - 0.00444 ± 0.00012
$R^2$ = 0.99612
$j_{cap}$ (mA cm$^{-2}$)
Scan rate (mV s$^{-1}$)
-0.05
-0.10
-0.15
-0.20
-0.25
-0.30
-0.35
-0.40
-0.45
0
20
40
60
80
100

n)

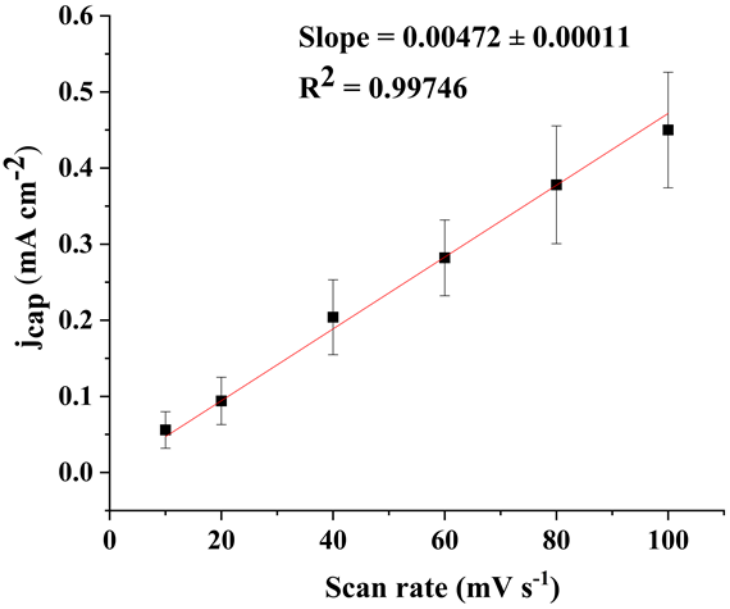
Slope = 0.00472 ± 0.00011
R2 = 0.99746
jcap (mA cm-2)
Scan rate (mV s-1)
0.6
0.5
0.4
0.3
0.2
0.1
0.0
0
20
40
60
80
100

o)

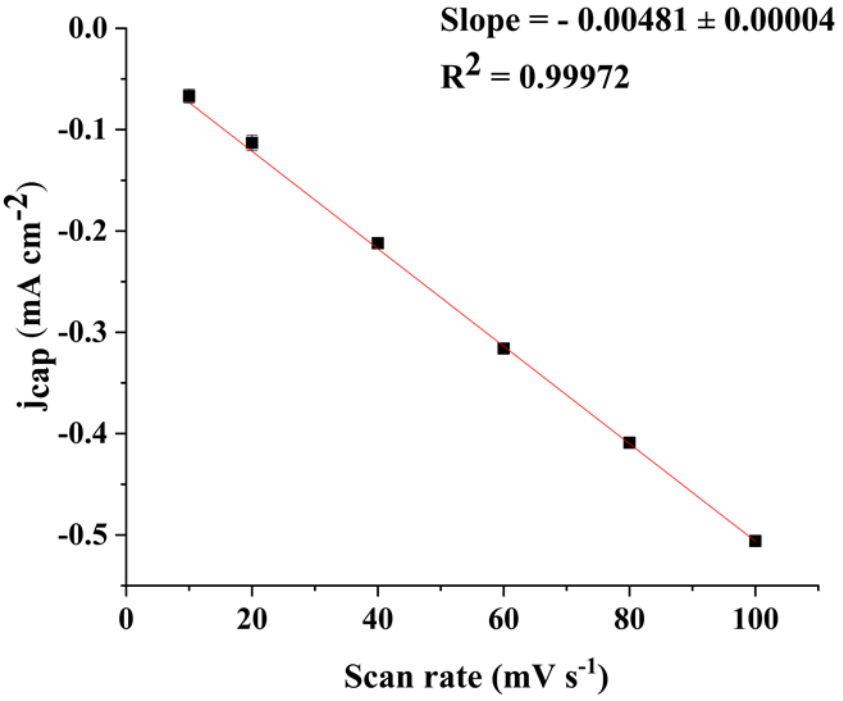
Slope = - 0.00481 ± 0.00004
R2 = 0.99972
jcap (mA cm-2)
Scan rate (mV s-1)
0.0
-0.1
-0.2
-0.3
-0.4
-0.5
0
20
40
60
80
100

p)

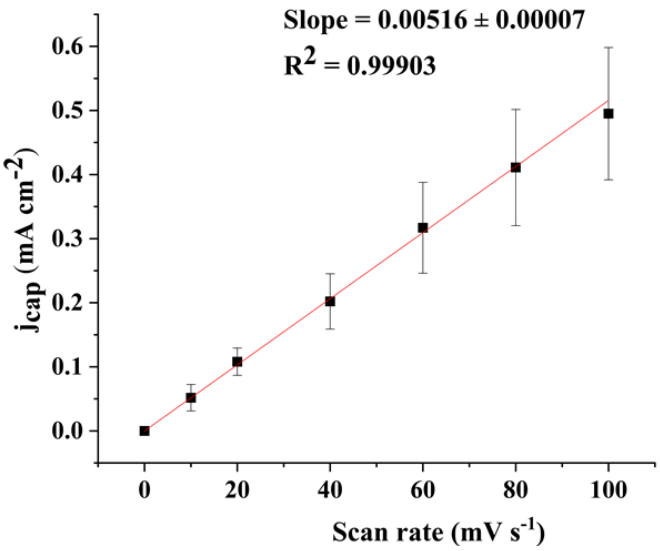
Slope = 0.00516 ± 0.00007
R2 = 0.99903
jcap (mA cm-2)
Scan rate (mV s-1)
0.0
0.1
0.2
0.3
0.4
0.5
0.6
0
20
40
60
80
100

q)

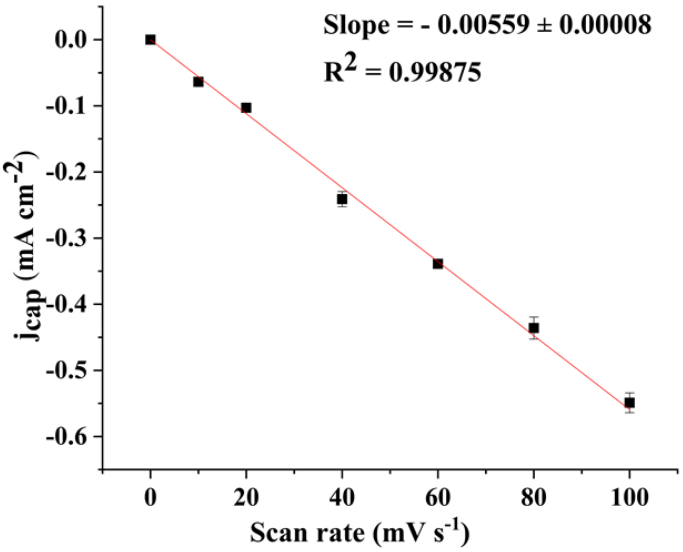
Slope = - 0.00559 ± 0.00008
R2 = 0.99875
jcap (mA cm-2)
Scan rate (mV s-1)
0.0
-0.1
-0.2
-0.3
-0.4
-0.5
-0.6
0
20
40
60
80
100

r)

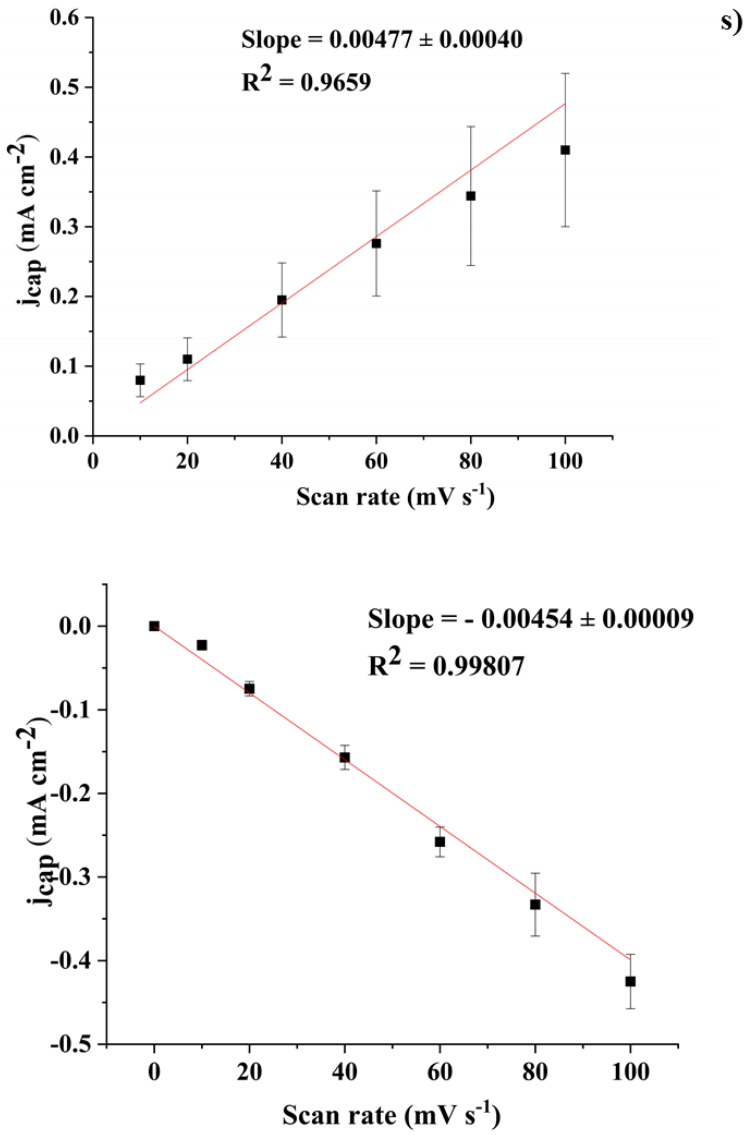


**Figure 3.10:** Plot of double layer charging current density vs. scan rate for the a) and b) $NiCo_2O_4$, c) and d) $Ni_{0.95}Cu_{0.05}Co_2O_4$, e) and f) $Ni_{0.9}Cu_{0.1}Co_2O_4$, g) and h) $Ni_{0.75}Cu_{0.25}Co_2O_4$, i) and j) $Ni_{0.5}Cu_{0.5}Co_2O_4$, k) and l) $Ni_{0.25}Cu_{0.75}Co_2O_4$, m) and n) $Fe_{0.1}Cu_{0.9}Co_2O_4$, o) and p) $Fe_{0.15}Cu_{0.35}Co_{2.5}O_4$ , q) and r) $Fe_{0.1}Ni_{0.9}Co_2O_4$, s) and t) $Fe_{0.15}Ni_{0.35}Co_{2.5}O_4$ , electrodes.

**Table 3.3:** Roughness factor of Ni-Cu, Fe-Cu and Fe-Ni spinel oxide prepared by thermal decomposition method.

| Composition | Total film loading ($g\ cm^{-2}$) ± 0.00010 | Roughness factor ($R_f$) |
|---|---|---|
| $NiCo_2O_4$ | 0.00063 | 410 ± 41 |
| $Ni_{0.95}Cu_{0.05}Co_2O_4$ | 0. 00064 | 493 ± 51 |
| $Ni_{0.9}Cu_{0.1}Co_2O_4$ | 0. 00078 | 507 ± 53 |
| $Ni_{0.75}Cu_{0.25}Co_2O_4$ | 0. 00071 | 514 ± 52 |
| $Ni_{0.5}Cu_{0.5}Co_2O_4$ | 0. 00051 | 624 ± 64 |
| $Ni_{0.25}Cu_{0.75}Co_2O_4$ | 0. 00082 | 353 ± 35 |
| $Fe_{0.1}Cu_{0.9}Co_2O_4$ | 0. 00041 | 80 ± 14 |
| $Fe_{0.15}Cu_{0.35}Co_{2.5}O_4$ | 0. 00030 | 82 ± 12 |
| $Fe_{0.1}Ni_{0.9}Co_2O_4$ | 0. 00031 | 90 ± 12 |
| $Fe_{0.15}Ni_{0.35}Co_{2.5}O_4$ | 0. 00040 | 78 ± 9 |
| $CuCo_2O_4$ | 0. 00051 | 181 ± 24 |
| $Co_3O_4$ | 0. 00071 | 112 ± 11 |

The double layer capacitance ($C_{dl}$) values were calculated) from the slope ($C_{dl} = i_{cap}/ (\delta E/ \delta t)$. The roughness factor was calculated from the ratio of ($C_{dl}$) of the sample and that of a smooth surface (i.e. 60 μF $cm^{-2}$). The roughness factor for each sample was summarized in Table 3.3. Our data shows that copper containing nickel samples have higher roughness factors whereas copper containing iron samples have lower roughness factors. High roughness factor means the material possesses a larger surface area and may lead to larger number of active sites being available for the catalytic process. The relative errors were in the range of 11 to 22%, they arise from the

calculated absolute error from the geometric area and the real smooth surface area of the standard which is mercury see section (2.2.4.2) in Chapter 2.

## 3.6. Conclusion

Our characterization methods have confirmed that we successfully prepared spinel oxide electrodes. The SEM experiments suggest that an increase in copper content in $NiCo_2O_4$ leads to a porous surface as well as formation of grains. The EDX spectra provided elemental compositions and allowed us to show a good correlation between stoichiometric and EDX elemental composition for our prepared samples. While all samples exhibit spinel structure $Fe_{0.1}Cu_{0.9}Co_2O_4$, and $Fe_{0.1}Ni_{0.9}Co_2O_4$ samples showed small amounts of an extra phase along with the spinel structure. The cyclic voltammogram of samples were obtained to produce the graph of charging current density as a function of sweep rate, which gives through a linear regression the surface roughness factor. We have determined that the $Ni_{1-x}Cu_xCo_2O_4$ ($0 \leq x \leq 0.75$) electrodes have higher roughness factors than $Fe_yCu_{x-y}Co_{3-x}O_4$ and $Fe_yNi_{x-y}Co_{3-x}O_4$, ($0.15 \leq x \leq 1.0$) electrodes.

# Chapter 4 - Electrocatalytic Behaviour- Results and Discussion

## 4.1 Introduction

Spinel oxide electrodes are catalysts that participate in electrochemical reactions by increasing the rate of the chemical reaction. Our aim is to prepare ternary spinel oxide electrocatalysts for water electrolysis leading to oxygen evolution reaction, which is highly sensitive to the nature and structure of the electrode surface [53]. Our prepared spinel oxide electrodes activities are tested using a well understood electrochemical process namely the oxygen evolution reaction. In a water electrolyser, decreasing the overpotential for oxygen evolution is key in reducing the cost of hydrogen production. In this chapter, the results of the electrocatalytic activity of our prepared samples will be discussed.

## 4.2. Identification of Electrochemical process at potential negative to oxygen evolution.

The effect of composition (1M KOH solution) on the voltammetric behaviour of $NiCo_2O_2$, $Ni_{0.95}Cu_{0.05}Co_2O_4$, $Ni_{0.9}Cu_{0.1}Co_2O_4$, $Ni_{0.75}Cu_{0.25}Co_2O_4$, $Ni_{0.5}Cu_{0.5}Co_2O_4$, $Ni_{0.25}Cu_{0.75}Co_2O_4$, and $Fe_{0.1}Cu_{0.9}Co_2O_4$, $Fe_{0.15}Cu_{0.35}Co_{2.5}O_4$, $Fe_{0.1}Ni_{0.9}Co_2O_4$, $Fe_{0.15}Ni_{0.35}Co_{2.5}O_4$ at a potential range of -100 mV to 500 mV with a scan rate of 10 mV $s^{-1}$, was clearly seen in Figure 4.1 (a) and Figure 4.1(b), respectively.

The CV display characteristic regions within the range of (-100 mV to 500 mV). The double layer region can be observed between -100 mV and 100 mV. The region between 300 mV and 400 mV display some redox reactions and around 500 mV the onset of oxygen evolution reaction is observed. When the potential is swept, a capacitive current exists, the magnitude of this current can be evaluated in the double layer region. A Faradaic current is introduced when a redox reaction take place at working electrode. Figure 4.1(a) and Figure 4.1(b) represent a cyclic voltammograms of redox process in the potential range of -100 mV to 500 mV for all our prepared samples. In Figure 4.1(a) the highest copper containing $Ni_{0.29}Cu_{0.55}Co_{2.3}O_4$ electrode shows the lowest redox peak current density (0.0037 $mAcm^{-2}$) among all other electrodes. Similarly, in Figure 4.1(b). The highest copper containing $Fe_{0.22}Cu_{0.41}Co_{2.35}O_4$ electrode exhibits the lowest redox peak current density (0.0045 $mAcm^{-2}$) among all other electrodes.

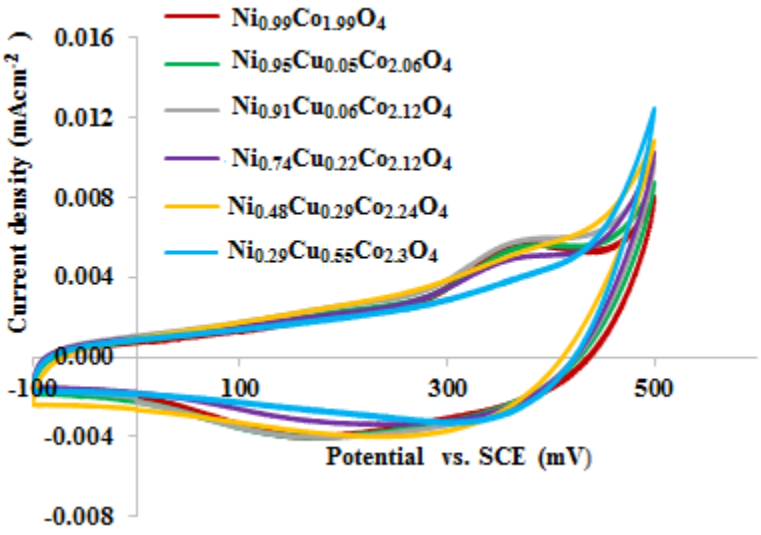


**Figure 4.1 (a):** Cyclic Voltammetry of $NiCo_2O_4$, $Ni_{0.95}Cu_{0.05}Co_2O_4$, $Ni_{0.9}Cu_{0.1}Co_2O_4$, $Ni_{0.75}Cu_{0.25}Co_2O_4$, $Ni_{0.5}Cu_{0.5}Co_2O_4$, $Ni_{0.25}Cu_{0.75}Co_2O_4$ electrodes in the potential region of -100 mV to 500 mV at a Scan rate of 10 $mVs^{-1}$ in 1M KOH solution.

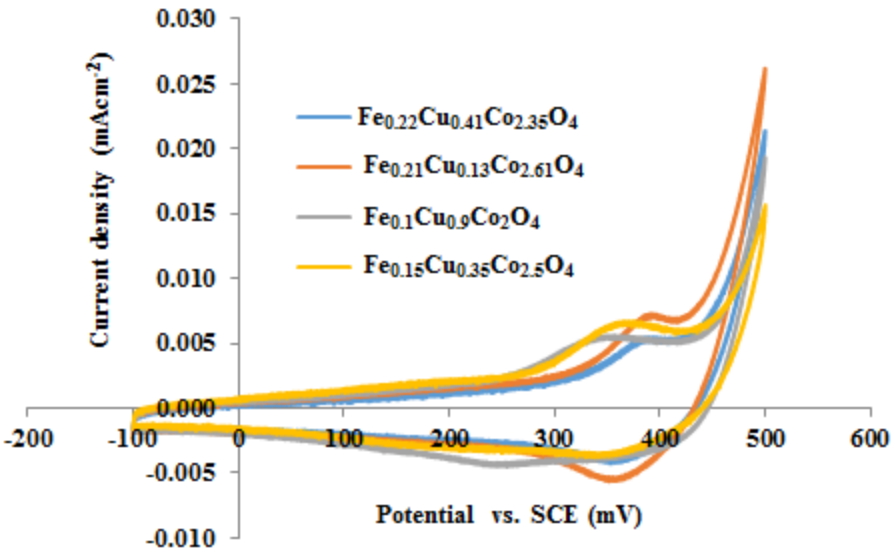


**Figure 4.1 (b):** Cyclic Voltammetry of $Fe_{0.1}Cu_{0.9}Co_2O_4$, $Fe_{0.15}Cu_{0.35}Co_{2.5}O_4$, $Fe_{0.1}Ni_{0.9}Co_2O_4$, and $Fe_{0.15}Ni_{0.35}Co_{2.5}O_4$ electrodes in the potential region of -100 mV to 500 mV at a Scan rate of 10 $mVs^{-1}$ in 1M KOH solution.

A clear understanding of the properties of these materials is still lacking and an increase in their performance could be due to several factors such as an increase in the number of active sites, higher conductivity of the films or creating chemically/structurally new active sites on the surface of the material. Overall, the cyclic voltammogram display a characteristic current response as a function of applied potential. At a positive potential region, each voltammogram exhibits a positive charging current and a corresponding negative charging current. The characteristic redox couples are assigned to Co (III) to Co (IV) and Ni (II) to Ni (III) surface processes according to the following reaction [94, 12].

$$Co^{3+}OOH + OH^- \rightleftharpoons Co^{4+}O_2 + H_2O + e \qquad (17)$$

$$Ni^{2+}(OH)_2 + OH^- \rightleftharpoons Ni^{3+}OOH + H_2O + e \qquad (18)$$

The assignment of this redox pair is still controversial because the redox potential of $Ni^{3+}/Ni^{2+}$ and $Co^{4+}/Co^{3+}$ are very close. [53]. Ding *et al.* obtained similar voltammograms for $NiCo_2O_4$ as our study. Ding *et al.* assigned these peaks to the overall contribution of $Ni^{3+}/Ni^{2+}$ and $Co^{3+}/Co^{2+}$ [95]. Qian *et al.* assigned these peaks to $Co^{2+}$ / $Co^{3+}$ and $Ni^{2+}$ / $Ni^{3+}$ and proposed that peaks are not separated [96]. Nikolov *et al.* also stated that the anodic peak may be due to the presence of $Co^{3+}$ / $Co^{4+}$ and $Ni^{3+}$ / $Ni^{4+}$ [41]. In our study, the $NiCo_2O_4$ electrode produced the lowest redox potential. As the amount of copper content increased in the sample electrode, the redox peaks were shifted to a more positive potential. Current density also decreased with the addition of copper. This indicates that the substitution of nickel with copper affects the redox potential as well as current density.

## 4.3 Electrocatalytic behaviour results

### 4.3.1 $Ni_{1-x}Cu_xCo_2O_4$ ($0 \leq x \leq 0.75$)

Cyclic voltammograms of $Ni_{1-x}Cu_xCo_2O_4$ electrodes were obtained for oxygen evolution reaction. The cyclic voltammograms of $Ni_{1-x}Cu_xCo_2O_4$ electrodes for the oxygen evolution reaction were recorded between -100 mV to 1000 mV with a scan rate of 50 m $Vs^{-1}$ and the data is shown in Figure 4.2. The slope (Figure 4.3) is highest for the electrode with the highest copper content ($Ni_{0.29}Cu_{0.55}Co_{2.3}O_4$) and lowest for the electrode with the lowest copper content ($Ni_{0.95}Cu_{0.05}Co_{2.06}O_4$). Figure 4.2 shows that the higher copper containing $Ni_{0.29}Cu_{0.55}Co_2O_4$ compound enhances catalytic activity, further investigations of the site occupancy and surface composition of our materials is necessary to explain this behaviour.

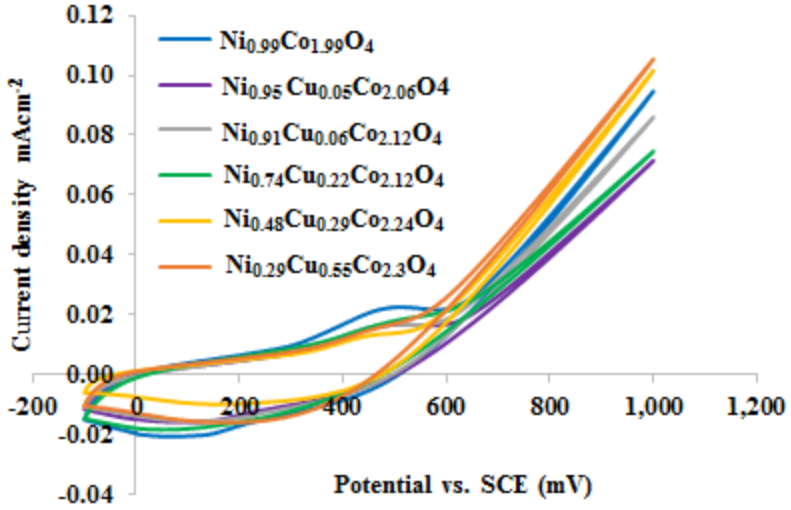


**Figure 4.2:** Cyclic voltammograms of $Ni_{1-x}Cu_xCo_2O_4$ corrected for the real surface area of the electrode using the roughness factor reported in Table 3.2, scan recorded in a potential range of -100 mV to 1000 mV.

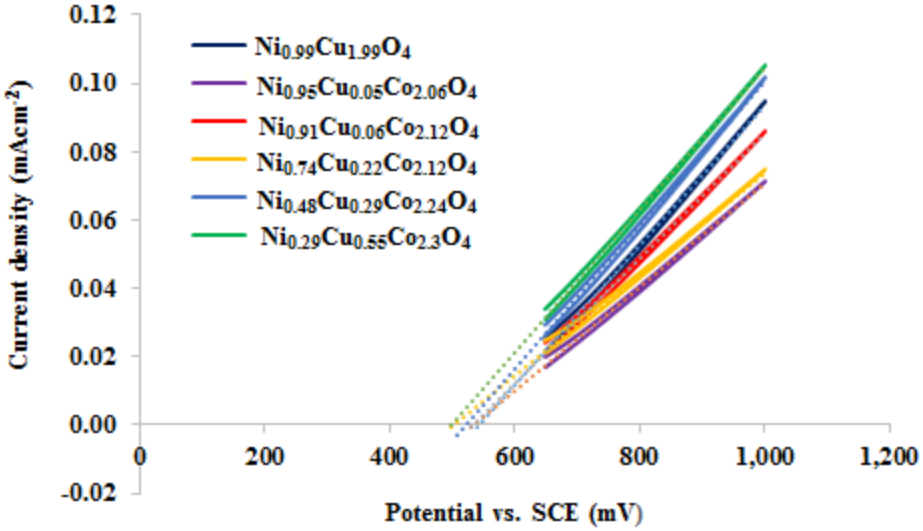


**Figure 4.3**: Single scan cyclic voltammograms of $Ni_{1-x}Cu_xCo_2O_4$ electrode showing the oxygen evolution reaction in a potential range of -100 mV to 1000 mV, corrected for their real surface area using the roughness factor.

### 4.3.2. $Fe_y$ Cu/ $Ni_{x-y}Co_{3-x}$ $O_4$ ($0 \leq x \leq 1$), ($0 \leq y \leq 0.15$), electrodes

Electrocatalytic activity for oxygen evolution reactions was carried out through cyclic voltammetry. In Figure 4.4 is the CV of $Fe_y$ Cu/ $Ni_{x-y}Co_{3-x}O_4$ ($0 \leq x \leq 1$), ($0 \leq y \leq 0.15$) electrode obtained from -100 mV to 1000 mV showing the region of the oxygen evolution reaction. The slope and current density are highest for the electrode with the highest copper content ($Fe_{0.1}Cu_{0.9}Co_2O_4$) shown in Figure 4.5.

A possible explanation for the current density enhancement in iron-containing samples may be attributed to iron's participation as an active site for the oxygen evolution reaction. According to Ting *et al.* the introduction of $Fe^{+3}$ increased the $Co^{+2}/Co^{+3}$ ratio in the octahedral sites, as shown below [59]:

$$\underset{A}{\underline{Co_x^{+2}\ Co_{1-x}^{+3}}}\ [\underset{B}{\underline{Co_x^{+3}\ Ni_{1-x}^{+2}\ Ni_x^{+3}}}]\ O_4\ (0 \leq x \leq 1),$$

where A and B refer to tetrahedral and octahedral sites, respectively. In reference to the description above, Xiao *et al.* concluded from their experiment that the active sites for the OER are related to the amount of $Co_x^{+2}$ ions [97]. In our copper containing iron samples, the highest current density (0.45 mA at 900 mV) are exhibited.

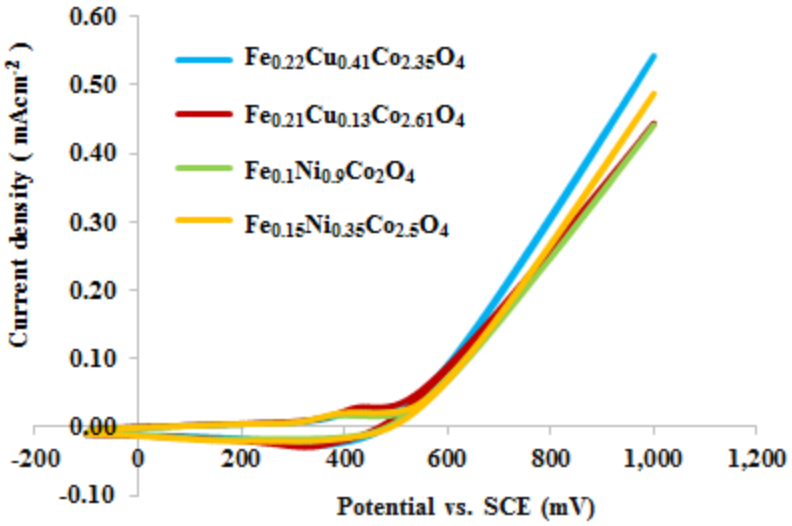


**Figure 4.4:** Cyclic voltammograms (true catalytic activity) of Fe-(Cu/Ni)-Co spinel oxide prepared by the thermal decomposition method, scan recorded in a potential range of -100 mV to 1000 mV.

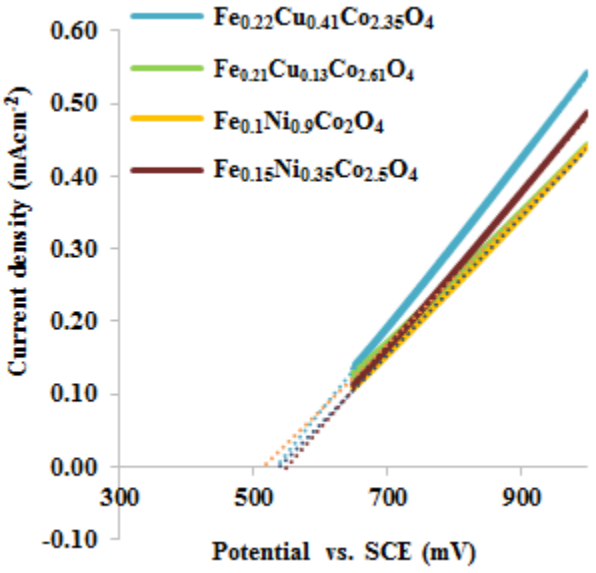


**Figure 4.5:** Single scan cyclic voltammograms of electrode Fe-(Cu/Ni)-Co showing the oxygen evolution reaction in a potential range of -100 mV to 1000 mV, corrected for their real surface area using the roughness factor.

Another possible reason for current density enhancement in iron-containing samples is due to nickel and copper's high electrical conductivity. In mixed oxidation states, the cations distribution in the octahedral site is responsible for the electrocatalytic activity. An increase in their performance properties could be due to the higher electrical conductivity of copper and nickel which facilitates an oxygen evolution reaction and enhances electrocatalytic activity [51, 98]. According to Marsan *et al*. and Fierro *et al.,* copper-cobalt spinel oxides exhibit a low crystalized single phase with partially inverted spinel structures along with a minor segregation of an extra CuO phase dependent on the Cu/Co ratio [99, 100]. Our existing work also mentions that the CuO phase is exhibited at a higher copper content (Cu =1). These results agree with the observation of our recent work in which the CuO extra phase is exhibited in the $Fe_{0.1}Cu_{0.9}Co_2O_4$ sample when the copper content is higher (Cu = 0.9). According to Guene *et al*. the conductivity increases with the increase of nickel content ($0 \leq x \leq 1$) [92].

The cyclic voltammograms of $Ni_{1-x}Cu_xCo_2O_4$ ($0 \leq x \leq 0.75$), $Fe_yCu/Ni_{x-y}Co_{3-x}O_4$ ($0 \leq x \leq 1$), ($0 \leq y \leq 0.15$), electrodes for the oxygen evolution reaction were recorded at a potential range of -100 mV to 1000 mV with a scan rate of 50 $mVs^{-1}$. Onset potential value was extrapolated from the linear slope of CV. Also, overpotential values were calculated by subtracting 159 mV vs. SCE from the onset potential. The onset potential and overpotential of all prepared electrodes for oxygen evolution reactions are summarized in Table 4.1. As the copper content increased in the nickel-cobalt spinel oxide, the overpotential decreased and $Ni_{0.5}Cu_{0.5}Co_2O_4$ achieved the lowest overpotential of 328 mV and the highest current density of 0.06 $mAcm^{-2}$ at 875 mV. This could be associated with high porosity of the copper-containing electrodes, corresponding to an increase in surface area. As the surface area increases, more active sites are available for the oxygen evolution reactions and hence the overpotential decreases. It has been discussed in the literature that the

substitution of cobalt by foreign materials such as nickel and copper usually give rise to improved catalytic activity [101, 102].

**Table 4.1.** Onset potential and overpotentials of all prepared electrodes-corrected for their real surface area using the roughness factor**.**

| Composition | Onset potential (mV) | Over potential (mV) |
|---|---|---|
| $NiCo_2O_4$ | 532 ± 0.018 | 373 ± 0.025 |
| $Ni_{0.95}Cu_{0.05}Co_2O_4$ | 524 ± 0.012 | 365 ± 0.018 |
| $Ni_{0.9}Cu_{0.1}Co_2O_4$ | 518 ± 0.019 | 359 ± 0.027 |
| $Ni_{0.75}Cu_{0.25}Co_2O_4$ | 516 ± 0.007 | 357 ± 0.010 |
| $Ni_{0.5}Cu_{0.5}Co_2O_4$ | 487 ± 0.032 | 328 ± 0.046 |
| $Ni_{0.25}Cu_{0.75}Co_2O_4$ | 511 ± 0.001 | 352 ± 0.016 |
| $Fe_{0.1}Cu_{0.9}Co_2O_4$ | 537 ± 0.007 | 378 ± 0.009 |
| $Fe_{0.15}Cu_{0.35}Co_{2.5}O_4$ | 518 ± 0.020 | 359 ± 0.028 |
| $Fe_{0.1}Ni_{0.9}Co_2O_4$ | 541 ± 0.019 | 382 ± 0.026 |
| $Fe_{0.15}Ni_{0.35}Co_{2.5}O_4$ | 553 ± 0.011 | 394 ± 0.015 |
| $CuCo_2O_4$ | 474 ± 0.085 | 315 ± 0.044 |
| $Co_3O_4$ | 569 ± 0.043 | 410 ± 0.025 |

## 4.4. Discussion – Comparison between binary and ternary spinel oxides.

Binary spinel oxide $NiCo_2O_4$ shows the highest overpotential (373 mV) compared to ternary spinel oxides with the lowest overpotential of (328 mV). Increasing copper content in $NiCo_2O_4$ binary spinel oxide reduces the overpotential as shown in Table 4.1 and increases the current density (see Figure 4.2). This indicates that a ternary spinel oxide has advantages over a binary one in terms of enhancement in the true catalytic activity.

### 4.4.1 This work compared with other spinels prepared by Prof. Morin's group

Here we have compared our ternary work with this lab's existing work ($CuCo_2O_4$), shown in Figure 4.6. The cyclic voltammograms, all iron-containing ternary spinel oxides show higher current densities close to 0.35 $mAcm^{-2}$ at 800 mV than all other spinel oxides and binary spinel oxides prepared in our work shown in Figure 4.6. At 800 mV, ternary spinel oxides exhibit double current density higher than binary $CuCo_2O_4$ spinel oxides (0.15 $mAcm^{-2}$). However, copper-nickel containing ternary spinel oxides show lower current density than copper containing binary spinel oxides. According to copper content, there was a systematic current density change observed.

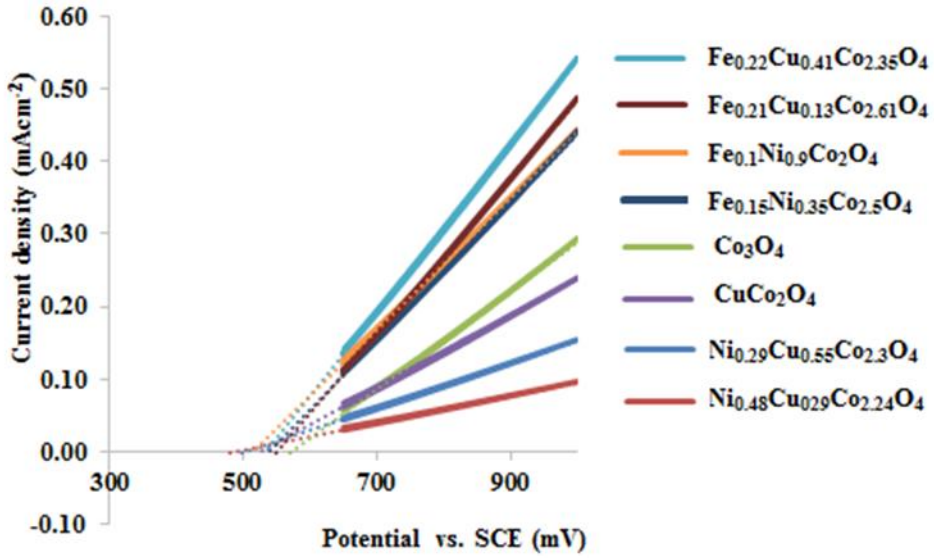


**Figure 4.6:** Cyclic voltammograms (corrected true catalytic activity) of binary and ternary spinel oxides, for scan recorded in a potential range of 400 mV to 1000 mV.

### 4.5. Discussion – Reproducibility test of SEM, EDX and CV

The SEM measurement performed for samples prepared in 2018 and 2019 showed similar images between the two years, as shown in Figure 4.7. Therefore, from the results of the different characterization methods (SEM, EDX and true catalytic activity) for the samples prepared in different years, we can conclude that our samples morphology is reproducible.

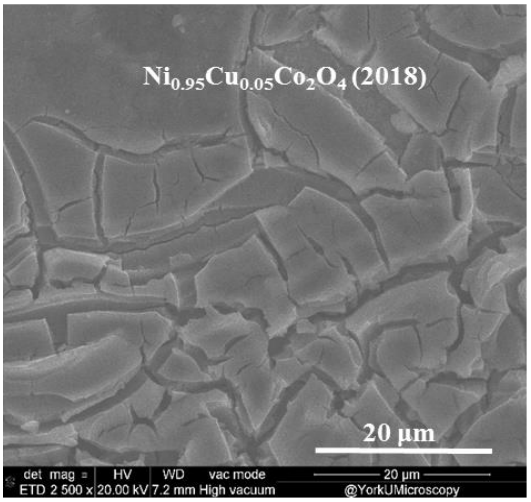
$Ni_{0.95}Cu_{0.05}Co_2O_4$ (2018)
20 µm
det mag HV WD vac mode 20 µm
ETD 2 500 x 20.00 kV 7.2 mm High vacuum @YorkUMicroscopy

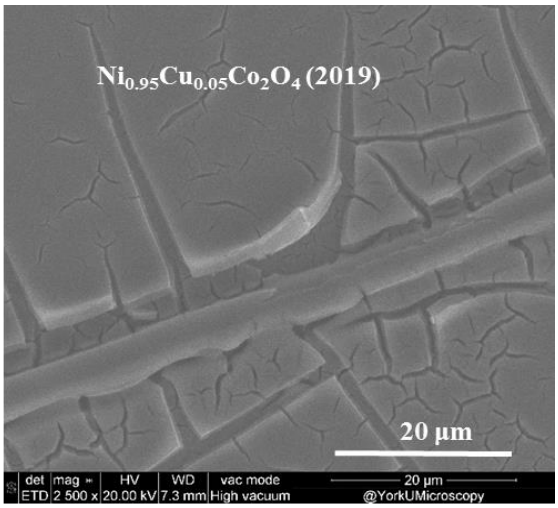
$Ni_{0.95}Cu_{0.05}Co_2O_4$ (2019)
20 µm
det mag HV WD vac mode 20 µm
ETD 2 500 x 20.00 kV 7.3 mm High vacuum @YorkUMicroscopy

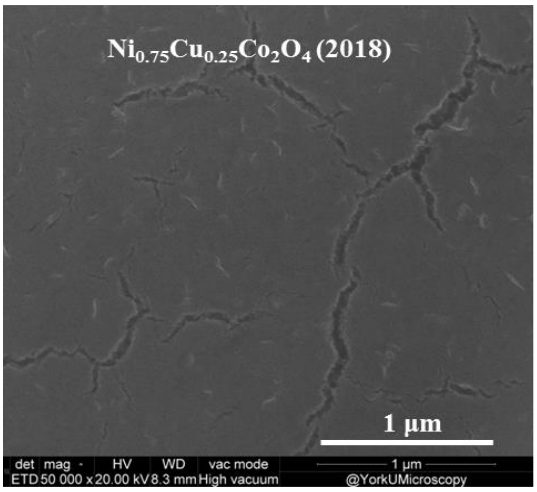
$Ni_{0.75}Cu_{0.25}Co_2O_4$ (2018)
1 µm
det mag HV WD vac mode 1 µm
ETD 50 000 x 20.00 kV 8.3 mm High vacuum @YorkUMicroscopy

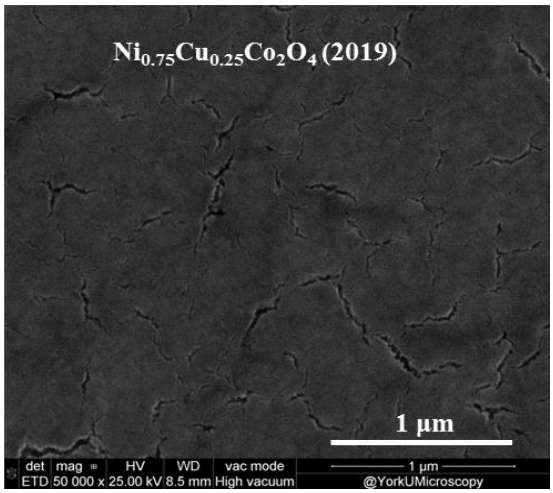
$Ni_{0.75}Cu_{0.25}Co_2O_4$ (2019)
1 µm
det mag HV WD vac mode 1 µm
ETD 50 000 x 25.00 kV 8.5 mm High vacuum @YorkUMicroscopy

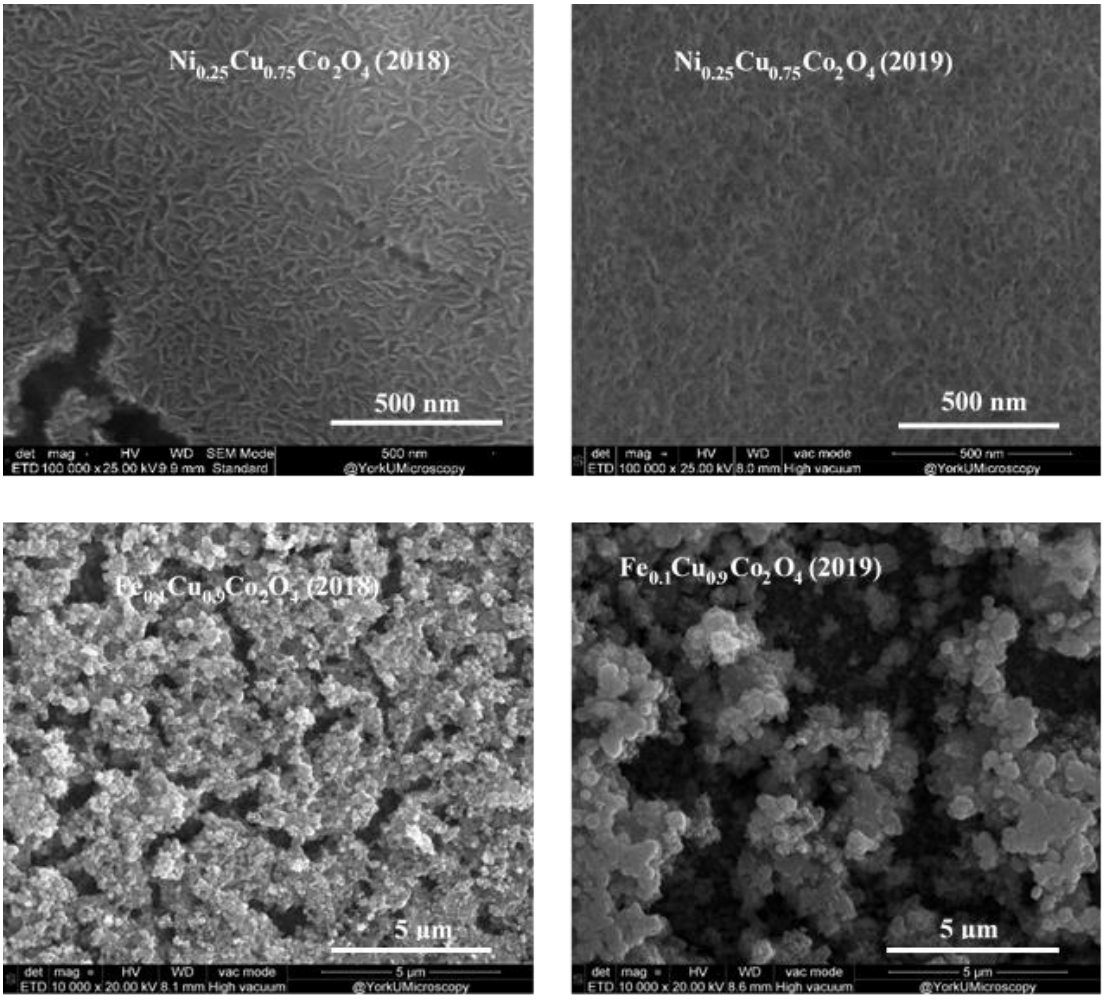


**Figure 4.7:** SEM images of samples prepared by the thermal decomposition method (in two different years) showing similarities in the morphology and reproducibility of the preparation method

The EDX measurement was performed on the $Fe_{0.1}Cu_{0.9}Co_2O_4$, $Fe_{0.15}Cu_{0.35}Co_{2.5}O_4$. Three sets of data collected in 2019, 2018 a and 2018 b were used for the error calculation. The relative errors of the sample $Fe_{0.1}Cu_{0.9}Co_2O_4$ and $Fe_{0.15}Cu_{0.35}Co_{2.5}O_4$ show very consistent values shown in table 4.2, even though they were tested in three different periods.

**Table 4.2:** EDX Relative errors comparison between $Fe_{0.1}Cu_{0.9}Co_2O_4$ and $Fe_{0.15}Cu_{0.35}Co_{2.5}O_4$ electrode prepared by the thermal decomposition method

| Samples | 2019<br>Relative error %<br>Fe/Co EDX ratio | 2018 a<br>Relative error %<br>Fe/Co EDX ratio | 2018 b<br>Relative error %<br>Fe/Co EDX ratio |
|---|---|---|---|
| $Fe_{0.1}Cu_{0.9}Co_2O_4$ | 5.2 | 6.4 | 5.1 |
| $Fe_{0.15}Cu_{0.35}Co_{2.5}O_4$ | 2.6 | 3.1 | 2.6 |

We have tested true catalytic activity for the samples prepared in different years. We obtained similar values for the current density. For samples prepared in 2018, the current density is ≈ 0. 05 mA at 800 mV while for the samples prepared in 2019, the current density is ≈ 0.053 mA at 800 mV. The average standard deviation and relative errors were calculated for the sample $Ni_{0.5}Cu_{0.5}Co_2O_4$ and $Ni_{0.25}Cu_{0.75}Co_2O_4$ as they showed better performance among all prepared samples. The average errors in current density were found for the sample $Ni_{0.5}Cu_{0.5}Co_2O_4$ and $Ni_{0.25}Cu_{0.75}Co_2O_4$ were 0.05062 mA $cm^{-2}$ ± 0.00267 (at 800 mV) and 0.05543 mA $cm^{-2}$ ± 0.00002 (at 800 mV) respectively. On the other hand, the average errors in overpotential were found to be (477 mV ± 176) and (467 mV ± 179) for the sample $Ni_{0.5}Cu_{0.5}Co_2O_4$ and $Ni_{0.25}Cu_{0.75}Co_2O_4$ respectively, shown in the error bar graphs, Figure 4.8.

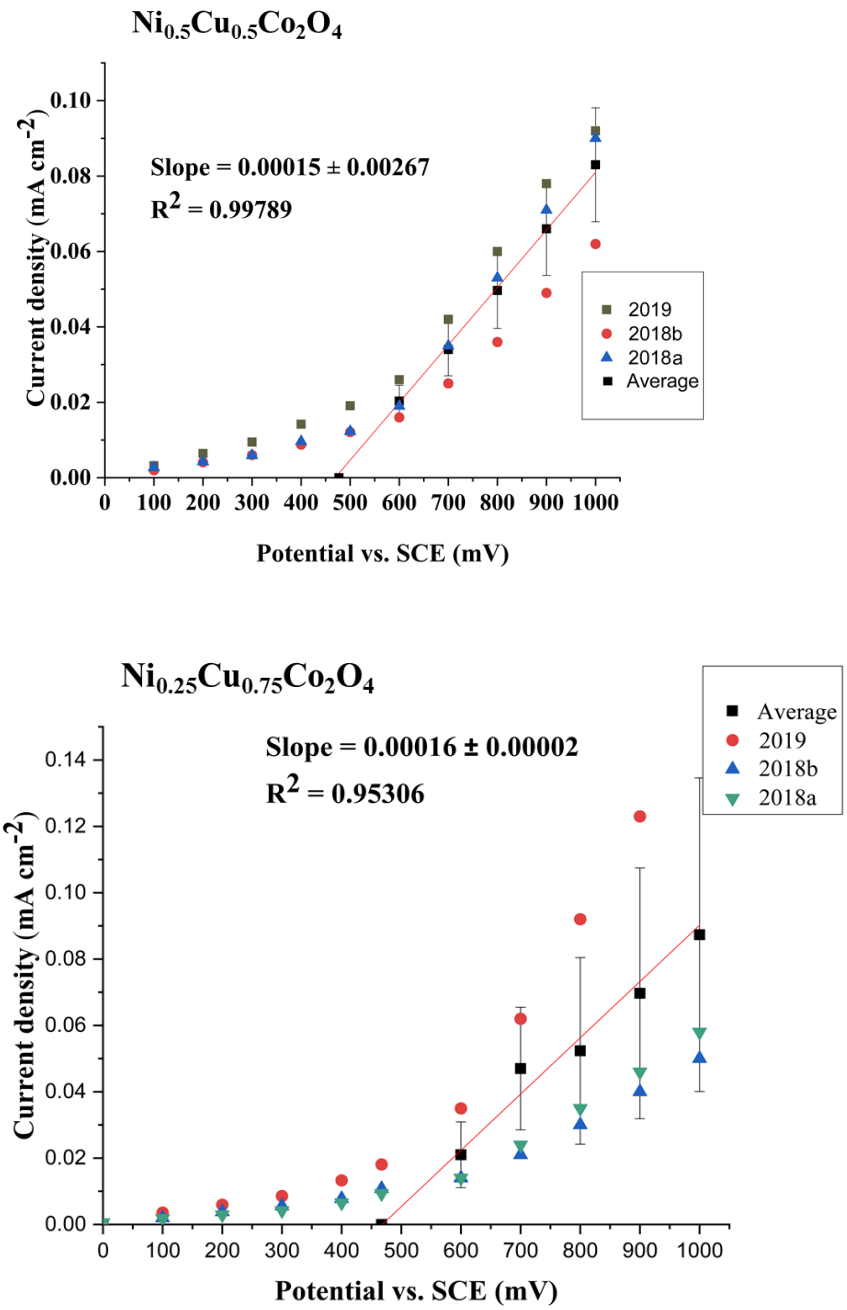


**Figure 4.8** The calculated error in current density and overpotential for $Ni_{0.5}Cu_{0.5}Co_2O_4$ and $Ni_{0.25}Cu_{0.75}Co_2O_4$ electrodes prepared by the thermal decomposition method.

## 4.6. Conclusion

In our study, as we introduce and increase the copper content of the ternary spinel oxide electrode, the electrocatalytic activity was increased. The iron containing electrodes show higher current density compared to pure $Co_3O_4$ spinel oxide electrode. Mixed valence states of the different metal cations of the spinel oxides could be facilitating the charge transfer between the cations in the octahedral sites and tetrahedral sites, the catalytic activity and this could be due to conductivity of these electrode material. This indicates that iron-containing nickel cobaltites are a promising anode material for oxygen evolution reaction in alkaline media. The current density from our prepared work was higher than the other spinel oxide electrode produced previously in our lab. As the copper content increased in the Nickel-cobalt spinel oxide, the overpotential decreased for some of the higher copper containing electrodes such as $Ni_{0.5}Cu_{0.5}Co_2O_4$ and $Ni_{0.25}Cu_{0.75}Co_2O_4$. From the results of our reproducibility test, for the samples prepared in different years, we can conclude that this work is reproducible.

# Chapter 5- Conclusion and Future work

## 5.1. Conclusion

To optimize a suitable electrode material for the oxygen evolution reaction, ternary spinel oxides $Ni_{1-x}Cu_xCo_2O_4$ ($0 \leq x \leq 0.75$), $Fe_y(Ni/Cu)_{x-y}Co_{3-x}O_4$ [($0.5 \leq x \leq 1$), and ($0.1 \leq \mathbf{y} \leq 0.15$)] have been prepared. Scanning electron microscopy (SEM) was used for analysis of the morphology of our prepared materials, while elemental analysis was done by energy dispersive X-ray spectroscopy (EDX). To obtain information regarding the structure of the prepared materials and lattice parameters, X-ray diffraction (XRD) analysis was performed. Electrochemical experiments were carried out using cyclic voltammetry (CV) to investigate the electrocatalytic activity of the prepared ternary spinel oxide electrode.

The SEM analysis of the $Ni_{1-x}Cu_xCo_2O_4$ electrode indicate that the surface morphology changes with nickel content and the surface gradually became more porous and homogeneous as the copper content increased. Some of the $Ni_{1-x}Cu_xCo_2O_4$ electrode surface appears to be more porous with grains that are uniformly distributed. From the SEM images, the $Fe_y(Ni/Cu)_{x-y}Co_{3-x}O_4$ electrode, the iron-copper electrode produced a more porous material compared to the electrode containing iron-nickel. The EDX analysis showed that there is a good correlation between the stoichiometric and EDX ratio for $Ni_{1-x}Cu_xCo_2O_4$ electrodes as Ni/Co ratios are very close to the expected values, however Cu/Co ratio tend to be systematically lower for all samples.

XRD analysis of all electrodes indicate the formation of spinel structures. While all samples exhibit spinel structure, $Fe_{0.1}Cu_{0.9}Co_2O_4$, and $Fe_{0.1}Ni_{0.9}Co_2O_4$ samples showed small amounts of an extra phase along with the spinel structure. The roughness factors for all prepared electrodes was obtained using values from cyclic voltammogram. The prepared $Ni_{1-x}Cu_xCo_2O_4$ (0

$\leq x \leq 0.75$) electrodes have higher roughness factors than $Fe_yCu_{x-y}Co_{3-x}O_4$ and $Fe_yNi_{x-y}Co_{3-x}O_4$, ($0.15 \leq x \leq 1.0$) electrodes. The $Ni_{0.5}Cu_{0.5}Co_2O_4$ electrode had the highest roughness factor with a value of 624 ± 64).

Cyclic voltammograms were obtained for the prepared electrodes within the range of -100 mV to 1000 mV in 1M KOH solution at the scan rate of 50 $mVs^{-1}$. From all the prepared $Ni_{1-x}Cu_xCo_2O_4$ electrodes, The $Ni_{0.25}Cu_{0.75}Co_2O_4$ gives the highest current density of 0.09 $mAcm^{-2}$ at 900 mV potential. However, the catalytic activity of iron containing electrodes show higher current density compared to all prepared electrodes and pure $Co_3O_4$ spinel oxide electrode. At a given potential, 900 mV the $Fe_{0.1}Cu_{0.9}Co_2O_4$ sample exhibits the highest current density of 0.45 $mAcm^{-2}$ among all other samples. Our prepared electrodes displayed lower overpotential than pure $Co_3O_4$ spinel oxide electrode. The $Ni_{0.5}Cu_{0.5}Co_2O_4$ electrode shows the lowest overpotential value of 328 ± 0.046 mV. These mixed oxides electrode exhibit good porosity, high catalytic activity as well as reproducibility. Therefore, in water electrolysis the iron-containing nickel or copper cobaltites could be some of the most promising anode materials for oxygen evolution reaction in alkaline media. Enhancement of the electrocatalytic activity of the electrodes could be explained further by performing conductivity analysis.

## 5.2. Future work

Future work will be to perform conductivity measurement on the prepared electrodes as it measured an electrical current which might have a direct influence on the electrocatalytic activity of the electrode. Conductivity can be measured by the four-probe method. There are two outer probes and two inner probes that are placed on a surface of the material. Current is passed through the two outer electrodes and the floating potential is measured by inner electrodes. The resistivity ($\rho$) can be calculated by the following equations [103]:

$$\rho = V/I * 2\pi S \quad (19)$$

where $\rho$ = resistivity, V = voltage, I = current, S = distance between point spacing. Therefore, electrical conductivity $\sigma$ ($\Omega^{-1} m^{-1}$) can be calculated by reversing the resistivity.

Electrocatalytic activity would be predicted from the conductivity of the material. Electrical conductivity in metal is a result of the movement of electrically charged particle (free electron) that allows metals to conduct an electric current. Our prepared electrodes are composed of mixed metal elements. Iron- copper containing cobalt based spinel oxide electrode exhibited higher catalytic activity, and conductivity analysis of these electrodes could provide information on the origin of their performance. This measurement will help better understanding in optimizing electrode compositions as well as material choice to improve better catalytic activity.

# References


[1] Electricity Statistics. International energy agency database. https://www.iea.org/statistics/electricity/ (Accessed Sept 2019).

[2] Marland, G; Rotty, R; Treat, N. *Tellus.* **1985**, *37B*, 243 - 258.

[3] Arico, A.; Bruce, P.; Scrosati, B.; Tarascon, J.; Van Schalkwijk, W. *Nat. Mater*. **2005**, *4*, 366-377.

[4] Liu, C.; Li, F.; Ma, P.; Cheng, H. *Adv. Mater*. **2010**, *22(8)*, 28-62.

[5] Trasatti, S. *Electrochim. Acta* **1984**, *29 (11*), 1503-1512.

[6] Trasatti, S. *Electrochim. Acta* **2000**, *45*, 2377-2385.

[7] Matsumoto, Y.; Sato, E. *J. Mat. Chem. Phys.* **1986**, *14*, 397- 426.

[8] Ying, J.Y. *Nanostructured materials*; Academic Press, Chapter 1, 2001**.**

[9] Trasatti, S. Interfacial Electrochemistry of Conductive Oxides for Electrocatalysis. In *Interfacial electrochemistry: Theory, Experiment and Applications*; Wieckowski Ed; New York, 1999.

[10] Lee, Y.; Suntivich, J.; May, K. J.; Perry, E. E.; Shao-Horn, Y. *J. Phys. Chem. Lett*. **2012**, *3*, 399 - 404.

[11] Trasatti, S.; Lodi.G. *Electrodes of Conductive Metallic Oxides,* Part A-B; Elsevier Science Publishers: Amsterdam, The Netherlands, 1980/1981.

[12] Rosa-Toro, La.; Berenguer, R.; Quijada, C.; Montilla, F.; Morallon, E.; Vazquez, J. L. *J. Phys. Chem.* **2006**, *47*, 24021-24029.

[13] Joshi, S. G.; Kulkarni, D. K.; Khandekar, P.V. J. *Bull. Mater. Sci.* **1982**, *4*, 455- 459.

[14] Hamdani, M.; Singh, R. N.; Chartier, P. *Int. J. Electrochem. Sci.* **2010**, *5*, 556-577.

[15] Tavares, A. C.; Cartaxo, M. A.; Pereira, M. I.; Costa F. M. *J. Electroanal. Chem.* **1999**, *464*, 187-197.

[16] Bursell, M.; Pirjamali, M.; Kiros, Y. *Electrochim. Acta* **2002**, *47*, 1651-1660.

[17] Wattiaux, A.; Grenier, J.C.; Pouchard, M.; Hagenrnuller, P. *J. Electrochim. Soc.* ***1987****, 134, (7),* 1714 -1718.

[18] Prakash, J.; Tryk, D.; Yeager, E. *J. Power Sources* **1990**, *29*, 413- 422.

[19] Merrill, M.; Dougherty, R. *J. Phys. Chem*. **2008**, *112(10),* 3655-3666.

[20] Chen, G.; Li, X.; Jia, J. *J. Electrochim. Acta* **2010**, *55*, 8197- 8206.

[21] Smart, L.; Moore E., *Solid State Chemistry – An Introduction, 2nd ed;* CRC press, Boca Raton, 2012.

[22] Rao, C.N.; Gopalakrishnan, J. *New Directions in Solid State Chemistry;* Cambridge University Press, New York, 1997.

[23] Issa, B.; Obaidat, I.; Albiss, B.; Haik, Y. *Int. J. Mol. Sci*. **2013**, *14*, 21266-21305.

[24] New proprietary technology to replace costly use of platinum group and rare earth metals in catalytic converter. http://www.cdti.com/spinel/ (Accessed Sept 2019).

[25] Singh, J. P.; Singh, R. N. *Indian J. Chem*. **2000**, *39A*, 819-825.

[26] Singh, J.P.; Singh, R.N. *J. New Mat. Electrochem. Syst.* **2000**, *3*, 131-139.

[27] Hamdani, M.; Singh, R.; Chartier, P. *Int. J. Electrochem. Sci*. **2010**, *5(4),* 556–577.

[28] Rao, C. N.; Subba Rao, G. V. *J. phys. stat. sol. (a)* **1970,** *1*, 597-652.

[29] Mirzaei, A.; Janghorban, K.; Hashemi, B.; Neri,G. "Metal-core@metal oxide-shell nanomaterials for gas-sensing applications: a review" *J. Nanoparticle Res*. **2015**, *17(9),* 371.

[30] Yonemura, M.; Yamada, A.; Kobayashi, H.; Tabuchi, M.; Kamiyama, T.; Kawamoto, Y.; Kanno, R. *J. Mat. Chem.* **2004**, *14*, 1948 –1958.

[31] Ellis, B.; Lee, K.; Nazar, L. *Chem. Mater*. **2010**, *22 (3),* 691–714.

[32] Liang, Y.; Vijayan, B.; Gray, K.; Hersam, M. *J. Am. Chem. Soc.* **2012**, *139(4)*, 3517–3523.

[33] Hussain, M.; Ibupoto, Z.; Abbasi, M.; Liu, X.; Nur, O.; Willander, M. *Sensors* **2014**, *14(3)*, 5415 –5425.

[34] Jiao, F.; Frei, H. *Angew. Chem.* **2009**, *48(10)*, 1841- 1844.

[35] Chen, J.; Miller, J.; Gerkeen, J.; Stahl, S. *Energy Environ. Sci*. **2014**, *7(4)*, 1382 - 1386.

[36] Singh, J.P; Singh, R.N. *Indian J. Chem*. **2000**, *39A*, 819 - 825.

[37] Singh, J.P.; Singh, R.N. *J. New Mater. Electrochem. Syst.* **2000**, *3*, 131-139.

[38] Nikolov, I.; Darkaoui, R.; Zhecheva, E.; Stoyanova, R.; Dimitrov, N.; Vitanov, T. *J. Electroanal. Chem.* **1997**, *429*, 157-168.

[39] Miley, G.H.; Luo, N.; Mather, J.; Burton, R.; Hawkins, G.; Gu, L.; Byrd, E.; Gimlin, R.; Shrestha, P. J.; Benavides, G.; Laystrom, J.; Carroll, D. *J. Power Sources* **2007**, 1*65*, 509 - 516.

[40] Choudhury, N.A.; Raman, R. K.; Sampath, S.; Shukla, A. K. *J. Power Sources* **200**5, *143*, 1-8.

[41] Nikolov, *J. Electroanal. Chem.* **1997**, *429*, 157-168.

[42] Angelov, S.; Tyuliev, G.; Marinova, T. *Appl. Surf. Sci.* **1987**, *27*, 381- 392.

[43] Li, G. H.; Dai, L. Z.; Lu, D. S.; Peng, S.Y. *J. Solid State Chem.* **1990**, *89*, 167-173.

[44] Marsan, B.; Fradette, N.; Beaudoin, G. *J. Electrochem. Soc.* **1992**, *139*, 1889 -1896.

[45] Lu, B.; Cao, D.; Wang, P.; wang, G.; Gao,Y. *Int. J. Hydrog. Energy* **2011**, 36, 72-78.

[46] Pandey, J.P.; Singh, R. N.; Singh ,N. K.; Lal, B.; Chartier, P.; Koenig, J. F. *J. Electrochim. Acta* **2000**, *45***,** 1911-1919.

[47] Niesen, T.; Guire, M. *J. Electroceram*. **2001**, *6*, 169-207.

[48] Burke, M.; Cast, M.; Trotochaud, L.; Smith, A.; Boettcher, S. *J. Am. Chem. Soc.* **2015**, *137(10)*, 3638-3648.

[49] Gerken, J.; Shaner, S.; Massé, R.; Porubskya, N.; Stahl, S. *Energy Environ. Sci*. **2014**, *7*, 2376-2382.

[50] Gerken, J., Chen, J., Massé, R., Powell, A., Stahl ,S. *Angew. Chem. Int. Ed*. **2012**, *51(27)*, 6676 -6680.

[51] Hasvold, O.; Johansen, K.H.; Mollestad, O.; Forseth, S.; Storkersen, N. *J. Power Sources* **1999**, *80*, 254-260.

[52] Bard A.J.; Faulkner L.R. *Eletcrochemical methods-Fundamentals and applications, 2nd ed.*; New York, 2001.

[53] Tavares, A.; Silva Pereira, M.; Cartaxo,M.; Costa,M., *J. Solid State Electro. Chem.* **2001**, *5*, 57-67.

[54] Berenguer, R.; Larosa-Toro, A.; Quijada, C.; Morallon, E. *J. Phys. Chem.* **2008**, *112*, 16945-16952.

[55] Wen,T.; Kang,H. *Electrochim. Acta* **1998**, *43*, 1729 -1745.

[56] Marco, J.; Gancedo, J., Garcia, *M. J. Solid State. Chem.* **2000**, *153*, 74 - 81.

[57] Verwey, E.; Boer, F.; Santen, J. *J. Chem. Phys*. **1947**, *174(15)*, 1091-1092.

[58] Godinho, M.; Catarino, M.; Pereira, M.; Mendonca, M. Costa, F. *Electrochim. Acta* **2002**, *47*, 4307- 4314.

[59] Ting Lu, Yi.; Chien**,** Yu.; Fang Liu, Ching.; Hsuan You, Ting.; Chang Hu, Chi. *J. Matter. Chem.* **2017**, *5*, 21016 - 21026.

[60] Bard A.J.; Faulkner L.R. *Eletcrochemical methods-Fundamentals and applications, 2nd ed.*; New York, 2001.

[61] Sapountzi, F.; Gracia, J.; Weststrate, C.; Fedriksson, H.; Niemantsverdriet, J. *Prog. Energy Combust. Sci.* **2017**, *58*, 1- 35.

[62] Trasatti, S. *J. Electrochim. Acta* **1984**, *29*, 1503 -1512.

[63] Appleby, A.; Nicholson, S. *J. Electroanal. Chem. Interf. Electrochem.* **1974**, *53*, 105 -119.

[64] Sampath, S.; Naik, Keerti. *Electrochim. Acta* **2018**, *292*, 268 - 275.

[65] Rossmeisl, J.; Qu, Z.; Zhu, H.; Kroes, G.; Nørskov, J. *J. Electroanal. Chem.* **2007**, *607*, 83-89.

[66] Dau**,** H.; Limberg , C.; Risch, M.; Roggan, S.; Strasser, P. *Chem. Cat. Chem.* **2010**, *2*, 724 - 761.

[67] Halck, N.; Petrykin, V; Krtil, P.; Rossmeisl J. *Phys. Chem. Chem. Phys*. **2014**, *16*, 13682-13688.

[68] Koper, M. *J. Electroanal. Chem*. **2011**, *660*, 254 - 260.

[69] Rossmeisl, J.; *Schlogl R Chemical energy storage, De Gruyter Graduate,* Berlin, 151 – 162, 2013.

[70] Viswanathan, V.; Hansen, H.; Rossmeisl, J.; Norskov, J. *J. Phys.Chem*. **2012**, *3*, 2948-2951.

[71] Stephens, I.; Bondarenko, A.; Perez-Alonso, F.; Bech, L.; Johansson, T.; Jepsen, A.; Frydendal, R.; Knudsen, B.; Rossmeisl, J.; Chorkendorff, I. *J. Am. Chem. Soc*. **2011**, *133*, 5485-5491.

[72] Hayes, R.; Kolaczkowski, *S. Chem. Eng. Sci.* **1994**, *21 (29)*, 3587 - 3599.

[73] Jia, J.; Li, X.; Chen, G. *Electrochim. Acta* **2010**, *55*, 8197 - 8206.

[74] Chi, B.; Lin, H.; Li, J. *Int. J. Hydrog. Energy* **2008**, *33*, 4763 - 4768.

[75] Baydi, M. E.; Tiwari, S. K.; Singh, R. N.; Rehspringer, J. L.; Chartier, P.; Koenig, J. F.; Poillerat, G. *J. Solid State Chem*. **1995**, *116*, 157-169.

[76] Koninck, M.; Poirier, S. C.; Marsan, B. *J. Electrochem. Soc*. **2006**, *153*, A2103-A2110.

[77] Gautier, J. L.; Trollund, E.; Rios, E.; Nkeng, P; Poillerat, G. *J. Electroanal. Chem.* **1997**, *428*, 47-56.

[78] Singh, R. N.; Koenig, J. F.; Poillerat, G.; Chartier, P. *J. Electrochem. Soc*. **1990**, *137(5),* 1408- 1413.

[79] Jiang, Y.; Wu, Y.; Xie, B.; Xie, Y.; Qian, Y. *Mater. Chem. Phys.* **2002**, *74*, 234-237.

[80] Sparatu, N.; Terashima, C.; Tokuhiro, K.; Sutanto, I.*;* Tryk, D. A.; Park, S. M.; Fugishima, A. *J. Electrochem. Soc.* **2003**, *150*, E337-E341.

[81] Doyle, R.; Godwin, I.; Brandon, M.; Lyons, M. *Phys. Chem. Chem. Phys*. **2013**, *15(33),* 13737-13783.

[82] Goldstein, J. I; Newbury, D. E; Joy, D. C; Lyman, C. E; Echlin, P.; Lifshin, E.; Sawyer, L.; Michael, J. R. *Scanning electron microscopy and X-ray microanalysis*, 3rd ed.; Kluwer Academic/Plenum Publishers: New York, 2003.

[83] Leng, Y. *Materials characterization: Introduction to microscopic and spectroscopic methods*. John Wiley & Sons: Asia, p 50,59, 2008 (Accessed Sept 2019).

[84] Schematic part of the scanning electron microscope (SEM), https://www.nanoimages.com/wp-content/uploads/sem_img2.png (Accessed Sept 2019).

[85] Raios-X, raios Gama e raios cosmicos. http://fisica-microfisica.blogspot.com/2013/10/raios-x-raios-e-raios-cosmicos.html?m=1. (Accessed Sept 2019).

[86] Cullity, B.D.; Stock, S. R.; *Elements of X-ray diffraction*, 3rd ed; Prentice hall: Upper Saddle River, 2001.

[87] Smart, L.; Moore E., *Solid State Chemistry – An Introduction*, 2nd ed*;* CRC press, Boca Raton, 2012.

[88] Bond, A.M; *Broadening of electrochemical horizons: principles and illustrations of voltammetric and related techniques*; Oxford University Press: New York, p34, 45, 2002 (Accessed Sept 2019).

[89] Wang, J. *Analytical Electrochemistry*, 3rd ed, John Wiley & Sons Inc., Hoboken, New Jersey, 2006.

[90] Gosser, J.; David, K., *Cyclic Voltammetry: Simulation and analysis of reaction mechanisms*; VCH: New York, 1993.

[91] Jolivet, J.; Tronc, E. *J. Colloid. Interf. Sci*.**1988**, *25 (2)*, 688 – 701.

[92] Guene, M.; Diagne, A.; Fall, M.; Dieng, M.; Poilleral, G. *Bull. Chem. Soc. Ethiop.* **2007**, *21(2)*, 255-262.

[93] JCPDS Powder diffraction file 20-181. *International Centre for Diffraction data,* Swarthmore, USA, 1988.

[94] Fradette, N.; Marsan, B. *J. Electrochem. Soc.* **1998**, *145*, 2320-2327.

[95] Ding, R.; Qi, L.; Wang, H. *ECS Electrochem. Lett.* **2012**, ***1*** (*3)*, A43-A46.

[96] Qian, L.; Gu, L.; Yang, L.; Yuan. H.; Xiao, D. *Nanoscale* **2013**, *5*, 7388-7396.

[97] Xiao, C.; Lu, X.; Zhao, C. *J. Chem. Commun.* **2014**, *50*, 10122-10124.

[98] Amri, A.; Jiang, Z.; Bahri, P.; Yin, C.; Zhao, X.; Duan, X.; Widja, H.; Rahman, M.; Pryor, T. *J. Phys. Chem.* **2013**, *117*, 16457 - 16467.

[99] Marsan, B.; Koninck, M.; Poirier, S. *J. Electrochem. Soc.* **2006**, *153*, A2103-A2110.

[100] Fierro, G.; Jacono, M.; Inversi, M.; Dragone, R.; Porta, P. *Top. Catal*. **2000**, *10*, 39-48.

[101] Trotochaud, L.; Samantha, L.; Young, S.; Boettcher, S. *J. Am. Chem. Soc*. **2014**, *136*, 6744-6753.

[102] Levine, S.; Smith, A.L. *Discuss. Faraday Soc*. **1971**, *52*, 290-301.

[103] White, M. *Physical properties of materials*. CRC Press, 2nd ed., p 316-318, 2012.